All-sky search for continuous gravitational-wave signals from unknown neutron stars in binary systems in the first part of the fourth LIGO-Virgo-KAGRA observing run

The LIGO Scientific Collaboration, the Virgo Collaboration and the KAGRA Collaboration

(Dated: December 5, 2025)

We present the results of a blind all-sky search for continuous gravitational-wave signals from neutron stars in binary systems using data from the first part of the fourth observing run (O4a) using LIGO detectors data. Rapidly rotating, non-axisymmetric neutron stars are expected to emit continuous gravitational waves, whose detection would significantly improve our understanding of the galactic neutron star population and matter under extreme conditions, while also providing valuable tests of general relativity. Neutron stars in binary systems likely constitute a substantial fraction of the unobserved galactic population and, due to potential mass accretion, may emit stronger gravitational-wave signals than their isolated counterparts. This search targets signals from neutron stars with frequencies in the $100 - 350$ Hz range, with orbital periods between 7 and 15 days and projected semi-major axes between 5 and 15 light-seconds. The analysis employs the GPU-accelerated `fasttracks` pipeline. No credible astrophysical signals were identified, and, in the absence of a detection, we report search sensitivity estimates on the population of neutron stars in binary systems in the Milky Way.

I. INTRODUCTION

Continuous gravitational waves (CWs) are long-lasting, nearly monochromatic signals. One of the most promising sources of CWs are rapidly rotating neutron stars (NSs) with non-axisymmetric mass distributions [1, 2]. These gravitational waves (GWs) arise from the star's time-varying quadrupole moment and can be generated through several mechanisms, which in turn provide a unique probe of the elastic, magnetic, thermal, and superfluid properties of NSs, both in isolated and binary systems [2, 3].

Non-axisymmetric distortions ("mountains") sustained either by elastic stresses in the crust or by strong magnetic fields can lead to the emission of CWs. Accreting systems in particular may generate sizable deformations [4–6]. Furthermore, non-axisymmetric instabilities can drive oscillation modes, such as r-modes, that may emit GWs, although their strength is strongly dependent on damping mechanisms and uncertain saturation amplitudes [7, 8]. Finally, free precession caused by a misalignment between the rotation and symmetry axes can lead to quasi-periodic emission [9].

The maximum possible ellipticity of a NS depends strongly on its interior composition and the poorly constrained equation of state, with estimates ranging from $\sim 10^{-6}$ for hadronic matter to $\sim 10^{-4}$ in scenarios allowing for more exotic physics such as crystalline phases [4, 10]. Additional factors such as general relativistic effects and strong magnetic fields can further influence the maximum sustainable deformation [11, 12]. By comparing the observational spindown limits on the ellipticity with these theoretical expectations, current CW searches probe astrophysically relevant regions of parameter space, and can provide constraints on the physics of dense matter [13].

NSs are among the densest known objects in the universe, with core densities of the order of nuclear values [14]. This makes them unique laboratories for probing the composition and behavior of matter under conditions not achievable in terrestrial laboratories, as well as studying potential deviations from general relativity, e.g. by looking for wave polarizations different from general relativity [3].

Highly magnetized rotating NSs can emit beams of electromagnetic radiation that are detected as pulses, in which case they are known as pulsars. A significant portion of the known pulsar population resides in binary systems [15], where mass accretion from a binary companion may increase the quadrupolar deformation of the NS, causing it to emit stronger CW signals than their isolated counterparts [6, 16–20]. Moreover, a large fraction of the known millisecond pulsars are in binary systems, spinning at frequencies that are in the sensitive band of ground-based GW detectors. Therefore, NS in binary systems are promising targets for CW detection in all-sky searches with data from current ground-based interferometers (IFOs).

Although numerous CW searches have been conducted to date, no detection has yet been achieved (see [1, 21–23] for recent reviews, and [24–40] for results from the O3 and O4 LIGO-Virgo-KAGRA observing runs [41–43]). In comparison with signals from compact binary mergers, from which all GW detections to date have originated [44–49], CW amplitudes are expected to be several orders of magnitude smaller, making them challenging to detect. Moreover, CW signals are subject to significant frequency modulation caused by the Earth's rotation and orbital motion [50–52]. As a result, all-sky searches must cover wide ranges of frequencies, sky positions, and in the case of binaries, orbital parameters [23]. These factors enlarge the search parameter space and require vast numbers of signal templates, up to more than 10^{16} templates for all-sky searches such as the one presented here.

To make CW searches computationally feasible, semi-coherent methods are commonly employed [53–56]. These approaches divide the data into shorter coherent segments, combine them incoherently, and follow up the most significant candidates with longer coherence times. This strategy reduces the computational load by allowing us to cover the parameter space less densely with templates and by improving robustness to small mismatches with the signal model, such as unmodeled astrophysical effects [57].

All-sky searches aim to detect CW emission from unknown NSs within our galaxy, that is, those that have not been observed using electromagnetic telescopes neither as pulsars nor as non-pulsating sources. Since only a small fraction of the estimated NS population has been observed as pulsars [58, 59], conducting this type of searches offers a valuable opportunity to find these undetected NSs.

To date, several pipelines have been developed and implemented for all-sky CW searches targeting unknown NSs in binary systems. These include the `TwoSpect` pipeline [60], and the `BinarySkyHough` pipeline [61], which has been employed in searches using data from the second [62] and third observing runs [63]. More recently, the `BinarySkyHou`$\mathcal{F}$ pipeline [64–66] has been introduced and the Falcon pipeline is being extended to include binary systems [67]. `BinarySkyHough` is based on the SkyHough [54] method, which uses the Hough transform [68] to search for CWs semi-coherently with the Hough number count detection statistic (see [54, 61, 69–71] for other works that use the Hough transform for searches of long-duration GW signals). Each of these pipelines makes different trade-offs between sensitivity and parameter space coverage, sacrificing some sensitivity in order to scan wider or more complex parameter spaces.

We present an all-sky search for CWs from unknown NSs in binary systems, carried out with the newly developed `fasttracks` pipeline [72]. `fasttracks` is a massively parallel Python engine built on `JAX` [73], designed to evaluate detection statistics for generic CW signals on Short Fourier Transform (SFT)-like data [74]. This includes the detection statistics used in the first stage of this search, which are summed weighted normalized power from the SFTs and summed weighted Hough number count. `fasttracks` can exploit Graphics Processing Units (GPUs) to accelerate the calculation of detection statistics across large amount templates needed for all-sky searches. Since this template evaluation is by far the most computationally expensive step, GPU acceleration makes large-scale searches feasible.

In addition, we employ a novel parameter-space partitioning strategy originally introduced in [72], which divides the high-dimensional search space into smaller regions, or "boxes". Each box is searched independently, producing its own output. This approach has two main advantages: different boxes can be computed in parallel in different GPUs and it avoids the need for clustering procedures in post-processing. Thanks to these improvements, `fasttracks` achieves higher computational efficiency compared to previous searches such as `BinarySkyHough` [63] and streamlines analysis with the new parameter-space partitioning strategy.

The remainder of this paper is organized as follows. in Sec. II, we outline the CW signal model. Sec. III describes the usage of data from the early fourth observing run (O4a). Sec. IV presents the details of the search pipeline. In Sec. V, we describe the line veto procedure. Sec. VI contains the sensitivity depth estimates of the search. Sec. VII discusses the most significant outliers identified, and explains how they were ruled out as non-astrophysical. The search results are discussed in Sec. VIII. Finally, our conclusions are summarized in Sec. IX.

II. SIGNAL MODEL

A NS exhibiting a deviation from perfect axial symmetry with respect to its rotation axis is expected to emit CWs at twice its rotational frequency. This emission arises from the time-varying mass quadrupole moment associated with the star's asymmetry. The resulting GW strain amplitude h_0, which can be measured by interferometric detectors, depends on the physical properties of the source and can be expressed as [1]

$$h_0 = \frac{4\pi^2 G}{c^4} \frac{I_{zz}\epsilon}{d} f_0^2, \tag{1}$$

where G is the gravitational constant, c is the speed of light, I_{zz} is the principal moment of inertia around the rotation axis (assumed to be the z-axis), d is the distance from the source to the detector, and f_0 is the intrinsic GW frequency. The equatorial ellipticity of the star, ϵ, can be related to the mass quadrupole moment Q_{22} via [4]

$$\epsilon = \sqrt{\frac{8\pi}{15}} \frac{|Q_{22}|}{I_{zz}}. \tag{2}$$

Due to the motion of Earth-based detectors relative to the Solar System Barycenter (SSB) and the motion of the NS around the binary system barycenter, the observed CW signal is subject to Doppler modulation from both effects. As a result, for the circular, non-relativistic binary orbit of the unknown searched NSs, the GW frequency measured at the detector is time-dependent and can be expressed as [61, 72]

$$f(t;\lambda) = f_0 \left[1 + \frac{\vec{v}(t)}{c} \cdot \hat{n} - a_p \Omega \cos(\Omega t - \phi_{\mathrm{b}}) \right], \tag{3}$$

where $\vec{v}\,(t)$ is the detector's velocity vector relative to the SSB, $\hat{n}$ is a vector that points from the SSB to the sky location of the source, parametrized by α, the right ascension and δ, the declination. f_0 is the GW frequency emitted by the source NS, a_p is the projected semi-major axis of the binary orbit in light-seconds, Ω is the angular orbital frequency of the source, and ϕ_{b} is the initial orbital phase. The last three parameters describe the orbital motion of the NS in the binary system.

The resulting frequency evolution, or *track*, traced by the signal in time-frequency space is the target of the search. It is parameterized by six quantities: $\lambda = \{f_0, \hat{n}, a_p, \Omega, \phi_\mathrm{b}\}$, where $\hat{n}$ is composed of α and δ.

The model described above assumes a circular, non-relativistic binary orbit. However, the search remains sensitive to signals from NSs in slightly eccentric systems, with an upper limit on the allowed eccentricity given by [61]

$$e \geq \frac{1}{2T_\mathrm{SFT} f_0 a_p \Omega}, \tag{4}$$

where T_SFT is the duration of each of the SFTs used in the analysis.

We assume that the NS does not undergo any glitches during the observing time and that spin wandering (stochastic fluctuations in the star's rotation frequency) can be neglected [75]. The typical glitch rate for known pulsars is of order one per year or less [76]. Estimates of spin wandering for accreting NSs suggest much smaller drifts than the frequency resolution of the semi-coherent methods used here. [77]. Accordingly, searches with observing duration of months to less than a few years may safely neglect these effects

Furthermore, as argued in [61], for observing durations of not more than a few years, CW searches targeting NS in binary systems do not require explicit searches of spin-down parameters. Consequently, we do not search over spin frequency derivatives in this analysis. Nonetheless, the search retains sensitivity to sources exhibiting spin-down or spinup values up to

$$\left|\dot{f}_0\right| \leq \frac{1}{T_\mathrm{SFT} T_\mathrm{obs}}, \tag{5}$$

the value above which the frequency track would deviate by more than one frequency bin in the data during the total observing run, T_obs.

III. DATA USED

For this search we use data from the first part of the fourth observing run of the LIGO-Virgo-KAGRA detector network. This segment of the run covers the period from 24 May 2023 15:00 UTC (GPS time 1368975618 s) to 16 January 2024 16:00 UTC (GPS time 1389456018 s). Correspondingly, this gives a total observing time of $T_\mathrm{obs} = 20477806$ s or 237 days.

This analysis makes use of data from the LIGO detectors at Hanford (H1) and Livingston (L1) [41]. We do not use data from Virgo [42], which was not observing in O4a; nor from KAGRA [43], which was not online for most of the run.

During O4a, H1 and L1 were in observing mode 67.5% and 69.0% of the time, respectively [48]. This represents a lower duty factor than in the O3a `BinarySkyHough` search [47, 63]. However, the observation time was significantly longer in O4a than in O3a (237 days vs 183 days). Multiplying the observing time by the duty factor, the relative amount of observing data is increased by 20.26% in O4a compared to O3a.

The data exhibit several different artifacts that can interfere with CW searches, including lines, combs, and hardware injections, any one of which may mimic the behavior of CW signals [78]. Instrumental lines are narrow-band features that appear as persistent monochromatic peaks in the detector's power spectral density. These features can originate from various sources such as injected calibration lines, digital clocks, power supplies, or environmental couplings [79]. These lines can have time dependent, non-stationary behavior in frequency and amplitude, and while some lines are isolated, others form part of broader spectral structures known as *combs*, which consist of multiple harmonics equally spaced in frequency and often arise from a common non-astrophysical origin [78].

The search is conducted using SFTs with a baseline duration of $T_\mathrm{SFT} = 1024$ s [74]. We start from the calibrated detector strain data channel `GDS-CALIB_STRAIN_CLEAN` (C00 calibration, [80]), restricted to science-mode segments with CAT1 vetoes [81]. These data are first processed by the self-gating algorithm [82], which removes large transient disturbances in the time domain. The gated strain data (G02) are then processed into Short Fourier Transform Data Base (SFDB) files [83]; this step includes another time-domain cleaning stage to suppress smaller glitches and transient artifacts.

For C00 low-latency data, the O4a uncertainty envelopes (v1) show amplitude and phase systematic errors of approximately 2% and 2° across the 20-2000 Hz band [80]. Finally, the cleaned and calibrated SFDBs are converted into SFTs with `LALSuite`'s `WriteSFTsfromSFDBs` tool, following the same procedure employed in the O3a all-sky binary CW search [63, 84].

Each SFT is produced with a 50% overlap between consecutive segments and a Tukey window with tapering parameter $\beta_\mathrm{Tukey} = 0.5$. Tukey-windowed SFTs contain a flat central region and tapered edges overlapped with consecutive SFTs, retaining high sensitivity to CW-type signals [69]. This procedure results in 25,426 1024-s SFTs from the H1 data and 26,552 1024-s SFTs from the L1 data.

IV. SEARCH PIPELINE

The search is built using the `fasttracks` pipeline to enable rapid evaluation of CW detection statistics with GPU acceleration, introduced in [72]. In this search, we use a parameter-space partitioning strategy for the six-dimensional search space $\lambda = \{f_0, \hat{n}, a_p, \Omega, \phi_\mathrm{b}\}$ (unit vector $\hat{n}$ composed of α and δ) associated with binary CW signals, also introduced in [72]. The pipeline evaluates detection statistics over several search templates, randomly sampled and in separate parameter-space regions known as *boxes*. This novel parameter-space partitioning naturally leads to a follow-up strategy: in each box of parameter space, only the most significant outliers are followed-up in a more sensitive search, while boxes dominated by instrumental artifacts can be vetoed and excluded from further analysis. Moreover, rather than covering the parameter space with a regular grid of templates, we employ random sampling with resolution chosen to control template mismatch. Details of the resolution criteria will be discussed in Sec. IV C, specifically Eq. (13). This approach does not degrade sensitivity compared with grid-based methods, as it keeps the average mismatch between templates and potential signals controlled and reduces correlations between templates [85, 86].

The output from each box is then passed to a post-processing stage (Sec. V), where high-significance candidates are subsequently followed up using more sensitive methods, as detailed in Sec. VII.

A. Parameter space

We perform a blind, all-sky search for CWs in the frequency range from 100 Hz to 350 Hz. The computational cost of the search grows steeply with frequency, scaling as f_0^6 due to the six-dimensional parameter space as derived in [72]. As a result, higher-frequency bands are significantly more expensive to analyze than lower ones.

The total frequency range is divided into 0.125 Hz sub-bands, for a total of 2000. Each sub-band is processed independently and partitioned into boxes (Sec. IV C).

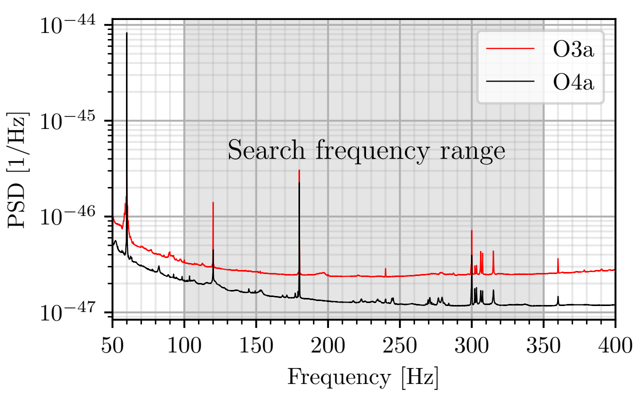

FIG. 1. Comparison of the O3a and O4a multi IFO power spectral density using the data from the H1 and L1 LIGO detectors. The grey area indicates the search frequency range.

The IFO's sensitivity in each frequency band can be seen in Fig. 1, which illustrates the inverse square root averaged multi-IFO (H1 + L1) power spectral densities (PSDs). We compute the PSD from the single-sided IFO PSD, $S_n(f)$, using an average of inverse-squared PSDs from individual SFTs, as in [87],

$$S_n(f) = \sqrt{\frac{N}{\sum_\alpha \left(S_\alpha(f)\right)^{-2}}}, \tag{6}$$

where N is the number of SFTs individually indexed by α contributing to the estimate at frequency f and $S_n(f)$ is the estimated multi-IFO PSD in the frequency band, computed as the power-2 sum of the individual IFO PSDs. Note that different analyses differ in the mean used to compute the respective PSDs. In the case of CW searches, the power-2 gives the most representative PSD for our searches and for the search sensitivity estimation in Sec. VI.

In O4a, the detectors show improved sensitivity compared to O3a. Whereas in O3a the most sensitive frequencies were in the 150-300 Hz range, in O4a, the optimal performance is in the 200-400 Hz range. The O4a search range overlaps with this most sensitive band of the detectors during the run.

For the binary orbital parameters, we target signals from systems with projected semi-major axis amplitude a_p along the line of sight between 5 and 15 light-seconds and orbital periods P ranging from 7 to 15 days. As illustrated in Fig. 2, this parameter space is chosen to match measured characteristics of observed galactic NSs, focusing on a parameter region which circumscribes a high-density area of known pulsars in binary systems [15]. This choice also corresponds to Region B from the O3a `BinarySkyHough` search [63], and overlaps in the upper 50 Hz with the range in [65] and for a_p in the 10 to 15 l-s range, but not in P. The O3a `BinarySkyHough` search [63] also included other parameter space regions below 100 Hz; we did not repeat the search in those areas in order to maximize the search sensitivity where the O4a sensitivity had improved the most compared to O3a.

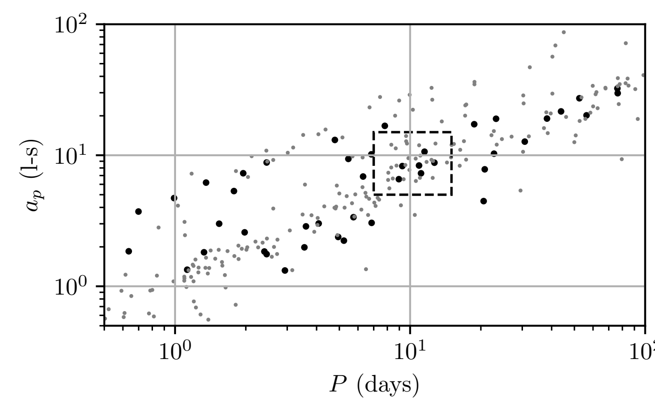

FIG. 2. Binary parameter space covered in the search. Large black dots indicate known pulsars with possible CW emission frequencies in the search range, while grey points correspond to sources outside this range. The boxed rectangular region denotes the portion of the binary parameter space explored in this search. Source: ATNF Pulsar Catalogue [15].

Parameter	f_0 [Hz]	α [rad]	δ [rad]	P [days]	a_p [l-s]	$\phi_{\rm b}$ [rad]
Range	[100,350)	$[0, 2\pi)$	$(-\frac{\pi}{2}, \frac{\pi}{2})$	$[7, 15)$	$[5, 15]$	$[0, 2\pi)$

TABLE I. Search parameter ranges.

The full search parameter space is summarized in Table I. In addition to the intrinsic frequency and binary orbital parameters discussed above, the search covers the whole sky in α and δ. The binary orbital phase $\phi_{\rm b}$ is also searched over its entire physical range.

B. Detection statistics

To identify potential CW signals in the data, we rely on detection statistics that measure the accumulation of excess power along the time–frequency tracks predicted by a given signal model. In practice, a CW signal from a NS in a binary system will produce a characteristic frequency evolution determined by the source parameters. For each template, we define a frequency track across the sequence of SFTs, which represents how a CW signal would evolve in time given the template parameters. Along this track, we add together the corresponding values of the detection statistic from each SFT. If a real signal is present, the detection statistic will accumulate along the track and stand out above the random fluctuations of detector noise, whereas in the absence of a signal the summed statistic will remain consistent with noise.

As in [72], we employ two complementary statistics: the weighted normalized power, which directly measures excess power in the data, and the Hough weighted number count, which is more useful to evaluate the persistence of such excess power across the observing time. The derivation below introduces the normalized power statistic and shows how it is summed along signal tracks to construct the detection statistic used in the search.

Following the notation convention in [72], let $\tilde{x}\,[t; f]$ denote the value of the SFT at time t (the start time of the SFT) and frequency f, each SFT is identified by an i index and the detector index X. Normalizing by the single-sided noise PSD in the band under analysis $S_{nXi}\,[f]$ (The PSD is estimated with a 101-bin running-median estimate for each SFT and frequency f) and the SFT time baseline $T_{\rm SFT}$, we define the normalized power statistic as

$$s\,[t; f] = \frac{4\,|\tilde{x}\,[t; f]|^2}{T_{\rm SFT} S_{nXi}\,[f]}. \tag{7}$$

A search template $\lambda = \{f_0, \hat{n}, a_p, \Omega, \phi_{\rm b}\}$ defines a signal frequency evolution $f\,(t; \lambda)$ across the observing time. The summed weighted normalized power detection statistic is computed by summing the normalized power along the signal track defined by the template,

$$s(\lambda) = \sum_{X,i} w_{Xi}(\hat{n}) s[t_{Xi}; f(t_{Xi}; \lambda)]\,, \tag{8}$$

where $w_{Xi}(\hat{n})$ are time-dependent weights that incorporate both detector sensitivity and antenna response, t_{Xi} refers to time at index i and detector X. The appropriate weights for all-sky searches from isotropically oriented sources are [87, 88]

$$w_{Xi}(\hat{n}) \propto \frac{a^2(t_{Xi}; \hat{n}) + b^2(t_{Xi}; \hat{n})}{S_{nXi}}, \tag{9}$$

where S_{nXi} is the averaged single-sided PSD of the noise in the frequency band under analysis[1], and where a and b are the detector's response functions to the two polarizations of the GW for a source located in direction $\hat{n}$ on the sky. Their definition can be found at [50]. These weights are normalized such that

$$\sum_{X,i} w_{Xi}\,(\hat{n}) = 1. \tag{10}$$

In order to evaluate the detection statistics across large template banks, we use the vectorization of the computation over batches of templates as implemented in `fasttracks` [72, 89]. This vectorization is done using the `jax.vmap` function [73].

In addition to the normalized power statistic, we also use the weighted Hough number count [54] to filter out transient noise artifacts. This statistic was previously also used in the O3a `BinarySkyHough` search [63] and has been used in a multitude of CW searches [27, 62, 69, 90]. It is defined as

$$\mathrm{nc}\,(\lambda) = \sum_{X,i} w_{Xi}(\hat{n}) \mathrm{nc}\,[t_{Xi}; f\,(t_{Xi}; \lambda)]\,, \tag{11}$$

where the number count of an SFT is defined as the digitized normalized power per SFT given by

$$\mathrm{nc}\,[t, f] = \begin{cases} 1 & \text{if } s\,[t; f] > 3.2 \\ 0 & \text{otherwise} \end{cases}. \tag{12}$$

As in [72], the threshold $s\,[t; f] > 3.2$ is equivalent to the $\rho_{\rm th} > 1.6$ optimal threshold to minimize the false dismissal rate derived in [54], given our definition of normalized power in Eq. (7).

The Hough number count acts as a persistence filter. While transient noise may produce large spikes in the normalized power statistic $s\,[t; f]$, it may affect only a small subset of the time series. In contrast, a CW signal will maintain consistent power increases over many segments. Hence, the Hough number count is more robust to brief transients and provides a discriminator against them.

---

[1] Note the difference between $S_n(f)$ in Eq. (6) (multi-IFO PSD computed as using average of inverse-squared PSD), the $S_{nXi}\,[f]$ in Eq. (7) (estimated with a 101-bin running-median estimate for each SFT and frequency f) and the S_{nXi} in Eq. (9) (averaged single-sided PSD of the noise in the frequency band under analysis).

C. Parameter space partitioning into boxes

To explore the six-dimensional parameter space $\lambda = \{f_0, \hat{n}, a_p, \Omega, \phi_\mathrm{b}\}$ of CW signals from NSs in binary systems, we adopt a box-based partitioning strategy, first introduced in [72]. Partitioning the parameter space makes post-processing more straightforward, since contaminated boxes can be vetoed and promising candidates followed up independently. Unlike previous searches, which required clustering strategies to sieve through the vast number of initial candidates and group together those likely originating from the same source, our approach reduces the results to a smaller set without this need for clustering.

The idea is to divide the parameter space into a large number of non-overlapping regions (or "boxes"), each covering a small portion of the total search volume. Each box is searched independently using a random template bank that densely samples its region.

To determine the size and number of templates in each box, we use characteristic resolution equations. For a box centered at parameters $(f_0, \hat{n}, a_p, \Omega, \phi_\mathrm{b})$, the corresponding step sizes in each parameter direction are

$$\delta f_0 = \frac{1}{T_\mathrm{SFT}} \;, \quad \delta\mathrm{sky} = \left(\frac{1}{T_\mathrm{SFT} f_0 v/c}\right)^2 \;, \quad \delta a_p = \frac{1}{T_\mathrm{SFT} f_0 \Omega} \;,$$
$$\delta\Omega = \frac{1}{T_\mathrm{SFT} f_0 a_p \Omega T_\mathrm{obs}} \;, \quad \delta\phi_\mathrm{b} = \frac{1}{T_\mathrm{SFT} f_0 a_p \Omega} \;. \tag{13}$$

To adjust the number of templates per box, we apply an oversampling factor, increasing or decreasing the step sizes defined in Eq. (13) times the oversampling factor. Increasing this factor makes the template bank denser (and search potentially more sensitive), however, also more computationally expensive. The oversampling values are tuned based on frequency band, as described in Sec. IV D.

The box-based search proceeds as follows:

1. Divide the search frequency range into 0.125 Hz sub-bands.

2. The boundaries of each search box in the physical parameter space $\Delta\lambda$ are mapped to a properly defined auxiliary parameter space, in which the grid steps defined above become uniform (see App. A for the definition of the auxiliary parameter space and the construction of the uniform grid there).

3. In this uniform space, divide the search volume into equally sized, non-overlapping boxes.

4. Randomly sample the templates from a uniform distribution inside each box. The number of templates inside a box is the oversampling factor times the amount of templates we would get with a grid if the step sizes were those in Eq. (13).

5. Map each sampled template back to physical parameter space, evaluate its detection statistics, and retain the template with the highest value according to the criteria in Sec. IV D.

The number of boxes used per frequency band is shown in Fig. 3, and further details of the partitioning algorithm can be found in App. A.

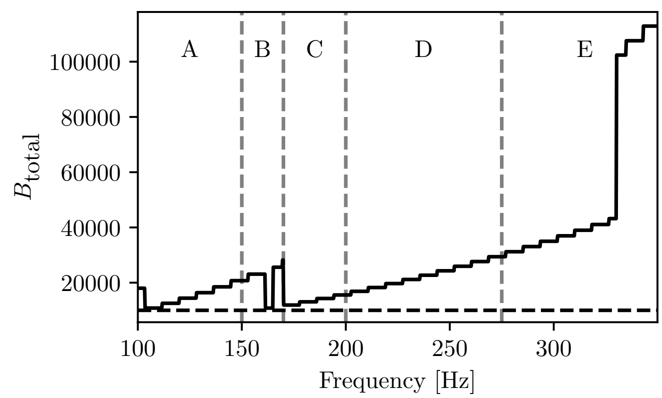

FIG. 3. Total number of boxes per 0.125 Hz frequency band across the full search range. The lettered regions (A-E) correspond to the frequency intervals defined in Table II. The dashed horizontal line marks the minimum enforced number of boxes (10^4). Sudden changes in the number of boxes correspond to transitions between regions where either the minimum box constraint or the 10^8 templates-per-box criterion dominates the partitioning as explained in App. A.

D. Two step setup

Our search adopts a two-step strategy inspired by the methodology used in the O3a `BinarySkyHough` search [63].

For each box in the parameter space, we begin by evaluating the weighted Hough number count statistic $\mathrm{nc}(\lambda)$ for all templates using only half of the available SFTs, skipping every other SFT in the time series. This first step acts as a filter to identify templates associated with CW signal behavior, showing persistent power accumulation over time. We use half the SFTs in order to reduce the computational cost of this first step.

From this first-stage evaluation, we retain the top 0.2% templates per box ranked by $\mathrm{nc}(\lambda)$. This fraction corresponds approximately to those templates whose $\mathrm{nc}(\lambda)$ exceeds the mean by more than three standard deviations, assuming Gaussian noise. The mean and standard deviation are calculated from all the $\mathrm{nc}(\lambda)$ computed per box.

In the second step of the search, we compute the weighted normalized power statistic $s(\lambda)$ for the subset of templates retained from the first step using the full set of SFTs. For each box, we identify the template with the

Region	Frequency [Hz]	Oversampling	Follow-up CR threshold
A	[100, 150)	4.0	7.0
B	[150, 170)	2.0	7.0
C	[170, 200)	1.0	7.0
D	[200, 275)	0.25	7.0
E	[275, 350)	0.25	7.2

TABLE II. Oversampling factor and follow-up CR threshold used in each frequency region.

highest $s(\lambda)$ as the most significant candidate from that region of parameter space.

Different boxes contain different weight distributions $w_{Xi}(\lambda)$ because they can be located at different sky positions. Therefore, to allow for sky-independent statistical significance comparisons across boxes, we use the weighted normalized power critical ratio (CR), defined as

$$\Psi_s = \frac{s - \langle s \rangle}{\sigma_s}, \tag{14}$$

where $\langle s \rangle$ and σ_s are the expected mean and standard deviation of the weighted normalized power statistic in Gaussian noise. These are computed analytically for each box from the weights following the derivation in [72],

$$\langle s \rangle = 2 \sum_{X,i} w_{Xi} \,, \tag{15}$$

$$\sigma_s^2 = 4 \sum_{X,i} w_{Xi}^2 \,, \tag{16}$$

where, given the weights normalization in Eq. (10), $\langle s \rangle = 2$.

We use different oversampling factors across the frequency range. At lower frequencies, where the number of required templates is relatively small, we use higher oversampling values, resulting in denser template banks. Conversely, at higher frequencies, where the parameter space volume increases due to frequency-dependent resolution scaling, we reduce the oversampling factor.

We define five frequency regions, each with a corresponding oversampling factor and follow-up threshold. Candidates with CR values above the specified threshold are further analyzed in the follow-up stage (see Sec. VII). The different frequency regions together with their oversampling factors and follow-up thresholds are described in Table II. The oversampling factors and follow-up thresholds are chosen based on the available computational resources in order to maximize the search sensitivity to continuous gravitational waves.

Fig. 4 illustrates the highest CR values obtained per each frequency band in each region. In some frequency bands, the highest CR values are orders of magnitude larger than those in neighboring bands, a sign of possible contamination from instrumental artifacts. This motivates the introduction of a band-vetoing stage to identify and veto such bands.

V. KNOWN LINES VETO

In this step, we identify and discard candidates affected by known instrumental artifacts. This is used to mitigate the contamination from spectral lines that can mimic the expected behavior of CW signals [92].

We use the official list of known instrumental lines from the O4a observing run [91] to identify such contaminations. Each known artifact in the list is examined to determine which frequency ranges affected by its harmonics, based on the tracks searched for each frequency band. The contamination reach of each line is described in App. C.

Based on the contamination, bands are classified as either non-vetoed, partially contaminated, or fully contaminated:

- **Non-vetoed bands**: Bands with fewer than 2000 candidates above the CR threshold are not vetoed. One candidate per box per band is retained for follow-up. Candidates from these bands may still be vetoed due to instrumental artifact contamination after the first stage follow-up, as explained in Sec. VII.

- **Fully vetoed bands**: Bands that are entirely within the contaminated region of one or more known lines and that exceed 2000 candidates above threshold are removed from the follow-up. These bands are presumed to be dominated by instrumental artifacts.

- **Partially vetoed bands**: Bands that are only partially affected by contamination and that also contain more than 2000 candidate are cleaned by removing candidates whose boxes fall within the contaminated region. Candidates from the rest of the band are followed-up.

The 2000 candidates threshold is an informed choice based on the candidates per band resulting from the search and the distribution observed in Fig. 5, where most bands have under 1000 candidates above the corresponding follow-up threshold.

To minimize the false dismissal probability of true astrophysical signals [92], only frequency regions with well-documented instrumental disturbances are vetoed outright, and partially contaminated bands are partially vetoed (That is, vetoing only the part of the band that may be contaminated by a known line as defined in in App. C) rather than excluded entirely.

Frequency bands not vetoed by this procedure may still be contaminated by unidentified instrumental artifacts. For example, since the search targets signals whose amplitude is much lower than the detector noise floor, it can be affected by lines that were not seen by the O4a lines analysis.

Across the 2000 search frequency bands, each of width 0.125 Hz, the initial number of candidates above their

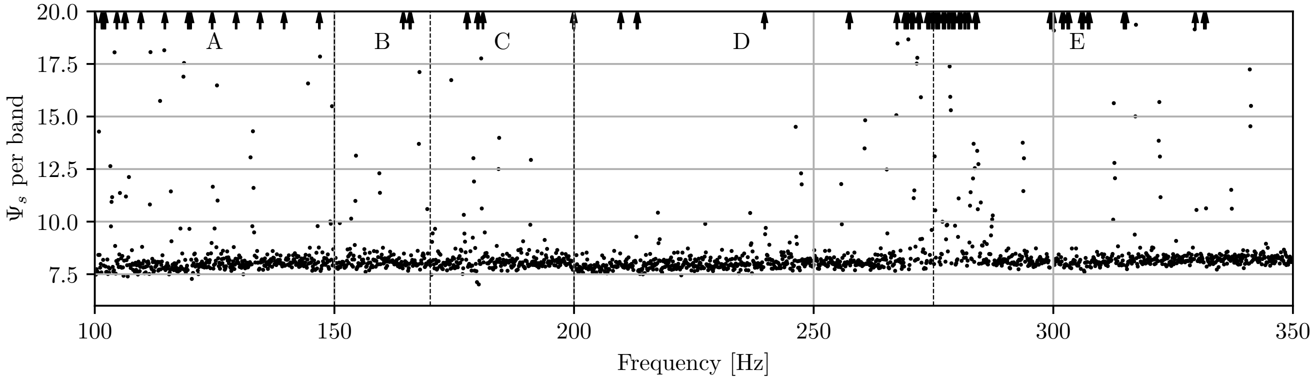

FIG. 4. Highest CR values per frequency band. Arrows indicate frequency bands where the highest value is above 20.

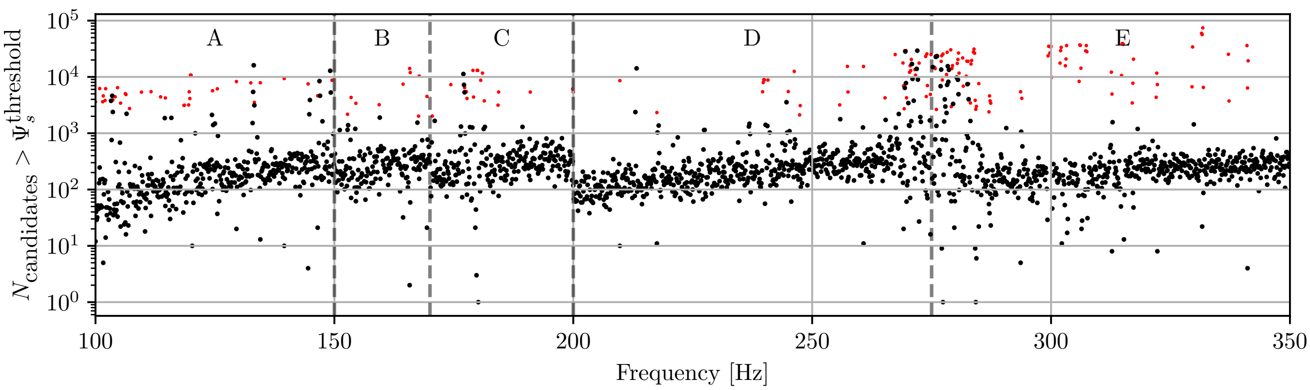

FIG. 5. Number of candidates per 0.125 Hz band with CR above the threshold, as a function of frequency. Frequency regions A through E correspond to those defined in Table II. Each black dot represents the number of candidates above threshold in a single band. Red dots indicate bands that were fully or partially vetoed due to contamination from known instrumental artifacts listed in the O4a lines list [91].

corresponding CR threshold (Table II) was 3,253,671. After the known lines veto, the number of surviving candidates is reduced to 927,443, corresponding to 28.5% of the original sample. Table III summarizes the classification of the bands. Fig. 5 illustrates the number of candidates above threshold in each band. The vetoed frequency ranges can be found in App. C.

Band type	**Count**	**% Bands**	**Bandwidth [Hz]**
Non-vetoed	1818	90.9%	227.25
Vetoed	182	9.1%	16.995
Totally	65	3.25%	8.125
Partially	117	5.85%	8.87

TABLE III. Summary of frequency band classification after the application of line and comb vetoes. Partial vetoes refers to bands where only a fraction of the templates are discarded due to contamination. The partially vetoed bands sum 14.625 Hz, of which 60.65% have been vetoed, corresponding to the 8.87 Hz on the table.

VI. SENSITIVITY DEPTH ESTIMATION

Similar to previous all-sky searches, we assess the sensitivity of this search to putative sources in the search space using software simulated signals added to detector data in selected frequency bands [62, 63, 90, 93, 94]. Through these simulations, we establish a population-based h_0 that is detectable 95% of the time.

We measure this h_0 using the sensitivity depth [95, 96], defined as

$$\mathcal{D} = \frac{\sqrt{S_n(f)}}{h_0}, \tag{17}$$

where S_n is the single-sided IFO PSD of the detector noise defined in Eq. (6), and h_0 is the intrinsic signal strain amplitude. The sensitivity depth provides a figure of merit that normalizes h_0 by the detector noise, facilitating comparisons across different frequency bands and search methods. Nonetheless, for these comparisons it is important to note that the sensitivity depth remains highly dependent on the searched parameter ranges in addition to frequency. These sensitivity depth estimates are used to set thresholds in the follow-up procedure (Sec. VII) and to study the astrophysical reach of the search (Sec. VIII).

For each 0.125 Hz frequency band in which injections are performed, we select the highest $S_n(f)$ within the band to evaluate sensitivity depths and search for the $\mathcal{D}^{95\%}$ value at which we determine the amplitude h_0 at which 95% of injections are recovered above threshold.

For each injected signal, we construct a small region centered on the injection parameters. The region spans ± 3 resolution units in all search dimensions according to Eq. (13), except for the binary phase $\phi_{\rm b}$, where a ± 5 resolution range is used. This choice has been made because it is more challenging to constrain the binary phase of simulated signals compared to the other parameters. These regions are designed to be compatible with the first-stage follow-up prior ranges in Sec. VII, making sure that any detectable signal in this setup is recovered and followed up by the pipeline.

Besides the resolution intervals shown in Eq. (13), the specific ones for α and δ are set using

$$\delta\alpha = \frac{1}{T_{\rm SFT}(v/c)f_0}\frac{1}{\cos\delta}, \quad \delta\delta = \frac{1}{T_{\rm SFT}(v/c)f_0}, \tag{18}$$

which take into account the $\cos\delta$ dependence arising from spherical coordinates to make resolution intervals correctly centered and spaced around injected signals.

All signals are injected into the same O4a SFT data used in the search using the `PyFstat` software package [97–100]. `PyFstat` is built on top of `LALSuite` [84] and contains multiple utilities for CW searches, such as injection generation or candidate follow-ups. After injecting the signals, we rerun the whole analysis on the small intervals, computing the detection statistics over the corresponding box with the same oversampling factor as used in the main search. We then check whether the candidate template CR value exceeds the corresponding CR follow-up threshold from Table II, which allows us to determine if the injection would have been one of the outliers passing to the follow-up stage. Afterwards, we use this information to estimate the detection efficiency and corresponding sensitivity depths.

To classify an injected signal as detected, we require that at least one candidate template within the injection search region satisfies the following three conditions:

1. The number count statistic $\mathrm{nc}(\lambda)$, computed using half of the SFTs, must be greater than the lowest $\mathrm{nc}(\lambda)$ value from the first stage of the search for the box in which the signal was injected. This ensures that the candidate template would have passed the persistence filter used in the first search step.

2. The CR must exceed the maximum found in the second stage of the search for that same box. This confirms that the candidate template would have been selected as the most significant outlier in that box.

3. The CR value must also surpass the follow-up CR threshold for the corresponding frequency band.

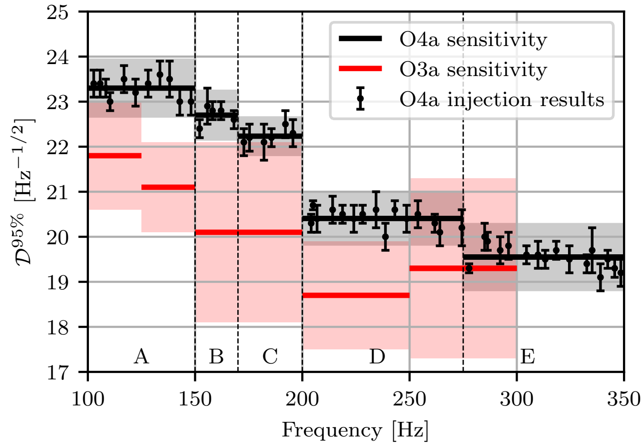

FIG. 6. 95% sensitivity depths $\mathcal{D}^{95\%}$ as a function of frequency. Each point represents a 0.125 Hz band with injection results, with error bars showing $\pm\sigma$ from the sigmoidal fit. Shaded regions show the average sensitivity depth per frequency region with its 3σ uncertainty (see Table IV). Comparison between the results of this search (in black) and the results of the O3a BinarySkyHough search [63] (in red).

We inject signals into at least one 0.125 Hz band every 5 Hz across the search frequency range in non-vetoed bands in Sec. V. Therefore, the sensitivity estimates do not apply to the vetoed frequencies from Sec V, listed in Table VI.

In each selected band, we inject 500 signals at different depths centered around the expected $\mathcal{D}^{95\%}$, with parameters drawn from uniform distributions over the phase and amplitude parameters. Each signal is injected at a random frequency inside the band and with random binary orbital parameters within the ranges defined in Table I. In order to estimate the sensitivity depth at each frequency, we compute the detection efficiency as the proportion of detectable injections in each depth, and estimate the sensitivity using sigmoidal fits and interpolating at which sensitivity depth 95% of the injections are tagged as detected. The procedure is detailed in App. B.

Fig. 6 shows the results for sensitivity depth estimates as a function of frequency for the different selected frequency bands. The mean value across each frequency region (as defined in Table II) is computed from these values and is summarized in Table IV.

VII. SEARCH OUTLIERS FOLLOW-UP

Candidates with CRs above the follow-up thresholds (Table II) in the main stage of the search (see

Region	Frequency [Hz]	$\langle \mathcal{D}^{95\%} \rangle \pm 3\sigma$ [$\mathrm{Hz}^{-1/2}$]
A	[100, 150)	23.3 ± 0.6
B	[150, 170)	22.7 ± 0.5
C	[170, 200)	22.2 ± 0.4
D	[200, 275)	20.4 ± 0.6
E	[275, 350)	19.6 ± 0.7

TABLE IV. Average 95% sensitivity depths across the frequency regions defined in Table II. The uncertainties correspond to $\pm 3\sigma$ from the sigmoidal fit.

Fig. 5) are subjected to a more sensitive follow-up analysis. The follow-up analysis is performed using the `PyFstat` software package [97–100], as was done in the O3a `BinarySkyHough` search [63]. `PyFstat` utilizes the parallel-tempered Markov Chain Monte Carlo (PTMCMC) sampler provided by the `ptemcee` package for the candidate follow-up [101, 102].

This stage uses longer coherence times and includes additional frequency-evolution parameters. Increasing coherence times may also reject potential signals that do not conform to the phase model enforced by the longer coherence lengths [75]. Signals whose spindown is larger than Eq. (5) or whose eccentricity is larger than Eq. (4) are expected to already be lost during the search stage and their high spindowns or eccentricities are not considered inside the parameter ranges of this follow-up stage. Changes to the frequency evolution model due to spin-wandering are not considered in the follow-up.

Increasing T_{coh} strengthens real CWs relative to Gaussian noise because correctly demodulated signals accumulate coherent power with time, while instrumental artifacts, which lack the astrophysical Doppler modulations, are typically diminished by the demodulation and are further rejected by our prominence-crossing and line-list vetoes.

Candidates are analyzed using $\mathcal{F}$-statistic searches [50, 103]. The $\mathcal{F}$-statistic compares data to signal templates in the frequency domain using coherent integration. The semi-coherent version, the segment-wise $2\hat{\mathcal{F}}$, is constructed by summing the coherent $2\tilde{\mathcal{F}}$ statistic over N_{seg} data segments, each with duration T_{coh},

$$2\hat{\mathcal{F}}(\lambda) = \sum_{i=0}^{N_{\mathrm{seg}}-1} 2\tilde{\mathcal{F}}_i(\lambda) \,. \tag{19}$$

In the follow-up process, the MCMC algorithm takes samples using 300 walkers each one with 300 steps to identify and characterize potential maxima, which are then used to determine whether a candidate passes a detection threshold. The MCMC-based follow-up and its application to CW searches is detailed in [104].

In the first stage of the MCMC follow-up, candidates from the initial search are analyzed using a significantly increased coherence time to improve sensitivity. Specifically, we increase the coherence time from the $T_{\mathrm{SFT}} = 1024$ s used in the main search to $T_{\mathrm{coh}} = 12$ hours for the follow-up. This configuration yields a total of $N_{\mathrm{seg}} = 474$ segments over the full observing time. The follow-up priors and MCMC sampler configuration is developed in App. D.

Fig. 7 summarizes the results of the first-stage MCMC follow-up across all frequency bands, showing the maximum recovered $2\hat{\mathcal{F}}$ values as a function of frequency. As seen, most frequency bands show minimums around $2\hat{\mathcal{F}} = 3600$ and maximums around $2\hat{\mathcal{F}} = 3900$. However, there are bands where the maximum sampled $2\hat{\mathcal{F}}$ is much higher above 3900. A large number of them appear near the instrumental disturbances around 270 Hz, which indicates that instrumental lines can highly increase the sampled $2\hat{\mathcal{F}}$.

To determine which candidates should advance to a more sensitive second follow-up stage, we calibrated a threshold on the cumulative $2\hat{\mathcal{F}}$ using simulated signal injections. These injections were generated with the same setup and randomized amplitudes described in the Sec VI. The simulated signals were injected at the sensitivity depths values obtained per each region shown in Table IV. For each injected signal, we recorded the maximum cumulative $2\hat{\mathcal{F}}$ value across all walkers within the corresponding frequency band. By repeating this process for many injections across different frequency bands, sampling at least one band every 5 Hz and covering all regions listed in Table II at the depths given in Table IV, we built up the distribution of recovered $2\hat{\mathcal{F}}$ values, which was then used to set the threshold. After running 14750 injections, the detection threshold was then set at $2\hat{\mathcal{F}} = 3850$, chosen such that fewer than 0.013% of the injected signals (2 of the 14750) would fall below it.

Only injections that were tagged as detected by the search pipeline were followed-up to determine this threshold. Furthermore, the injection follow-up was performed with the same MCMC sampler configuration and priors for the search candidates.

The injection results are shown in Fig. 8. Candidates passing this initial $2\hat{\mathcal{F}}$ cut are then subjected to a second follow-up stage with a longer coherence time, following the methodology outlined in [97, 105, 106].

After running the first-stage MCMC follow-up and applying the cumulative $2\hat{\mathcal{F}}$ threshold, several outliers remained, as summarized in Table V. These surviving outliers were further analyzed to determine whether they are consistent with astrophysical signals or can be attributed to instrumental origins.

CW signals are expected to accumulate $2\hat{\mathcal{F}}$ linearly over time, adding to the segment-wise $2\hat{\mathcal{F}}$ in a relatively uniform way across the observation period. However, if a candidate's frequency evolution briefly overlaps with a strong instrumental disturbance or narrow-band spectral line, it may produce a spike in $2\tilde{\mathcal{F}}$ during that specific time window, while remaining at background levels otherwise.

To identify such cases, we examine the segment-wise $2\tilde{\mathcal{F}}$ distributions of surviving candidates. Following the same approach used in the O3a search, we flag

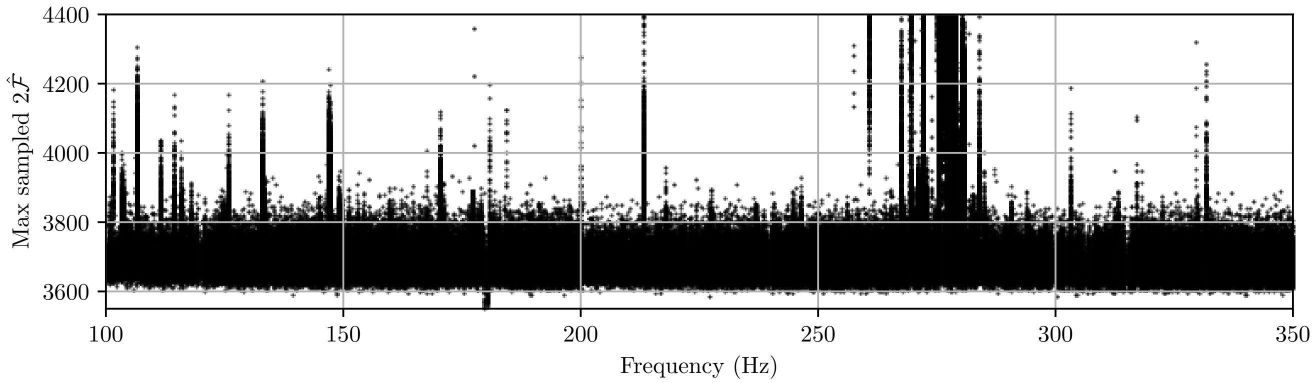

FIG. 7. Results of the first-stage MCMC follow-up. The figure shows the maximum $2\hat{\mathcal{F}}$ values recovered for each candidate, plotted as a function of frequency.

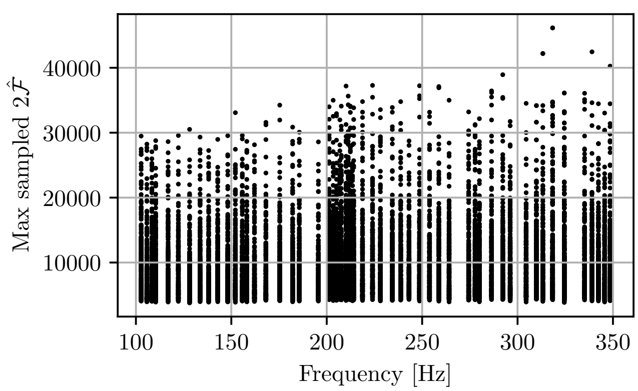

FIG. 8. First-stage MCMC follow-up results on injection studies with $T_{\rm coh} = 12$ h. Each point corresponds to the maximum $2\hat{\mathcal{F}}$ value sampled for each injected signal. 14750 Injections were run, with 2 obtaining a final $2\hat{\mathcal{F}}$ below 3850. Signals were injected at the sensitivity depths values obtained per each region shown in Table IV.

any candidates in bands with at least one segment-wise $2\tilde{\mathcal{F}}$ value exceeding 100. These outliers are classified as "prominence-crossing" cases and are likely caused by transient overlaps with lines or short-lived artifacts rather than persistent astrophysical signals. All candidates within-bands that are tagged as prominence-crossing are discarded in this stage and not followed-up.

Notice that this prominence-crossing veto is necessary even if the number-count statistic has previously been used in the candidate selection. Using the number-count during the search provides more importance to candidates consistent with high power across the observing run. Nonetheless, it is not a filter that eliminates all candidates whose high power is a consequence of crossing paths with an instrumental artifact.

An example is shown in Fig. 9, where the candidate band exhibits a sharp and isolated $2\tilde{\mathcal{F}}$ spike near day 150 of the run. While the total $2\hat{\mathcal{F}}$ surpasses the threshold, the strong deviation in a single segment suggests a transient artifact rather than a genuine signal, and the candidate is therefore discarded.

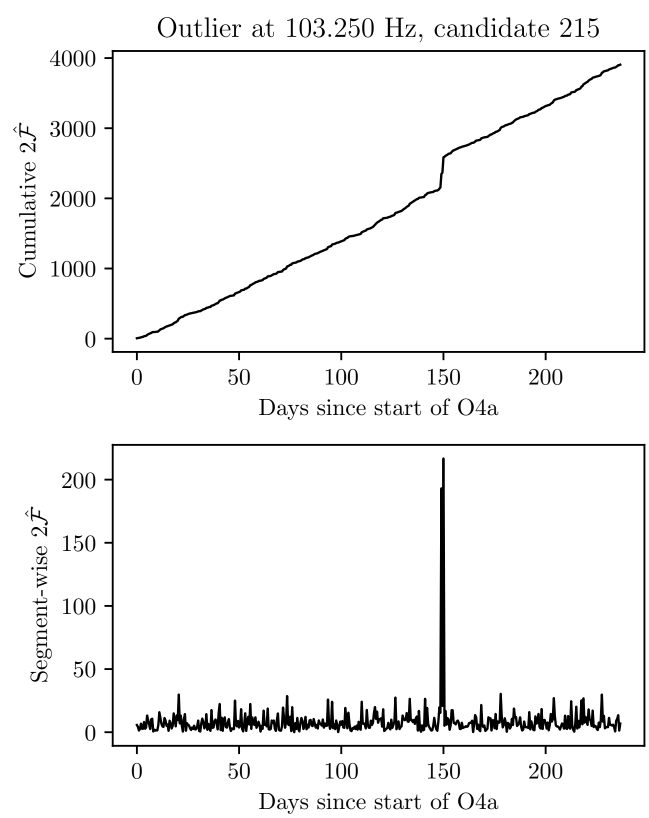

FIG. 9. Example of a prominence-crossing outlier. The candidate shows a large spike in $2\tilde{\mathcal{F}}$ near day 150 of the observing run. This spike allows it to exceed the follow-up threshold of $2\hat{\mathcal{F}} = 3850$, but the narrow change suggests a superposition with an instrumental disturbance. This candidate is therefore discarded from second-stage follow-up.

The broader distribution of such outliers is summarized in Fig. 10. The top panel shows those candidates that have been tagged as prominence-crossing and rejected; they tend to be clustered within a few narrow frequency ranges and exhibit significantly elevated $2\hat{\mathcal{F}}$ values. The bottom panel shows the remaining 1,997 outliers, which passed all veto criteria and are retained for further second-stage follow-up analysis. The results from this prominence crossing veto are summarized in Table V.

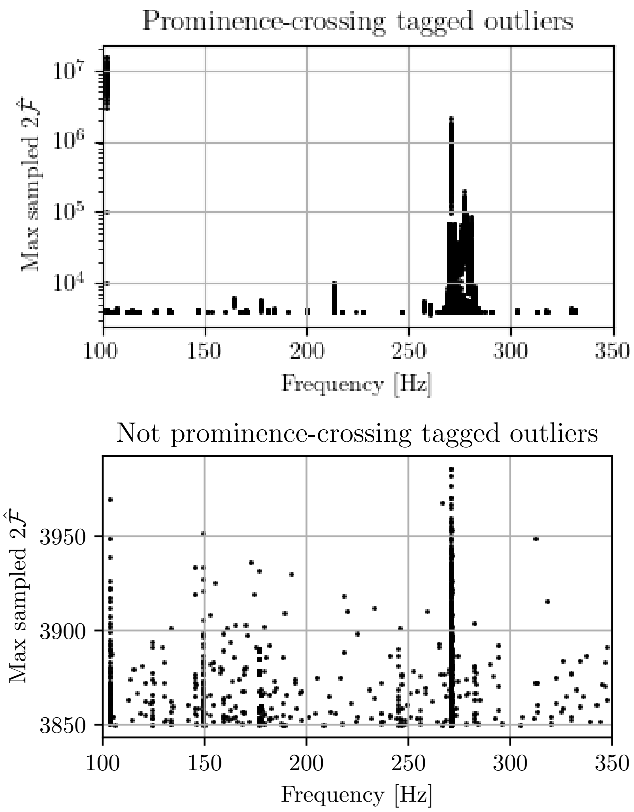

FIG. 10. Distribution of maximum $2\hat{\mathcal{F}}$ values for surviving outliers. The top panel shows outliers tagged as prominence-crossing and discarded due to transient spectral contamination. These candidates tend to cluster in a few frequency bands and exhibit extremely high $2\hat{\mathcal{F}}$ values. The bottom panel shows the remaining outliers, which were not flagged as line-crossing and are retained for further analysis.

Of the 251,717 surviving candidates in Table V, 84% come from the frequency range between 260 Hz and 280 Hz, a range with a high amount of high-CR results as seen in Fig. 4 where there is also a high amount of vetoed bands as seen in Fig. 5. It appears that there is a high amount of broad artifacts in the range, not all of them vetoed in Sec. V.

The second-stage follows the multi-stage procedure established in previous works [97, 105, 106]. In this second follow-up stage, we use a longer coherence time of $T_{\mathrm{coh}} = 26$ h, which increases the sensitivity of the search and improves the accuracy of parameter estimation. The rationale for this choice, together with the details of the priors and analysis setup, which runs again 300 walkers with 300 steps each, is provided in App. D.

Follow-up Summary	**Count**
Total candidates followed up	927,443
Candidates surviving $2\hat{\mathcal{F}} > 3850$	251,717
- Prominence crossings (discarded)	249,720
- Surviving to 2nd stage	1,997

TABLE V. Summary of candidate outcomes from the first-stage MCMC follow-up. Of the 927,443 candidates analyzed, 251,717 exceeded the threshold $2\hat{\mathcal{F}} > 3850$, yielding a survival rate of 27.14%. Among these, 249,720 were tagged as prominence or prominence crossings and discarded, while 1,997 (8%) were retained for second-stage follow-up.

The second stage threshold for further follow-ups was calibrated using software injections as in the first stage. Fig. 11 shows the maximum $2\hat{\mathcal{F}}$ values sampled by the MCMC for each injected signal. The lowest sampled value for detectable signals was close to 2200, indicating that a threshold of 2100 would give a false dismissal rate below 1/14000, given the 14000 injections run.

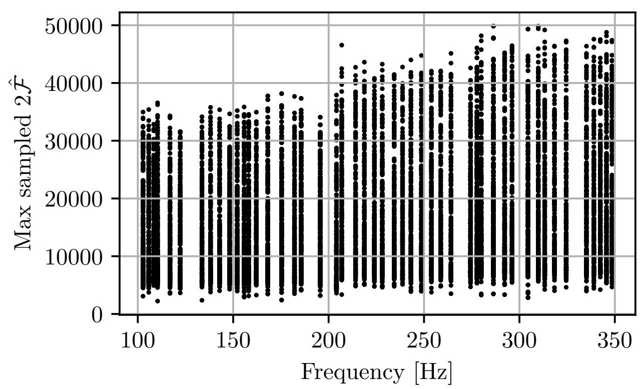

FIG. 11. Second-stage MCMC follow-up results on injection studies $T_{\mathrm{coh}} = 26$ h. Each dot represents the maximum sampled $2\hat{\mathcal{F}}$ value for a detected injection across multiple frequency bands. A total of 14000 injections are shown. Signals were injected at the sensitivity depths values obtained per each region shown in Table IV.

The second-stage pipeline was applied to the 1,997 candidates that survived the first stage. The results are shown in Fig. 12. None of the recovered maximum $2\hat{\mathcal{F}}$ values exceeded the calibrated threshold of 2100. As seen again in Fig. 5, there is a high amount of instrumental disturbances around 270 Hz which have been vetoed in this stage. All recovered values were well below the injection minimum of 2200, and thus none of these outliers are consistent with a detectable CW signal.

Since no candidate survives the second-stage threshold, no further follow-up stages have been carried out. The

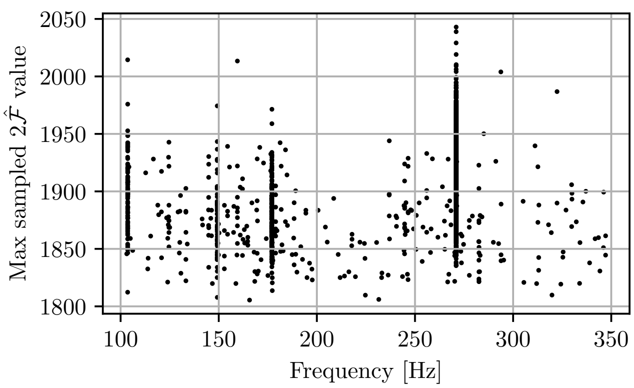

FIG. 12. Maximum $2\hat{\mathcal{F}}$ values recovered from the second-stage MCMC follow-up for each of the 1,997 candidates. No outlier exceeds the detection threshold.

follow-up phase of the search concludes with no candidate consistent with an astrophysical CW source.

VIII. DISCUSSION

This analysis is the first large-scale application of the `fasttracks` pipeline [72, 89], designed to compute detection statistics with GPU acceleration using SFT-type data. To address the large parameter space of the search, we used a novel box-based partitioning strategy also introduced in [72], in which each parameter-space partition, or box, is analyzed independently. This novel partitioning makes post-processing more straightforward, since contaminated boxes can be vetoed and candidates from each box followed up independently. Whereas previous searches required clustering strategies to filter large numbers of candidates and group those likely originating from the same source, our approach achieves comparable reduction in a simpler manner.

A two-step search approach has been used, with a Hough number count filter in the first step to prioritize candidates showing persistent power accumulation. Using the O4a lines list, frequency bands were checked for line contamination and those with more than 2000 candidates and known line contamination were vetoed.

The surviving 27.14% of candidates after the known lines veto were analyzed using an MCMC follow-up method using the `PyFstat` package [97–100] and $T_{\rm coh} =$ 12 h. These candidates were checked to determine if their high statistical values were due to prominence-crossing behavior. Those deemed as not prominence-crossing (8%) were re-analyzed with a second stage follow-up, which concluded the search with no candidates consistent with astrophysical CW sources.

To evaluate the sensitivity of our search, we conducted injection campaigns across all frequency regions, as described in Sec. VI. From these studies, we derived the 95% confidence strain amplitude sensitivity $h_0^{95\%}$, computed from the estimated sensitivity depths and the noise power spectral density shown in Fig. 1. The resulting sensitivity curve is presented in Fig. 13. The best performance was achieved at 199.9 Hz, with $h_0^{95\%} = (1.62 \pm 0.3) \times 10^{-25}$, corresponding to an improvement by a factor 1.5 compared to the lowest amplitude obtained by the previous `BinarySkyHough` search on O3a data [63]. This improvement over the O3a results is consistent with the expectations given the improvement in search sensitivity shown in Fig. 1 and longer observing times plus the improvement in sensitivity depth shown in Fig. 6. These estimates are not applicable to the vetoed frequency ranges listed in Table VI. As in [61], the reported sensitivities are valid for eccentricities below the maximum value defined in Eq. (4), above which the signal track would deviate by more than one frequency bin.

Fig. 14 illustrates the astrophysical reach of this search (in black) derived from the estimated $h_0^{95\%}$ sensitivities and its comparison with the O3a BinarySkyHough search results [63] (in red). The figure shows the distance range (in kiloparsecs) at which NSs with various ellipticities ϵ could be detected, assuming the canonical moment of inertia $I_{zz} = 10^{38}$ kg·m^2. The shaded regions indicate values excluded by being larger than the maximum spin-down used in this search (see Eq. (5)).

Fig. 15 translates these sensitivity results into constraints on the NS ellipticity ϵ, assuming sources are located at fixed distances. For sources within 1 kpc, the ellipticity can be constrained to below 10^{-5} across the majority of the analyzed band (above 130 Hz). These limits begin to probe astrophysically interesting regimes: theoretical expectations for the maximum ellipticity of realistic NSs range from $\sim 10^{-6}$ to 10^{-7} for conventional nuclear equations of state, up to $\sim 10^{-5}$ for more extreme or exotic configurations [4, 107].

Using the ATNF pulsar catalogue [15], we find that of the 3,473 known pulsars, 715 lie within 2 kpc of Earth, 282 within 1 kpc, and 117 within 0.5 kpc. Of these, 151, 66, and 16, respectively, are in binary systems. This confirms that the sensitivity region of our search overlaps with a non-negligible fraction of the known pulsar population, including binaries. Moreover, restricting the nearby binaries to orbital periods between 7 and 15 days and projected semi-major axes between 5 and 15 light-seconds, we identify 17, 8, and 1 such systems within 2 kpc, 1 kpc, and 0.5 kpc, respectively. These are a relative small number of known pulsars probed by the search. Nonetheless, only a small fraction of the Galactic NS population is observable as radio or gamma-ray pulsars [58, 59], with population synthesis models predicting orders of magnitude more NSs than those currently detected. Consequently, our sensitivity may overlap with a much larger, presently unseen NS population, including systems with properties favorable for the emission of CW. Thus, this search directly probes the parameter space occupied by several known binary pulsars, as well as potentially a much larger population of undetected NSs.

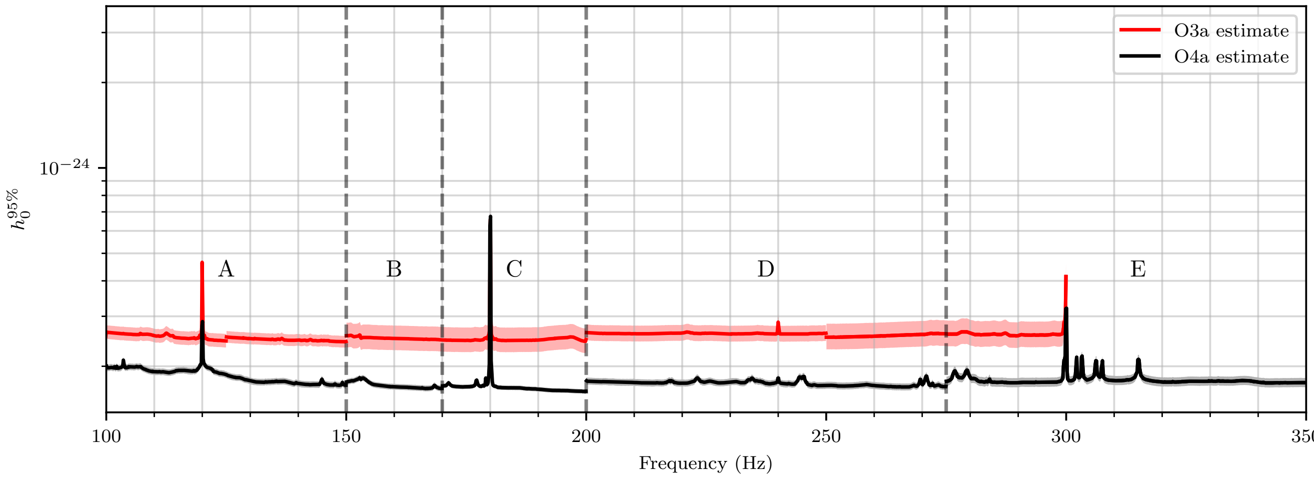

FIG. 13. Estimated 95% strain amplitude sensitivity $h_0^{95\%}$ derived from the sensitivity depths in Table IV, using the inverse square root of the averaged PSD. Comparison between the O3a BinarySkyHough search results [63] (in red), and the results of this present search (in black).

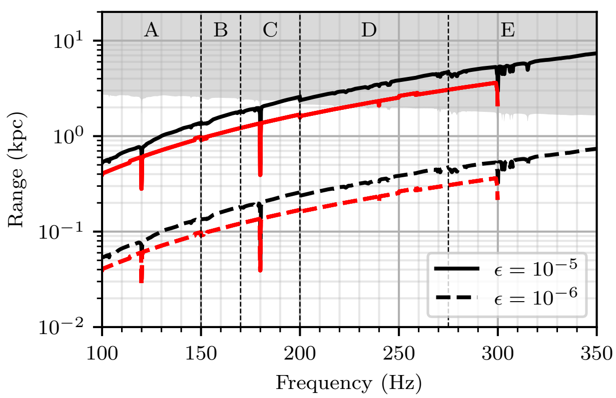

FIG. 14. Estimated distance reach for sources emitting at $h_0^{95\%}$, based on the sensitivity of the search. Shaded regions indicate distances excluded by the limit imposed by the maximum spindown used in the analysis. Comparison between the O3a BinarySkyHough search results [63] (in red), and the results of this present search (in black).

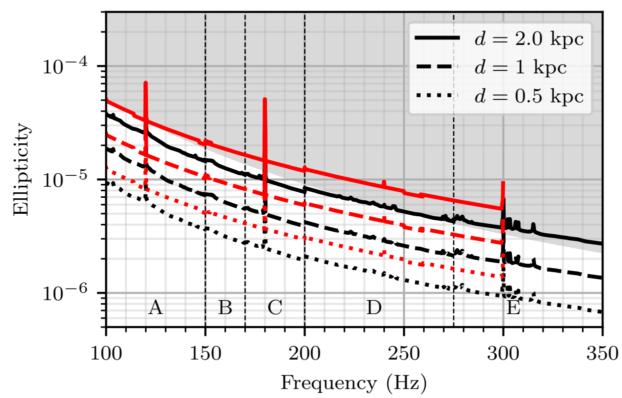

FIG. 15. Corresponding equatorial ellipticities estimated from the $h_0^{95\%}$ sensitivity, assuming a canonical NS moment of inertia $I_{zz} = 10^{38}$ kg·m^2. The shaded regions are excluded by the maximum spindown constraint. Comparison between the O3a BinarySkyHough search results [63] (in red), and the results of this present search (in black).

IX. CONCLUSION

We have conducted an all-sky search for continuous gravitational waves from neutron stars in binary systems using data from the first part of the fourth LIGO-Virgo-KAGRA observing run. The search covered the frequency range from 100 to 350 Hz, targeting systems with projected semi-major axes between 5 and 15 light-seconds and orbital periods between 7 and 15 days.

This work represents the first large-scale application of the `fasttracks` pipeline. We analyzed O4a data with a two-step procedure: a first Hough number count filter to identify persistent candidates, a second step computing weighted normalized power, followed by an MCMC analysis with extended coherence time follow-ups with `PyFstat`. Vetoes of line-contaminated bands reduced the candidate set, however, no signals consistent with astrophysical continuous waves were found. Sensitivity estimates from extensive injection campaigns show a minimum detectable amplitude of $h_0^{95\%} = (1.62 \pm 0.3) \times 10^{-25}$ at 199.9 Hz, representing a 1.5-fold improvement over the lowest amplitude achieved by the previous `BinarySkyHough` search on O3a data [63].

The achieved sensitivity covers binary parameters and spin frequencies consistent with those of many known binary pulsars within a few kiloparsecs, as well as with a potentially much larger unseen neutron star population. Constraints on the ellipticity of nearby sources reach below 10^{-5}, entering the regime predicted by some nuclear equations of state and more exotic neutron star models. The non-detection of continuous gravitational waves at O4 sensitivity imposes strong constraints on neutron stars with exotic compositions within the distance reach of the sources.

Looking ahead, upgrades to the global network of terrestrial gravitational-wave detectors are expected to deliver enhanced strain sensitivity, extended frequency coverage, and longer observing baselines in upcoming observing runs, more so with third-generation detectors such as the Einstein Telescope [108] and Cosmic Explorer [109]. These advancements will increase the chances of detecting CW signals and improve constraints on the galactic neutron star population. Complementary progress will come from next-generation pulsar timing facilities, such as the Square Kilometre Array [110], which will expand the known pulsar population and improve the measurement of their evolution, thereby providing valuable priors and targets for gravitational-wave searches.

ACKNOWLEDGMENTS

This material is based upon work supported by NSF's LIGO Laboratory, which is a major facility fully funded by the National Science Foundation. The authors also gratefully acknowledge the support of the Science and Technology Facilities Council (STFC) of the United Kingdom, the Max-Planck-Society (MPS), and the State of Niedersachsen/Germany for support of the construction of Advanced LIGO and construction and operation of the GEO 600 detector. Additional support for Advanced LIGO was provided by the Australian Research Council. The authors gratefully acknowledge the Italian Istituto Nazionale di Fisica Nucleare (INFN), the French Centre National de la Recherche Scientifique (CNRS) and the Netherlands Organization for Scientific Research (NWO) for the construction and operation of the Virgo detector and the creation and support of the EGO consortium. The authors also gratefully acknowledge research support from these agencies as well as by the Council of Scientific and Industrial Research of India, the Department of Science and Technology, India, the Science & Engineering Research Board (SERB), India, the Ministry of Human Resource Development, India, the Spanish Agencia Estatal de Investigación (AEI), the Spanish Ministerio de Ciencia, Innovación y Universidades, the Red Española de Supercomputación - Barcelona Supercomputing Center - Centro Nacional de Supercomputación (BSC-CNS). the European Union NextGenerationEU/PRTR (PRTR-C17.I1), the ICSC - CentroNazionale di Ricerca in High Performance Computing, Big Data and Quantum Computing, funded by the European Union NextGenerationEU, the Comunitat Autonòma de les Illes Balears through the Conselleria d'Educació i Universitats, the Conselleria d'Innovació, Universitats, Ciència i Societat Digital de la Generalitat Valenciana and the CERCA Programme Generalitat de Catalunya, Spain, the Polish National Agency for Academic Exchange, the National Science Centre of Poland and the European Union - European Regional Development Fund; the Foundation for Polish Science (FNP), the Polish Ministry of Science and Higher Education, the Swiss National Science Foundation (SNSF), the Russian Science Foundation, the European Commission, the European Social Funds (ESF), the European Regional Development Funds (ERDF), the Royal Society, the Scottish Funding Council, the Scottish Universities Physics Alliance, the Hungarian Scientific Research Fund (OTKA), the French Lyon Institute of Origins (LIO), the Belgian Fonds de la Recherche Scientifique (FRS-FNRS), Actions de Recherche Concertées (ARC) and Fonds Wetenschappelijk Onderzoek - Vlaanderen (FWO), Belgium, the Paris Île-de-France Region, the National Research, Development and Innovation Office of Hungary (NKFIH), the National Research Foundation of Korea, the Natural Sciences and Engineering Research Council of Canada (NSERC), the Canadian Foundation for Innovation (CFI), the Brazilian Ministry of Science, Technology, and Innovations, the International Center for Theoretical Physics South American Institute for Fundamental Research (ICTP-SAIFR), the Research Grants Council of Hong Kong, the National Natural Science Foundation of China (NSFC), the Israel Science Foundation (ISF), the US-Israel Binational Science Fund (BSF), the Leverhulme Trust, the Research Corporation, the National Science and Technology Council (NSTC), Taiwan, the United States Department of Energy, and the Kavli Foundation. The authors gratefully acknowledge the support of the NSF, STFC, INFN and CNRS for provision of computational resources.

This work was supported by MEXT, the JSPS Leading-edge Research Infrastructure Program, JSPS Grant-in-Aid for Specially Promoted Research 26000005, JSPS Grant-in-Aid for Scientific Research on Innovative Areas 2402: 24103006, 24103005, and 2905: JP17H06358, JP17H06361 and JP17H06364, JSPS Core-to-Core Program A. Advanced Research Networks, JSPS Grants-in-Aid for Scientific Research (S) 17H06133 and 20H05639, JSPS Grant-in-Aid for Transformative Research Areas (A) 20A203: JP20H05854, the joint research program of the Institute for Cosmic Ray Research, University of Tokyo, the National Research Foundation (NRF), the Computing Infrastructure Project of the Global Science experimental Data hub Center (GSDC) at KISTI, the Korea Astronomy and Space Science Institute (KASI), the Ministry of Science and ICT (MSIT) in Korea, Academia Sinica (AS), the AS Grid Center (ASGC) and the National Science and Technology Council (NSTC) in Taiwan under grants including the Science Vanguard Research Program, the Advanced Technology Center (ATC) of NAOJ, and the Mechanical Engineering Center of KEK.

Additional acknowledgements for support of individual authors may be found in the following document: `https://dcc.ligo.org/LIGO-M2300033/public`. For the purpose of open access, the authors have applied a Creative Commons Attribution (CC BY) license to any Author Accepted Manuscript version arising. We request that citations to this article use 'A. G. Abac *et al.* (LIGO-Virgo-KAGRA Collaboration), ...' or similar phrasing, depending on journal convention.

This paper has been assigned document number LIGO-P2500437.

Appendix A: Parameter-space Partitioning

To estimate the number of templates required to cover a given region of parameter space, we begin with the resolution steps $\delta\lambda[k]$ given by Eq. (13) along each of the parameters in $\lambda = \{f_0, \hat{n}, a_p, \Omega, \phi_\mathrm{b}\}$. The total number of templates within a volume $\Delta\lambda$ is given by

$$\mathcal{N}\left(\Delta\lambda\right) = \int_{\Delta\lambda} d\lambda\rho\left(\lambda\right), \tag{A1}$$

where the local template density, $\rho\left(\lambda\right)$, is defined as [72]

$$\rho\left(\lambda\right) = \prod_{k=1}^{D} \frac{1}{\delta\lambda[k]}, \tag{A2}$$

where k is the running index over the search parameters, up to $D = 6$ in this case.

In order to sample the templates, we perform a coordinate transformation from the physical parameter space λ to a uniform template space ξ, in which the template density is constant. This is achieved by applying the transformation

$$d\lambda\rho(\lambda) = d\xi \quad \Leftrightarrow \quad \rho(\xi) = 1. \tag{A3}$$

which we use to derivate the following relations between the coordinates in the physical and uniform parameter space

$$\begin{aligned}
\xi[0] &= \frac{C^{1/6}}{6} f_0^6 \\
\xi[1] &= C^{1/6}\alpha \\
\xi[2] &= C^{1/6}\sin\delta \\
\xi[3] &= \frac{C^{1/6}}{3} a_\mathrm{p}^3 \\
\xi[4] &= \frac{C^{1/6}}{4}\Omega^4 \\
\xi[5] &= C^{1/6}\phi_\mathrm{b}
\end{aligned} . \tag{A4}$$

with $C = T_\mathrm{SFT}^6 T_\mathrm{obs} (v/c)^2$ (more details can be found in [72]).

In this transformed space, templates are generated by uniform random sampling over the search region. These samples are then mapped back to the physical parameter space λ using the inverse transformation as described in [72]. As a result, the sampling in λ automatically follows the required non-uniform density $\rho(\lambda)$.

The number of templates in a volume region $\Delta\xi$ in the uniform space is simply

$$\mathcal{N}(\Delta\lambda) = \int_{\Delta\xi} d\xi = \prod_{k=1}^{D} \Delta\xi[k]. \tag{A5}$$

To construct the boxes, the algorithm used is as follows:

We begin by estimating the number of sky templates required due to the Doppler modulation induced by Earth's motion. This number depends on the frequency and the resolution of the sky grid, and is given by

$$\mathcal{N}_\mathrm{sky} = \int_\mathrm{sky} \frac{1}{\delta\mathrm{sky}} = 4\pi \left(f_0 T_\mathrm{SFT} \frac{v}{c}\right)^2. \tag{A6}$$

We then divide the sky into smaller patches so that each sky patch contains a fixed number of templates. We chose for each sky patch a small number of templates, ≈ 9, in order to ensure that all templates in one box were spatially close to each other. Hence, the total number of sky boxes is

$$B_\mathrm{sky} = \frac{\mathcal{N}_\mathrm{sky}}{9}. \tag{A7}$$

We split both sky coordinate parameters into the same number of subdivisions,

$$B_{\alpha,\sin\delta} = \mathrm{round}\left(\sqrt{B_\mathrm{sky}}\right), \tag{A8}$$

and then calculate the number of templates assigned to each sky box

$$\mathcal{N}_\text{per sky box} = \frac{\mathcal{N}_\mathrm{total}\mathcal{O}}{B_{\alpha,\sin\delta}^2}. \tag{A9}$$

where $\mathcal{O}$ is the oversampling factor for a given frequency band and $\mathcal{N}_\mathrm{total}$ the total amount of templates in the frequency band, computed using Eq. (A5). The amount $B_{\alpha,\sin\delta}$ per band is increased in discrete steps according to the increasing frequency (see Eq. A8). We start at 100 Hz with 12^2 sky boxes ending with 42^2 at 350 Hz.

We also tune the number of subdivisions in the frequency and binary parameters so that each box contains approximately 10^8 templates. This limit was enforced by the maximum number of templates that we were able to process at the same time in parallel in a modern NVIDIA A100 Tensor Core GPU as described in [72]. Maximizing the number of templates to be processed for the efficient use of GPU resources.

Hence, we partition the following three parameters: frequency f_0, projected semi-major axis a_p, and orbital frequency Ω, into an equal number of subdivisions ($B_{f_0} = B_{a_p} = B_\Omega \equiv B_{f_0,a_p,\Omega}$). The quantity $B_{f_0,a_p,\Omega}$

per frequency band is illustrated in Fig. 16. Additionally, orbital phase parameter ϕ_b is not subdivided, it is sampled over its full physical range within each box. The total number of boxes is

$$B_{\rm total} = B^2_{\alpha,\sin\delta} B^3_{f_0,a_p,\Omega}, \tag{A10}$$

and number of templates per box is

$$\mathcal{N}_{\rm box} = \frac{\mathcal{N}_{\rm total}\mathcal{O}}{B_{\rm total}} = \frac{\mathcal{N}_{\rm total}\mathcal{O}}{B^2_{\alpha,\sin\delta} B^3_{f_0,a_p,\Omega}}. \tag{A11}$$

As a consequence, the division of these three parameters is done according to

$$B_{f_0,a_p,\Omega} = \text{round}\left(\sqrt[3]{\frac{\mathcal{N}_{\rm total}\mathcal{O}}{\mathcal{N}_{\rm box} B^2_{\alpha,\sin\delta}}}\right), \tag{A12}$$

per each 0.125 Hz band, where $\mathcal{N}_{\rm box} = 10^8$.

We ensured that boxes were sufficiently small, in order to avoid that possible contaminations in one of them affected a large region in parameter space, by defining a minimum of 10^4 boxes per frequency band: if the resulting $\mathcal{N}_{\rm box}$ from Eq. (A11) is less than 10^4, we further subdivided the frequency and binary parameter space by incrementing $B_{f_0,a_p,\Omega}$ according to

$$B_{f_0,a_p,\Omega} = \left\lceil \sqrt[3]{\frac{B_{\rm min}}{B^2_{\alpha,\sin\delta}}} \right\rceil. \tag{A13}$$

The total amount of boxes per frequency band is illustrated in Fig. 3, and the number of templates per box in Fig. 17.

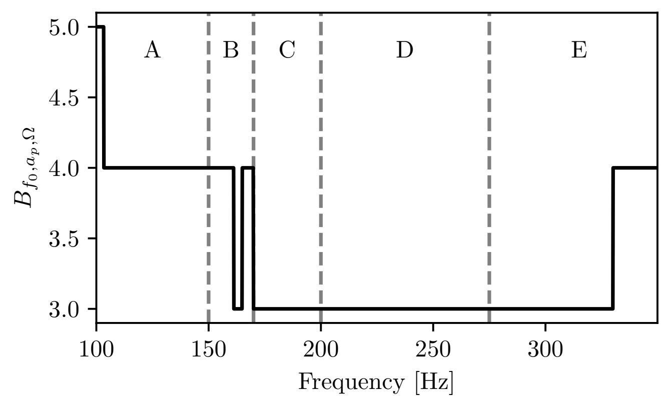

FIG. 16. Number of subdivisions in the intrinsic frequency f_0, projected semi-major axis a_p, and orbital frequency Ω dimensions per 0.125 Hz frequency band. The lettered regions (A-E) correspond to the frequency intervals defined in Table II. Four major transitions can be observed, with different oversampling factors. The first two drops in the number of subdivisions (near 100 Hz and between 170-200 Hz) are due to the enforcement of a minimum total number of 10^4 boxes. The drop at 170 Hz is due to a change in oversampling. At 174 Hz there is another increase because the amount of templates per box is above 1.5×10^8, hence, another subdivision is added to round the number closer to 10^8. The sharp increase beyond 300 Hz is instead driven by the 10^8 templates-per-box criterion.

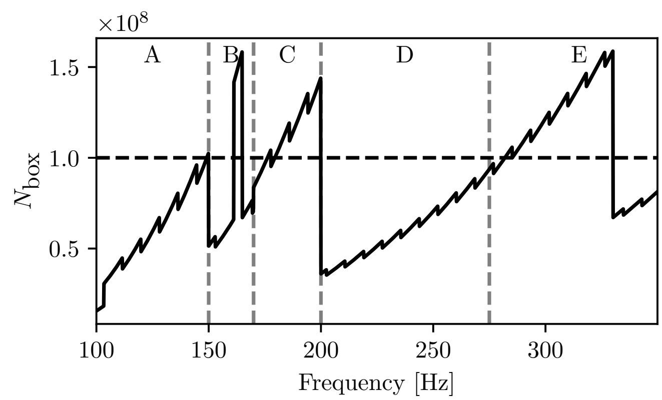

FIG. 17. Number of templates per box $\bar{\mathcal{N}}_{\rm box}$ as a function of frequency. The white dashed line marks the target threshold of 10^8 templates per box. The five lettered regions (A-E) match the frequency intervals defined in Table II. The sawtooth pattern arises due to rounding of box counts and the adaptive balancing of box size to the minimum amount of boxes and templates per box criteria as shown in Fig. 16.

Appendix B: Fitting Sensitivity Estimation

In this appendix, we describe the procedure used to estimate the search sensitivity shown in Sec. VI. Our goal is to quantify the amplitude of CW signals that the search could detect with 95% efficiency across different frequency bands. This is done by performing a large number of signal injection studies and analyzing their recovery.

After separating detected and non-detected injections, we construct efficiency-versus-depth curves by using six different sensitivity depths. For each depth $\mathcal{D}$, the detection efficiency E is defined as the fraction of successfully detected injections out of the total N performed (500 for each sensitivity depth). Its statistical uncertainty is assigned as

$$\delta E = \sqrt{\frac{E(1-E)}{N}}, \tag{B1}$$

the standard error of a proportion when counting successes in a set of independent trials.

To extract the sensitivity depth corresponding to 95% detection efficiency ($\mathcal{D}^{95\%}$), we fit a sigmoid function to the efficiency-versus-depth data. The fit is performed using the `curve_fit` function from `SciPy` [111], with the form

$$S(\mathcal{D};a,b) = \frac{1}{1+\exp\left(\frac{\mathcal{D}-b}{a}\right)}, \tag{B2}$$

where a and b are shape parameters. The 95% sensitivity

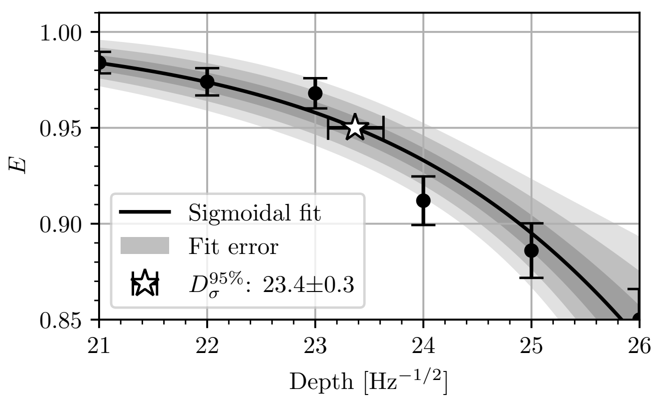

FIG. 18. Example of 95% sensitivity depth interpolation at 105.75 Hz (Region A, oversampling = 4.0, threshold $\Psi_s > 7.0$). Circles indicate injection results, the black line shows the sigmoidal fit, and shaded bands represent 1, 2, and 3σ confidence intervals. The star denotes the estimated $\mathcal{D}^{95\%}$ with its $\pm\sigma$ uncertainty.

depth is given by the value of $\mathcal{D}$ for which $S(\mathcal{D}; a, b) = 0.95$.

The uncertainty in the sigmoidal fit is propagated from the covariance matrix C as

$$\sigma_S(\mathcal{D}) = \sqrt{\left(\frac{\partial S}{\partial a}\right)^2 C_{aa} + \left(\frac{\partial S}{\partial b}\right)^2 C_{bb} + 2\frac{\partial S}{\partial a}\frac{\partial S}{\partial b}C_{ab}}, \tag{B3}$$

and the error in the $\mathcal{D}^{95\%}$ is done by bisecting the curves defined by $S(\mathcal{D}; a, b) \pm \sigma_S(\mathcal{D})$ with $E = 0.95$.

In Fig. 18, we show a representative example of the efficiency curve fit used to estimate the 95% sensitivity depth, $\mathcal{D}^{95\%}$, and its error. The 95% depth and its $\pm\sigma$ uncertainty are extracted from the fit and indicated with a star.

Appendix C: Vetoed frequency ranges

The total contaminated frequency range surrounding a line is given by

$$f_{\text{contaminated}} = f_{\text{line}} \pm (\Delta f_{\text{line}} + f_{\text{wings}}), \tag{C1}$$

where Δf_{line} is the width towards each side of the line (left width towards lower frequencies and right width towards higher ones), and f_{wings} accounts for the maximum Doppler excursion, computed as

$$f_{\text{wings}} = f_{\text{line}}\left(\frac{v}{c} + a_p\Omega\right). \tag{C2}$$

We provide in this appendix Table VI, which contains a list of the frequency ranges which have been vetoed as described in Sec. V. The contamination range caused by each line has been calculated using Eq. (C1). Outliers from the search in these ranges have been vetoed and have not been followed up in the stage discussed in Sec. VII.

Appendix D: Outlier follow-up setup

1. First-step follow-up setup

For the follow-up first stage, we employ 300 walkers with 300 steps per walker. This setup is not expected to achieve full convergence of the MCMC chains. Nonetheless, it is sufficient for our purpose of identifying promising candidates. Better convergence of the MCMC chains is expected to take place if further stages in case a CW signal is detected.

We also add two additional frequency-evolution parameters to be searched over. The first one is the orbital eccentricity e. Due to considering non-zero eccentricities, the full frequency-evolution equation for the CW signal is [61]

$$f(t;\lambda) = f_0\Bigg\{1 + \frac{\vec{v}(t)}{c}\cdot\hat{n} - a_p\Omega\Bigg(\cos\left[\Omega\left(t - t_{\text{asc}}\right)\right] + e\cos\left[\omega + 2\Omega\left(t - t_{\text{asc}}\right)\right]\Bigg)\Bigg\}. \tag{D1}$$

The addition of eccentricity necessitates also the inclusion of the argument of periapsis ω. Furthermore, the first stage is done with the time of periastron passage t_p instead of the time of ascending node t_{asc}, since this is the search parameter implemented in the MCMC using `PyFstat` package [97–100]. These two are related through

$$t_{\text{asc}} = t_p - \frac{\omega}{\Omega}, \tag{D2}$$

where the orbital phase ϕ_{b} can be calculated as

$$\phi_{\text{b}} = \Omega t_{\text{asc}}. \tag{D3}$$

The priors used for this stage are uniform over intervals centered on the candidate parameters. The size of these prior regions is determined by the resolution Eq. (13), (18). Specifically, the frequency f_0 is taken within ±1.5 resolution intervals, the sky position (α, δ) and the orbital period P within ±3 resolution intervals, where the orbital period resolution is given by

$$\delta P = \frac{P^2\delta\Omega}{2\pi} \tag{D4}$$

The projected semi-major axis a_p prior is within ±1 resolution interval, the orbital phase reference time t_p is allowed to vary over the full orbital period, while the argument of periapsis ω spans the full range $[0, 2\pi]$. The eccentricity e is drawn from the range $[0, e^{\max}]$, where $e^{\max}$ is the maximum value to which the search is sensitive, given by Eq. (4). When the resulting prior boundaries extend beyond the physical limits of a parameter, such as δ exceeding $\pi/2$, they are truncated to ensure that no samples fall outside.

2. Second-stage follow-up setup

In the second stage, both the coherence time and the priors are modified. The higher coherence time makes the parameter-space "peak" of the signal higher and narrower. For that reason, the priors are also modified with smaller intervals. One additional parameter, the possible spindown or spin-up of the signal, $|\dot{f}_0|$, is also added to this stage.

As shown in [106], the coherence time for stage j is given by

$$T_{\rm coh}^{(j)} = \mathcal{N}_*^{j/D} T_{\rm coh}^{(0)}, \tag{D5}$$

where we take $\mathcal{N}_* = 10^3$ as in [106], D is the number of resolvable parameters, and $T_{\rm coh}^{(0)}$ is the coherence time used in the first stage (12 hours). For the second stage, the additional parameter of the frequency spindown $\dot{f}_0$ is introduced, increasing the number of dimensions to $D = 9$. This gives a second-stage coherence time of approximately 26 hours, corresponding to $N_{\rm seg} = 219$ segments (down from $N_{\rm seg} = 474$ in the first stage).

In the second stage, the priors are Gaussian distributions centered on the candidate values recovered from the first stage, with narrower widths than those used previously. These gaussian priors allow for the exploration beyond the expected location if the true signal lies slightly further away. Specifically, the frequency f_0 has a Gaussian width of $\delta f_0/6$, right ascension α a width of $\delta\alpha/3$, and declination δ a width of $\delta\delta/3$. The projected semi-major axis a_p is assigned a width of $\delta a_p/9$, the orbital period P a width of $\delta P/3$, the time of ascending node t_p a width of $5\delta t_p/3$, the eccentricity e a width of $\delta e/9$, and the argument of periapsis ω a width of $\delta\omega/9$. The spindown $|\dot{f}_0|$ is instead given a uniform prior between minus the maximum and the maximum spindown for which the search remains sensitive, given in Eq. (5), allowing both positive (spin-up) and negative (spindown) values. When the Gaussian support extends beyond physical limits, such as when the center ± ten times the width falls outside the allowed physical or search ranges, the prior is replaced with a uniform distribution covering only the physically valid region.

These prior widths ensure that roughly 99.7% (3σ) of the initial walker distribution lies within one-third of the prior volume used in the first stage. The resolution formulas for the additional parameters introduced in this stage are

$$\delta t_{\rm asc} = \frac{1}{T_{\rm SFT} f_0 a_p \Omega^2}, \tag{D6}$$

$$\delta e = \frac{1}{T_{\rm SFT} f_0 a_p \Omega}, \tag{D7}$$

$$\delta\omega = \frac{1}{T_{\rm SFT} f_0 a_p \Omega e}. \tag{D8}$$

The sampler configuration is kept consistent with the first stage, using the `ptemcee` algorithm with 300 walkers and 300 steps per walker.

[1] K. Riles, Searches for continuous-wave gravitational radiation, Living Rev. Rel. **26**, 3 (2023), arXiv:2206.06447 [astro-ph.HE].

[2] M. Sieniawska and M. Bejger, Continuous gravitational waves from neutron stars: current status and prospects, Universe **5**, 217 (2019), arXiv:1909.12600 [astro-ph.HE].

[3] P. D. Lasky, Gravitational Waves from Neutron Stars: A Review, Publ. Astron. Soc. Austral. **32**, e034 (2015), arXiv:1508.06643 [astro-ph.HE].

[4] G. Ushomirsky, C. Cutler, and L. Bildsten, Deformations of accreting neutron star crusts and gravitational wave emission, Mon. Not. Roy. Astron. Soc. **319**, 902 (2000), arXiv:astro-ph/0001136.

[5] C. J. Horowitz, Gravitational Waves From Low Mass Neutron Stars, Physical Review D **81**, 103001 (2010), arXiv:0912.1491 [astro-ph.SR].

[6] L. Bildsten, Gravitational radiation and rotation of accreting neutron stars, Astrophys. J. Lett. **501**, L89 (1998), arXiv:astro-ph/9804325.

[7] N. Andersson, A New class of unstable modes of rotating relativistic stars, Astrophysics Journal **502**, 708 (1998), arXiv:gr-qc/9706075.

[8] N. Andersson, Gravitational waves from instabilities in relativistic stars, Classical and Quantum Gravity **20**, R105 (2003), arXiv:astro-ph/0211057.

[9] C. Van Den Broeck, The Gravitational wave spectrum of non-axisymmetric, freely precessing neutron stars, Classical and Quantum Gravity **22**, 1825 (2005), arXiv:gr-qc/0411030.

[10] J. A. Morales and C. J. Horowitz, Neutron star crust can support a large ellipticity, Mon. Not. Roy. Astron. Soc. **517**, 5610 (2022), arXiv:2209.03222 [gr-qc].

[11] J. Soldateschi, N. Bucciantini, and L. Del Zanna, Quasi-universality of the magnetic deformation of neutron stars in general relativity and beyond, Astron. Astrophys. **654**, A162 (2021), arXiv:2106.00603 [astro-ph.HE].

[12] A. Colaiuda, V. Ferrari, L. Gualtieri, and J. A. Pons, Relativistic models of magnetars: structure and deformations, Mon. Not. Roy. Astron. Soc. **385**, 2080 (2008), arXiv:0712.2162 [astro-ph].

[13] G. Woan, M. D. Pitkin, B. Haskell, D. I. Jones, and P. D. Lasky, Evidence for a Minimum Ellipticity in Millisecond Pulsars, Astrophys. J. Lett. **863**, L40 (2018), arXiv:1806.02822 [astro-ph.HE].

[14] B. Haskell and M. Bejger, Astrophysics with continuous gravitational waves, Nature Astron. **7**, 1160 (2023).

[15] R. N. Manchester, G. B. Hobbs, A. Teoh, and M. Hobbs, The Australia Telescope National Facility pulsar catalogue, Astron. J. **129**, 1993 (2005), arXiv:astro-ph/0412641.

[16] A. I. Chugunov, M. E. Gusakov, and E. M. Kantor,

New possible class of neutron stars: hot and fast non-accreting rotators, Monthly Notices of the Royal Astronomical Society **445**, 385 (2014), arXiv:1408.6770 [astro-ph.HE].

[17] A. M. Holgado, P. M. Ricker, and E. A. Huerta, Gravitational Waves from Accreting Neutron Stars Undergoing Common-envelope Inspiral, The Astrophysical Journal **857**, 38 (2018), arXiv:1706.09413 [astro-ph.HE].

[18] F. Gittins and N. Andersson, Modelling neutron star mountains in relativity, Monthly Notices of the Royal Astronomical Society **507**, 116 (2021), arXiv:2105.06493 [astro-ph.HE].

[19] F. Gittins, Gravitational waves from neutron-star mountains, Class. Quant. Grav. **41**, 043001 (2024), arXiv:2401.01670 [gr-qc].

[20] P. H. B. Rossetto, J. Frauendiener, R. Brunet, and A. Melatos, Magnetically confined mountains on accreting neutron stars in general relativity, Mon. Not. Roy. Astron. Soc. **526**, 2058 (2023), arXiv:2309.09519 [astro-ph.HE].

[21] R. Tenorio, D. Keitel, and A. M. Sintes, Search Methods for Continuous Gravitational-Wave Signals from Unknown Sources in the Advanced-Detector Era, Universe **7**, 474 (2021), arXiv:2111.12575 [gr-qc].

[22] O. J. Piccinni, Status and Perspectives of Continuous Gravitational Wave Searches, Galaxies **10**, 72 (2022), arXiv:2202.01088 [gr-qc].

[23] K. Wette, Searches for continuous gravitational waves from neutron stars: A twenty-year retrospective, Astropart. Phys. **153**, 102880 (2023), arXiv:2305.07106 [gr-qc].

[24] A. G. Abac *et al.* (LIGO, Virgo, KAGRA), Search for Continuous Gravitational Waves from Known Pulsars in the First Part of the Fourth LIGO-Virgo-KAGRA Observing Run, Astrophys. J. **983**, 99 (2025), arXiv:2501.01495 [astro-ph.HE].

[25] R. Abbott *et al.* (LIGO, Virgo, KAGRA), Model-based Cross-correlation Search for Gravitational Waves from the Low-mass X-Ray Binary Scorpius X-1 in LIGO O3 Data, Astrophys. J. Lett. **941**, L30 (2022), arXiv:2209.02863 [astro-ph.HE].

[26] R. Abbott *et al.* (LIGO, Virgo, KAGRA), Search for gravitational waves from Scorpius X-1 with a hidden Markov model in O3 LIGO data, Phys. Rev. D **106**, 062002 (2022), arXiv:2201.10104 [gr-qc].

[27] R. Abbott *et al.* (LIGO, Virgo, KAGRA), All-sky search for continuous gravitational waves from isolated neutron stars using Advanced LIGO and Advanced Virgo O3 data, Phys. Rev. D **106**, 102008 (2022), arXiv:2201.00697 [gr-qc].

[28] R. Abbott *et al.* (LIGO, Virgo, KAGRA), Narrowband Searches for Continuous and Long-duration Transient Gravitational Waves from Known Pulsars in the LIGO-Virgo Third Observing Run, Astrophys. J. **932**, 133 (2022), arXiv:2112.10990 [gr-qc].

[29] R. Abbott *et al.* (LIGO, Virgo), Search of the early O3 LIGO data for continuous gravitational waves from the Cassiopeia A and Vela Jr. supernova remnants, Phys. Rev. D **105**, 082005 (2022), arXiv:2111.15116 [gr-qc].

[30] R. Abbott *et al.* (LIGO, Virgo, KAGRA), All-sky search for gravitational wave emission from scalar boson clouds around spinning black holes in LIGO O3 data, Phys. Rev. D **105**, 102001 (2022), arXiv:2111.15507 [astro-ph.HE].

[31] R. Abbott *et al.* (LIGO, Virgo, KAGRA), Searches for Gravitational Waves from Known Pulsars at Two Harmonics in the Second and Third LIGO-Virgo Observing Runs, Astrophys. J. **935**, 1 (2022), arXiv:2111.13106 [astro-ph.HE].

[32] R. Abbott *et al.* (LIGO, Virgo, KAGRA), Search for continuous gravitational waves from 20 accreting millisecond x-ray pulsars in O3 LIGO data, Phys. Rev. D **105**, 022002 (2022), arXiv:2109.09255 [astro-ph.HE].

[33] R. Abbott *et al.* (LIGO, Virgo, KAGRA), All-sky search for continuous gravitational waves from isolated neutron stars in the early O3 LIGO data, Phys. Rev. D **104**, 082004 (2021), arXiv:2107.00600 [gr-qc].

[34] R. Abbott *et al.* (LIGO, Virgo, KAGRA), Searches for Continuous Gravitational Waves from Young Supernova Remnants in the Early Third Observing Run of Advanced LIGO and Virgo, Astrophys. J. **921**, 80 (2021), arXiv:2105.11641 [astro-ph.HE].

[35] R. Abbott *et al.* (LIGO, Virgo, KAGRA), Constraints from LIGO O3 Data on Gravitational-wave Emission Due to R-modes in the Glitching Pulsar PSR J0537–6910, Astrophys. J. **922**, 71 (2021), arXiv:2104.14417 [astro-ph.HE].

[36] R. Abbott *et al.* (LIGO, Virgo, KAGRA), Diving below the Spin-down Limit: Constraints on Gravitational Waves from the Energetic Young Pulsar PSR J0537-6910, Astrophys. J. **913**, L27 (2021), arXiv:2012.12926 [astro-ph.HE].

[37] J. Ming, M. A. Papa, H.-B. Eggenstein, B. Beheshtipour, B. Machenschalk, R. Prix, B. Allen, and M. Bensch, Deep Einstein@Home Search for Continuous Gravitational Waves from the Central Compact Objects in the Supernova Remnants Vela Jr. and G347.3-0.5 Using LIGO Public Data, Astrophys. J. **977**, 154 (2024), arXiv:2408.14573 [gr-qc].

[38] B. Steltner, M. A. Papa, H. B. Eggenstein, R. Prix, M. Bensch, B. Allen, and B. Machenschalk, Deep Einstein@Home All-sky Search for Continuous Gravitational Waves in LIGO O3 Public Data, Astrophys. J. **952**, 55 (2023), arXiv:2303.04109 [gr-qc].

[39] B. McGloughlin, J. Martins, B. Steltner, M. Alessandra Papa, H.-B. Eggenstein, B. Machenschalk, R. Prix, and M. Bensch, Einstein@Home all-sky "bucket" search for continuous gravitational waves in LIGO O3 public data, arXiv e-prints , arXiv:2508.16423 (2025), arXiv:2508.16423 [gr-qc].

[40] B. McGloughlin, B. Steltner, J. Martins, M. Alessandra Papa, H.-B. Eggenstein, J. Ming, B. Machenschalk, R. Prix, and M. Bensch, High-frequency continuous gravitational waves searched in LIGO O3 public data with Einstein@Home, arXiv e-prints , arXiv:2508.20073 (2025), arXiv:2508.20073 [gr-qc].

[41] J. Aasi *et al.* (LIGO Scientific Collaboration), Advanced LIGO, Class. Quant. Grav. **32**, 074001 (2015), arXiv:1411.4547 [gr-qc].

[42] F. Acernese *et al.* (Virgo), Advanced Virgo: a second-generation interferometric gravitational wave detector, Class. Quant. Grav. **32**, 024001 (2015), arXiv:1408.3978 [gr-qc].

[43] T. Akutsu *et al.* (KAGRA Collaboration), KAGRA: 2.5 Generation Interferometric Gravitational Wave Detector, Nature Astron. **3**, 35 (2019), arXiv:1811.08079 [gr-qc].

[44] B. P. Abbott *et al.* (LIGO, Virgo), GWTC-1: A

Gravitational-Wave Transient Catalog of Compact Binary Mergers Observed by LIGO and Virgo during the First and Second Observing Runs, Phys. Rev. X **9**, 031040 (2019), arXiv:1811.12907 [astro-ph.HE].
[45] R. Abbott *et al.* (LIGO, Virgo), GWTC-2: Compact Binary Coalescences Observed by LIGO and Virgo During the First Half of the Third Observing Run, Phys. Rev. X **11**, 021053 (2021), arXiv:2010.14527 [gr-qc].
[46] R. Abbott *et al.* (LIGO, Virgo, KAGRA), GWTC-3: Compact Binary Coalescences Observed by LIGO and Virgo during the Second Part of the Third Observing Run, Phys. Rev. X **13**, 041039 (2023), arXiv:2111.03606 [gr-qc].
[47] A. Buikema *et al.*, Sensitivity and performance of the Advanced LIGO detectors in the third observing run, Physical Review D **102**, 062003 (2020), arXiv:2008.01301 [astro-ph.IM].
[48] E. Capote *et al.*, Advanced LIGO detector performance in the fourth observing run, Phys. Rev. D **111**, 062002 (2025), arXiv:2411.14607 [gr-qc].
[49] GWTC-4.0: Updating the Gravitational-Wave Transient Catalog with Observations from the First Part of the Fourth LIGO-Virgo-KAGRA Observing Run, arXiv e-prints (2025), arXiv:2508.18082 [gr-qc].
[50] P. Jaranowski, A. Krolak, and B. F. Schutz, Data analysis of gravitational - wave signals from spinning neutron stars. 1. The Signal and its detection, Phys. Rev. D **58**, 063001 (1998), arXiv:gr-qc/9804014.
[51] C. Cutler and B. F. Schutz, The Generalized F-statistic: Multiple detectors and multiple GW pulsars, Phys. Rev. D **72**, 063006 (2005), arXiv:gr-qc/0504011.
[52] K. Wette, Lattice template placement for coherent all-sky searches for gravitational-wave pulsars, Phys. Rev. D **90**, 122010 (2014), arXiv:1410.6882 [gr-qc].
[53] P. R. Brady, T. Creighton, C. Cutler, and B. F. Schutz, Searching for periodic sources with ligo, Phys. Rev. D **57**, 2101 (1998).
[54] B. Krishnan, A. M. Sintes, M. A. Papa, B. F. Schutz, S. Frasca, and C. Palomba, The Hough transform search for continuous gravitational waves, Phys. Rev. D **70**, 082001 (2004), arXiv:gr-qc/0407001.
[55] C. Cutler, I. Gholami, and B. Krishnan, Improved stack-slide searches for gravitational-wave pulsars, Phys. Rev. D **72**, 042004 (2005).
[56] R. Prix and M. Shaltev, Search for continuous gravitational waves: Optimal stackslide method at fixed computing cost, Phys. Rev. D **85**, 084010 (2012).
[57] A. Mukherjee, C. Messenger, and K. Riles, Accretion-induced spin-wandering effects on the neutron star in scorpius x-1: Implications for continuous gravitational wave searches, Phys. Rev. D **97**, 043016 (2018).
[58] K. Rajwade, J. Chennamangalam, D. Lorimer, and A. Karastergiou, The Galactic halo pulsar population, Mon. Not. Roy. Astron. Soc. **479**, 3094 (2018), arXiv:1802.04690 [astro-ph.HE].
[59] B. T. Reed, A. Deibel, and C. J. Horowitz, Modeling the Galactic Neutron Star Population for Use in Continuous Gravitational-wave Searches, Astrophys. J. **921**, 89 (2021), arXiv:2104.00771 [astro-ph.HE].
[60] E. Goetz and K. Riles, An all-sky search algorithm for continuous gravitational waves from spinning neutron stars in binary systems, Class. Quant. Grav. **28**, 215006 (2011), arXiv:1103.1301 [gr-qc].
[61] P. B. Covas and A. M. Sintes, New method to search for continuous gravitational waves from unknown neutron stars in binary systems, Phys. Rev. D **99**, 124019 (2019), arXiv:1904.04873 [astro-ph.IM].
[62] P. B. Covas and A. M. Sintes, First all-sky search for continuous gravitational-wave signals from unknown neutron stars in binary systems using Advanced LIGO data, Phys. Rev. Lett. **124**, 191102 (2020), arXiv:2001.08411 [gr-qc].
[63] R. Abbott *et al.* (LIGO, Virgo), All-sky search in early O3 LIGO data for continuous gravitational-wave signals from unknown neutron stars in binary systems, Phys. Rev. D **103**, 064017 (2021), [Erratum: Phys.Rev.D 108, 069901 (2023)], arXiv:2012.12128 [gr-qc].
[64] P. B. Covas and R. Prix, Improved all-sky search method for continuous gravitational waves from unknown neutron stars in binary systems, Phys. Rev. D **106**, 084035 (2022), arXiv:2208.01543 [gr-qc].
[65] P. B. Covas, M. A. Papa, R. Prix, and B. J. Owen, Constraints on r-modes and Mountains on Millisecond Neutron Stars in Binary Systems, Astrophys. J. Lett. **929**, L19 (2022), arXiv:2203.01773 [gr-qc].
[66] P. B. Covas, M. A. Papa, and R. Prix, Search for Continuous Gravitational Waves from Unknown Neutron Stars in Binary Systems with Long Orbital Periods in O3 Data, Astrophys. J. **985**, 192 (2025), arXiv:2409.16196 [gr-qc].
[67] V. Dergachev and M. Alessandra Papa, First loosely coherent search for continuous gravitational wave sources with substellar companions in the Orion spur, arXiv e-prints , arXiv:2503.11503 (2025), arXiv:2503.11503 [gr-qc].
[68] P. V. C. Hough, Method and means for recognizing complex patterns (1962), filed: Nov 6, 1959; Issued: Dec 18, 1962.
[69] P. Astone, A. Colla, S. D'Antonio, S. Frasca, and C. Palomba, Method for all-sky searches of continuous gravitational wave signals using the frequency-Hough transform, Physical Review D **90**, 042002 (2014), arXiv:1407.8333 [astro-ph.IM].
[70] A. Miller, P. Astone, S. D'Antonio, S. Frasca, G. Intini, I. La Rosa, P. Leaci, S. Mastrogiovanni, F. Muciaccia, C. Palomba, O. J. Piccinni, A. Singhal, and B. F. Whiting, Method to search for long duration gravitational wave transients from isolated neutron stars using the generalized frequency-hough transform, Phys. Rev. D **98**, 102004 (2018).
[71] M. Oliver, D. Keitel, and A. M. Sintes, Adaptive transient hough method for long-duration gravitational wave transients, Phys. Rev. D **99**, 104067 (2019).
[72] R. Tenorio, J. R. Mérou, and A. M. Sintes, One-stop strategy to search for long-duration gravitational-wave signals, Phys. Rev. D **111**, 104002 (2025), arXiv:2411.18370 [gr-qc].
[73] J. Bradbury, R. Frostig, P. Hawkins, M. J. Johnson, C. Leary, D. Maclaurin, G. Necula, A. Paszke, J. VanderPlas, S. Wanderman-Milne, and Q. Zhang, JAX: composable transformations of Python+NumPy programs (2018).
[74] B. Allen *et al.*, *SFT Data Format Version 2-3 Specification*, Tech. Rep. LIGO-T040164 (LIGO Scientific Collaboration, 2022) lIGO Technical Document.
[75] J. B. Carlin and A. Melatos, How much spin wandering can continuous gravitational wave search algorithms handle?, Phys. Rev. D **111**, 083016 (2025),

arXiv:2504.08163 [gr-qc].
[76] N. Wang, R. N. Manchester, R. T. Pace, M. Bailes, V. M. Kaspi, B. W. Stappers, and A. G. Lyne, Glitches in southern pulsars, Mon. Not. Roy. Astron. Soc. **317**, 843 (2000), arXiv:astro-ph/0005561.
[77] A. Mukherjee, C. Messenger, and K. Riles, Accretion-induced spin-wandering effects on the neutron star in Scorpius X-1: Implications for continuous gravitational wave searches, Phys. Rev. D **97**, 043016 (2018), arXiv:1710.06185 [gr-qc].
[78] P. B. Covas *et al.*, Identification and mitigation of narrow spectral artifacts that degrade searches for persistent gravitational waves in the first two observing runs of Advanced LIGO, Physical Review D **97**, 082002 (2018), arXiv:1801.07204 [astro-ph.IM].
[79] A. Effler, R. M. S. Schofield, V. V. Frolov, G. González, K. Kawabe, J. R. Smith, J. Birch, and R. McCarthy, Environmental influences on the LIGO gravitational wave detectors during the 6th science run, Classical and Quantum Gravity **32**, 035017 (2015), arXiv:1409.5160 [astro-ph.IM].
[80] M. Wade, D. Bhattacharjee, L. Dartez, E. Goetz, J. Kissel, A. Viets, M. Carney, E. Makelele, J. Betzwieser, L. Sun, and L. Wade, Toward low-latency, high-fidelity calibration of the ligo detectors with enhanced monitoring tools, Classical and Quantum Gravity (2025).
[81] E. Goetz, *Segments used for creating standard SFTs in O4 data*, Tech. Rep. LIGO-T2400058-v2 (LIGO Scientific Collaboration, 2024) lIGO Technical Document.
[82] D. Davis, *Self-gating of O4a h(t) for use in continuous-wave searches*, Tech. Rep. LIGO-T2400003 (LIGO Scientific Collaboration, 2024) lIGO Technical Document.
[83] P. Astone, S. Frasca, and C. Palomba, The short FFT database and the peak map for the hierarchical search of periodic sources, Classical and Quantum Gravity **22**, S1197 (2005).
[84] LIGO Scientific Collaboration, Virgo Collaboration, and KAGRA Collaboration, LVK Algorithm Library - LALSuite, Free software (GPL) (2018).
[85] B. Allen, Performance of random template banks, Phys. Rev. D **105**, 102003 (2022), arXiv:2203.02759 [gr-qc].
[86] J. R. Mérou, R. Tenorio, and A. M. Sintes, GPU-Accelerated Searches for Long-Transient Gravitational Waves from Newborn Neutron Stars (2025) arXiv:2507.07816 [gr-qc].
[87] B. Abbott *et al.* (LIGO Scientific Collaboration), All-sky search for periodic gravitational waves in LIGO S4 data, Phys. Rev. D **77**, 022001 (2008), [Erratum: Phys.Rev.D 80, 129904 (2009)], arXiv:0708.3818 [gr-qc].
[88] C. Palomba, P. Astone, and S. Frasca, Adaptive Hough transform for the search of periodic sources, Class. Quant. Grav. **22**, S1255 (2005).
[89] R. Tenorio and J. R. Mérou, `FastTracks`, `https://github.com/Rodrigo-Tenorio/fasttracks` (2024).
[90] B. P. Abbott *et al.* (LIGO, Virgo), All-sky search for continuous gravitational waves from isolated neutron stars using Advanced LIGO O2 data, Phys. Rev. D **100**, 024004 (2019), arXiv:1903.01901 [astro-ph.HE].
[91] E. Goetz, *O4a lines and combs in found in self-gated C00 cleaned data*, Tech. Rep. LIGO-T2400204 (LIGO Scientific Collaboration, 2024) lIGO Technical Document.
[92] R. Jaume, R. Tenorio, and A. M. Sintes, Assessing the Similarity of Continuous Gravitational-Wave Signals to Narrow Instrumental Artifacts, Universe **10**, 121 (2024), arXiv:2403.03027 [gr-qc].
[93] B. P. Abbott *et al.* (LIGO, Virgo), All-sky Search for Periodic Gravitational Waves in the O1 LIGO Data, Phys. Rev. D **96**, 062002 (2017), arXiv:1707.02667 [gr-qc].
[94] B. P. Abbott *et al.* (LIGO, Virgo), Full Band All-sky Search for Periodic Gravitational Waves in the O1 LIGO Data, Phys. Rev. D **97**, 102003 (2018), arXiv:1802.05241 [gr-qc].
[95] B. Behnke, M. A. Papa, and R. Prix, Postprocessing methods used in the search for continuous gravitational-wave signals from the Galactic Center, Phys. Rev. D **91**, 064007 (2015), arXiv:1410.5997 [gr-qc].
[96] C. Dreissigacker, R. Prix, and K. Wette, Fast and Accurate Sensitivity Estimation for Continuous-Gravitational-Wave Searches, Phys. Rev. D **98**, 084058 (2018), arXiv:1808.02459 [gr-qc].
[97] G. Ashton and R. Prix, Hierarchical multistage mcmc follow-up of continuous gravitational wave candidates, Phys. Rev. D **97**, 103020 (2018).
[98] D. Keitel, R. Tenorio, G. Ashton, and R. Prix, Pyfstat: a python package for continuous gravitational-wave data analysis, Journal of Open Source Software **6**, 3000 (2021).
[99] G. Ashton, D. Keitel, R. Prix, and R. Tenorio, Pyfstat, `https://doi.org/10.5281/zenodo.8434761` (2023).
[100] K. Wette, SWIGLAL: Python and Octave interfaces to the LALSuite gravitational-wave data analysis libraries, SoftwareX **12**, 100634 (2020), arXiv:2012.09552 [astro-ph.IM].
[101] D. Foreman-Mackey, D. W. Hogg, D. Lang, and J. Goodman, emcee: The MCMC Hammer, Publications of the Astronomical Society of the Pacific **125**, 306 (2013), arXiv:1202.3665 [astro-ph.IM].
[102] W. D. Vousden, W. M. Farr, and I. Mandel, Dynamic temperature selection for parallel tempering in Markov chain Monte Carlo simulations, Monthly Notices of the Royal Astronomical Society **455**, 1919 (2016), arXiv:1501.05823 [astro-ph.IM].
[103] R. Prix, S. Giampanis, and C. Messenger, Search method for long-duration gravitational-wave transients from neutron stars, Phys. Rev. D **84**, 023007 (2011), arXiv:1104.1704 [gr-qc].
[104] G. Ashton and R. Prix, Hierarchical multistage MCMC follow-up of continuous gravitational wave candidates, Phys. Rev. D **97**, 103020 (2018), arXiv:1802.05450 [astro-ph.IM].
[105] R. Tenorio, D. Keitel, and A. M. Sintes, Application of a hierarchical MCMC follow-up to Advanced LIGO continuous gravitational-wave candidates, Phys. Rev. D **104**, 084012 (2021), arXiv:2105.13860 [gr-qc].
[106] L. Mirasola and R. Tenorio, Toward a computationally efficient follow-up pipeline for blind continuous gravitational-wave searches, Phys. Rev. D **110**, 124049 (2024).
[107] D. I. Jones and K. Riles, Multimessenger observations and the science enabled: continuous waves and their progenitors, equation of state of dense matter, Class. Quant. Grav. **42**, 033001 (2025), arXiv:2403.02066 [astro-ph.HE].
[108] M. Maggiore *et al.* (ET), Science Case for the Einstein Telescope, JCAP **03**, 050, arXiv:1912.02622 [astro-

ph.CO].

[109] M. Evans *et al.*, A Horizon Study for Cosmic Explorer: Science, Observatories, and Community, arXiv e-prints , arXiv:2109.09882 (2021), arXiv:2109.09882 [astro-ph.IM].

[110] A. Weltman *et al.*, Fundamental physics with the Square Kilometre Array, Publ. Astron. Soc. Austral. **37**, e002 (2020), arXiv:1810.02680 [astro-ph.CO].

[111] P. Virtanen *et al.*, Scipy 1.0: fundamental algorithms for scientific computing in python, Nature Methods **17**, 261 (2020).

Vetoed Frequency Ranges (Start, End) [Hz]					
(100.000, 100.026)	(100.649, 100.702)	(100.860, 100.913)	(101.302, 101.355)	(101.574, 101.699)	(101.969, 102.178)
(102.643, 102.696)	(102.963, 103.131)	(103.639, 103.693)	(104.186, 104.313)	(104.624, 104.697)	(105.294, 105.348)
(105.632, 105.687)	(106.284, 106.339)	(106.402, 106.457)	(106.629, 106.684)	(107.114, 107.170)	(107.511, 107.566)
(107.625, 107.681)	(107.945, 108.001)	(108.619, 108.678)	(109.606, 109.784)	(109.972, 110.028)	(110.615, 110.672)
(110.836, 110.893)	(111.081, 111.138)	(111.267, 111.324)	(111.611, 111.677)	(111.944, 112.002)	(112.608, 112.666)
(112.927, 112.986)	(113.052, 113.111)	(113.604, 113.796)	(114.161, 114.220)	(114.588, 114.667)	(115.269, 115.329)
(115.597, 115.657)	(116.249, 116.309)	(116.378, 116.438)	(116.594, 116.654)	(116.969, 123.091)	(123.134, 123.279)
(123.570, 123.634)	(124.136, 124.200)	(124.552, 124.638)	(125.244, 125.309)	(125.563, 125.636)	(126.213, 126.418)
(126.559, 126.625)	(127.461, 127.622)	(127.874, 127.940)	(128.552, 128.636)	(129.534, 129.624)	(129.678, 129.745)
(129.934, 130.001)	(130.545, 130.613)	(130.786, 130.854)	(130.918, 130.985)	(131.195, 131.263)	(131.542, 131.610)
(131.895, 131.963)	(132.538, 132.924)	(133.003, 133.072)	(133.297, 133.366)	(133.535, 133.604)	(134.111, 134.181)
(134.516, 134.610)	(135.220, 135.289)	(135.528, 135.598)	(136.177, 136.247)	(136.328, 136.398)	(136.525, 136.595)
(137.436, 137.592)	(137.838, 137.909)	(138.518, 138.616)	(139.498, 139.596)	(139.653, 139.725)	(140.511, 140.583)
(140.761, 140.834)	(141.159, 141.232)	(141.507, 141.580)	(141.870, 141.943)	(142.078, 142.245)	(142.504, 142.577)
(142.820, 143.052)	(143.500, 143.574)	(144.087, 144.161)	(144.405, 144.581)	(145.195, 145.270)	(146.141, 146.217)
(146.303, 146.575)	(147.412, 147.488)	(147.802, 147.878)	(148.520, 148.597)	(149.463, 149.566)	(149.628, 149.706)
(149.809, 149.886)	(150.737, 150.814)	(151.123, 151.201)	(151.550, 151.728)	(151.845, 151.923)	(152.784, 152.863)
(152.953, 153.032)	(153.475, 153.555)	(154.062, 154.141)	(154.445, 154.552)	(155.170, 155.250)	(155.513, 155.594)
(156.105, 156.186)	(156.279, 156.359)	(157.387, 157.468)	(157.766, 157.847)	(158.495, 158.577)	(159.427, 159.686)
(160.451, 160.535)	(160.712, 160.795)	(161.021, 161.211)	(161.820, 161.904)	(162.748, 162.832)	(162.929, 163.013)
(164.037, 164.122)	(164.409, 164.523)	(165.145, 165.231)	(165.757, 165.954)	(166.070, 166.155)	(166.254, 166.339)
(166.621, 166.707)	(167.362, 167.515)	(167.730, 167.817)	(168.470, 168.557)	(169.391, 169.666)	(169.984, 170.071)
(170.493, 170.775)	(171.052, 171.140)	(171.796, 171.884)	(172.712, 172.801)	(172.904, 172.993)	(174.012, 174.102)
(174.373, 174.494)	(175.121, 175.211)	(176.034, 176.125)	(176.229, 176.320)	(176.954, 183.046)	(183.988, 184.082)
(184.337, 184.465)	(185.096, 185.191)	(185.998, 186.094)	(186.204, 186.300)	(187.313, 187.409)	(187.659, 187.755)
(188.356, 188.518)	(188.838, 188.935)	(189.319, 189.660)	(190.638, 190.736)	(190.980, 191.078)	(191.746, 191.845)
(192.641, 192.740)	(192.854, 192.954)	(193.963, 194.063)	(194.302, 194.436)	(195.071, 195.172)	(195.332, 195.434)
(195.962, 196.063)	(196.179, 196.280)	(197.288, 197.389)	(197.623, 197.725)	(198.396, 198.498)	(198.909, 199.143)
(199.284, 199.421)	(199.505, 199.607)	(199.945, 200.049)	(200.613, 200.716)	(200.944, 201.048)	(201.721, 201.825)
(202.605, 202.709)	(202.830, 202.934)	(203.938, 204.043)	(204.266, 204.407)	(205.046, 205.152)	(205.926, 206.032)
(206.155, 206.261)	(207.263, 207.370)	(207.587, 207.694)	(208.371, 208.626)	(209.248, 209.588)	(209.733, 209.841)
(210.588, 210.697)	(210.909, 211.017)	(211.697, 211.805)	(212.569, 212.679)	(212.805, 212.914)	(213.913, 214.023)
(214.230, 214.378)	(215.022, 215.132)	(215.891, 216.002)	(216.130, 216.241)	(217.238, 217.350)	(217.551, 217.663)
(217.853, 218.109)	(218.347, 218.459)	(219.212, 219.363)	(219.455, 219.568)	(220.563, 220.677)	(220.873, 220.986)
(221.672, 221.786)	(222.533, 222.648)	(222.780, 222.895)	(223.889, 224.004)	(224.194, 224.349)	(224.997, 225.113)
(225.855, 225.971)	(226.105, 226.222)	(227.214, 227.633)	(228.322, 228.439)	(229.176, 229.335)	(229.430, 229.548)
(229.907, 230.025)	(230.539, 230.657)	(230.837, 230.956)	(231.647, 231.766)	(232.498, 232.617)	(232.755, 232.875)
(233.864, 233.984)	(234.158, 234.320)	(234.972, 235.093)	(235.819, 235.940)	(236.080, 236.202)	(236.796, 243.061)
(243.839, 243.964)	(244.123, 244.291)	(244.947, 245.073)	(245.783, 245.910)	(246.056, 246.182)	(246.268, 246.559)
(247.164, 247.291)	(247.444, 247.571)	(248.272, 248.400)	(249.105, 249.277)	(249.381, 249.509)	(250.489, 250.618)
(250.765, 250.894)	(251.598, 251.727)	(252.426, 252.556)	(252.706, 252.836)	(253.814, 253.945)	(254.087, 254.262)
(254.923, 255.054)	(255.740, 256.163)	(257.139, 257.272)	(257.408, 257.540)	(258.248, 258.380)	(259.069, 259.248)
(259.356, 259.489)	(260.464, 260.598)	(260.729, 260.864)	(261.573, 261.707)	(262.390, 262.525)	(262.681, 262.816)
(263.789, 263.925)	(264.051, 264.233)	(264.898, 265.034)	(265.212, 265.525)	(265.712, 265.848)	(266.006, 266.143)
(267.115, 267.510)	(268.223, 268.361)	(269.033, 269.219)	(269.331, 269.470)	(269.656, 269.795)	(269.956, 270.095)
(270.440, 270.579)	(270.694, 270.833)	(271.548, 271.688)	(272.354, 272.494)	(272.656, 272.797)	(273.765, 273.905)
(274.015, 274.204)	(274.684, 275.014)	(275.676, 275.817)	(275.981, 276.123)	(277.090, 277.232)	(277.336, 277.479)
(278.198, 278.341)	(278.997, 279.190)	(279.307, 279.450)	(280.415, 280.559)	(280.658, 280.802)	(281.523, 281.668)
(282.319, 282.464)	(282.632, 282.777)	(283.208, 283.513)	(283.740, 284.491)	(284.848, 284.995)	(285.640, 285.787)
(285.957, 286.104)	(287.065, 287.213)	(287.301, 287.448)	(288.173, 288.321)	(288.961, 289.161)	(289.282, 289.430)
(290.390, 290.771)	(291.498, 291.648)	(292.283, 292.433)	(292.607, 292.757)	(293.627, 294.146)	(294.824, 294.975)
(295.604, 295.756)	(295.932, 296.084)	(296.923, 303.522)	(303.690, 303.846)	(303.908, 304.117)	(304.799, 304.955)
(305.568, 305.725)	(305.852, 306.568)	(307.016, 307.690)	(308.124, 308.282)	(308.890, 309.103)	(309.232, 309.391)
(310.341, 310.710)	(311.449, 311.609)	(312.211, 312.372)	(312.557, 312.940)	(313.666, 314.088)	(314.637, 315.474)
(315.533, 315.695)	(315.882, 316.045)	(316.991, 317.356)	(318.099, 318.263)	(318.854, 319.074)	(319.207, 319.371)
(320.316, 320.480)	(320.515, 320.679)	(321.424, 321.589)	(322.043, 322.423)	(322.533, 322.698)	(323.641, 324.060)
(324.749, 324.916)	(325.497, 325.664)	(325.858, 326.025)	(326.966, 327.326)	(328.074, 328.243)	(328.818, 329.045)
(329.183, 329.352)	(329.580, 329.750)	(329.880, 330.049)	(330.291, 330.649)	(331.399, 331.907)	(332.140, 332.310)
(332.508, 332.679)	(333.616, 334.031)	(334.725, 334.896)	(335.461, 335.633)	(335.833, 336.005)	(336.941, 337.295)
(338.050, 338.223)	(338.782, 339.016)	(339.158, 339.332)			

TABLE VI. Vetoed frequency ranges due to known instrumental artifacts.

All-sky search for continuous gravitational-wave signals from unknown neutron stars in binary systems in the first part of the fourth LIGO-Virgo-KAGRA observing run

A. G. Abac,[1] I. Abouelfettouh,[2] F. Acernese,[3,4] K. Ackley,[5] C. Adamcewicz,[6] S. Adhicary,[7] D. Adhikari,[8,9] N. Adhikari,[10] R. X. Adhikari,[11] V. K. Adkins,[12] S. Afroz,[13] A. Agapito,[14] D. Agarwal,[15] M. Agathos,[16] N. Aggarwal,[17] S. Aggarwal,[18] O. D. Aguiar,[19] I.-L. Ahrend,[20] L. Aiello,[21,22] A. Ain,[23] P. Ajith,[24] T. Akutsu,[25,26] S. Albanesi,[27,28] W. Ali,[29,30] S. Al-Kershi,[8,9] C. Alléné,[31] A. Allocca,[32,4] S. Al-Shammari,[33] P. A. Altin,[34] S. Alvarez-Lopez,[35] W. Amar,[31] O. Amarasinghe,[33] A. Amato,[36,37] F. Amicucci,[38,39] C. Amra,[40] A. Ananyeva,[11] S. B. Anderson,[11] W. G. Anderson,[11] M. Andia,[41] M. Ando,[42] M. Andrés-Carcasona,[43] T. Andrić,[44,45,8,9] J. Anglin,[46] S. Ansoldi,[47,48] J. M. Antelis,[49] S. Antier,[41] M. Aoumi,[50] E. Z. Appavuravther,[51,52] S. Appert,[11] S. K. Apple,[53] K. Arai,[11] A. Araya,[42] M. C. Araya,[11] M. Arca Sedda,[44,45] J. S. Areeda,[54] N. Aritomi,[2] F. Armato,[29,30] S. Armstrong,[55] N. Arnaud,[56] M. Arogeti,[57] S. M. Aronson,[12] G. Ashton,[58] Y. Aso,[25,59] L. Asprea,[28] M. Assiduo,[60,61] S. Assis de Souza Melo,[62] S. M. Aston,[63] P. Astone,[38] F. Attadio,[39,38] F. Aubin,[64] K. AultONeal,[65] G. Avallone,[66] E. A. Avila,[49] S. Babak,[20] C. Badger,[67] S. Bae,[68] S. Bagnasco,[28] L. Baiotti,[69] R. Bajpai,[70] T. Baka,[71,37] A. M. Baker,[6] K. A. Baker,[72] T. Baker,[73] G. Baldi,[74,75] N. Baldicchi,[76,51] M. Ball,[77] G. Ballardin,[62] S. W. Ballmer,[78] S. Banagiri,[6] B. Banerjee,[44] D. Bankar,[79] T. M. Baptiste,[12] P. Baral,[10] M. Baratti,[80,81] J. C. Barayoga,[11] B. C. Barish,[11] D. Barker,[2] N. Barman,[79] P. Barneo,[82,83,84] F. Barone,[85,4] B. Barr,[86] L. Barsotti,[35] M. Barsuglia,[20] D. Barta,[87] A. M. Bartoletti,[88] M. A. Barton,[86] I. Bartos,[46] A. Basalaev,[8,9] R. Bassiri,[89] A. Basti,[81,80] M. Bawaj,[76,51] P. Baxi,[90] J. C. Bayley,[86] A. C. Baylor,[10] P. A. Baynard II,[57] M. Bazzan,[91,92] V. M. Bedakihale,[93] F. Beirnaert,[94] M. Bejger,[95] D. Belardinelli,[22] A. S. Bell,[86] D. S. Bellie,[96] L. Bellizzi,[80,81] W. Benoit,[18] I. Bentara,[56] J. D. Bentley,[97] M. Ben Yaala,[55] S. Bera,[98,99] F. Bergamin,[33] B. K. Berger,[89] S. Bernuzzi,[27] M. Beroiz,[11] D. Bersanetti,[29] T. Bertheas,[100] A. Bertolini,[37,36] J. Betzwieser,[63] D. Beveridge,[72] G. Bevilacqua,[101] N. Bevins,[102] R. Bhandare,[103] R. Bhatt,[11] D. Bhattacharjee,[104,105] S. Bhattacharyya,[106] S. Bhaumik,[46] V. Biancalana,[101] A. Bianchi,[37,107] I. A. Bilenko,[108] G. Billingsley,[11] A. Binetti,[109] S. Bini,[11,74,75] C. Binu,[110] S. Biot,[111] O. Birnholtz,[112] S. Biscoveanu,[96] A. Bisht,[9] M. Bitossi,[62,80] M.-A. Bizouard,[113] S. Blaber,[114] J. K. Blackburn,[11] L. A. Blagg,[77] C. D. Blair,[72,63] D. G. Blair,[72] N. Bode,[8,9] N. Boettner,[97] G. Boileau,[113] M. Boldrini,[38] G. N. Bolingbroke,[115] A. Bolliand,[116,40] L. D. Bonavena,[46] R. Bondarescu,[82] F. Bondu,[117] E. Bonilla,[89] M. S. Bonilla,[54] A. Bonino,[118] R. Bonnand,[31,116] A. Borchers,[8,9] V. Boschi,[80] S. Bose,[119] V. Bossilkov,[63] Y. Bothra,[37,107] A. Boudon,[56] L. Bourg,[57] M. Boyle,[120] A. Bozzi,[62] C. Bradaschia,[80] P. R. Brady,[10] A. Branch,[63] M. Branchesi,[44,45] I. Braun,[104] T. Briant,[121] A. Brillet,[113] M. Brinkmann,[8,9] P. Brockill,[10] E. Brockmueller,[8,9] A. F. Brooks,[11] B. C. Brown,[46] D. D. Brown,[115] M. L. Brozzetti,[76,51] S. Brunett,[11] G. Bruno,[15] R. Bruntz,[122] J. Bryant,[118] Y. Bu,[123] F. Bucci,[61] J. Buchanan,[122] O. Bulashenko,[82,83] T. Bulik,[124] H. J. Bulten,[37] A. Buonanno,[125,1] K. Burtnyk,[2] R. Buscicchio,[126,127] D. Buskulic,[31] C. Buy,[100] R. L. Byer,[89] G. S. Cabourn Davies,[73] R. Cabrita,[15] V. Cáceres-Barbosa,[7] L. Cadonati,[57] G. Cagnoli,[128] C. Cahillane,[78] A. Calafat,[98] T. A. Callister,[129] E. Calloni,[32,4] S. R. Callos,[77] M. Canepa,[30,29] G. Caneva Santoro,[43] K. C. Cannon,[42] H. Cao,[35] L. A. Capistran,[130] E. Capocasa,[20] E. Capote,[2,11] G. Capurri,[81,80] G. Carapella,[66,131] F. Carbognani,[62] M. Carlassara,[8,9] J. B. Carlin,[123] T. K. Carlson,[132] M. F. Carney,[104] M. Carpinelli,[126,62] G. Carrillo,[77] J. J. Carter,[8,9] G. Carullo,[118,133] A. Casallas-Lagos,[134] J. Casanueva Diaz,[62] C. Casentini,[135,22] S. Y. Castro-Lucas,[136] S. Caudill,[132] M. Cavaglià,[105] R. Cavalieri,[62] A. Ceja,[54] G. Cella,[80] P. Cerdá-Durán,[137,138] E. Cesarini,[22] N. Chabbra,[34] W. Chaibi,[113] A. Chakraborty,[13] P. Chakraborty,[8,9] S. Chakraborty,[103] S. Chalathadka Subrahmanya,[97] J. C. L. Chan,[139] M. Chan,[114] K. Chang,[140] S. Chao,[141,140] P. Charlton,[142] E. Chassande-Mottin,[20] C. Chatterjee,[143] Debarati Chatterjee,[79] Deep Chatterjee,[35] M. Chaturvedi,[103] S. Chaty,[20] A. Chen,[144] A. H.-Y. Chen,[145] D. Chen,[146] H. Chen,[141] H. Y. Chen,[147] S. Chen,[143] Yanbei Chen,[148] Yitian Chen,[120] H. P. Cheng,[149] P. Chessa,[76,51] H. T. Cheung,[90] S. Y. Cheung,[6] F. Chiadini,[150,131] G. Chiarini,[8,9,92] A. Chiba,[151] A. Chincarini,[29] M. L. Chiofalo,[81,80] A. Chiummo,[4,62] C. Chou,[145] S. Choudhary,[72] N. Christensen,[113,152] S. S. Y. Chua,[34] G. Ciani,[74,75] P. Ciecielag,[95] M. Cieślar,[124] M. Cifaldi,[22] B. Cirok,[153] F. Clara,[2] J. A. Clark,[11,57] T. A. Clarke,[6] P. Clearwater,[154] S. Clesse,[111] F. Cleva,[113,116] E. Coccia,[44,45,43] E. Codazzo,[155,156] P.-F. Cohadon,[121] S. Colace,[30] E. Colangeli,[73] M. Colleoni,[98] C. G. Collette,[157] J. Collins,[63] S. Colloms,[86] A. Colombo,[158,127] C. M. Compton,[2] G. Connolly,[77] L. Conti,[92] T. R. Corbitt,[12] I. Cordero-Carrión,[159] S. Corezzi,[76,51] N. J. Cornish,[160] I. Coronado,[161]

A. Corsi ,[162] R. Cottingham,[63] M. W. Coughlin ,[18] A. Couineaux,[38] P. Couvares ,[11,57] D. M. Coward,[72] R. Coyne ,[163] A. Cozzumbo,[44] J. D. E. Creighton ,[10] T. D. Creighton,[164] P. Cremonese ,[98] S. Crook,[63] R. Crouch,[2] J. Csizmazia,[2] J. R. Cudell ,[165] T. J. Cullen ,[11] A. Cumming ,[86] E. Cuoco ,[166,167] M. Cusinato ,[137] L. V. Da Conceição ,[168] T. Dal Canton ,[41] S. Dal Pra ,[169] S. Dall'Osso ,[170,171] G. Dálya ,[100] B. D'Angelo ,[29] S. Danilishin ,[36,37] S. D'Antonio ,[38] K. Danzmann,[9,8,9] K. E. Darroch,[122] L. P. Dartez ,[63] R. Das,[106] A. Dasgupta,[93] V. Dattilo ,[62] A. Daumas,[20] N. Davari,[172,173] I. Dave,[103] A. Davenport,[136] M. Davier,[41] T. F. Davies,[72] D. Davis ,[11] L. Davis,[72] M. C. Davis ,[18] P. Davis ,[174,175] E. J. Daw ,[176] M. Dax ,[1] J. De Bolle ,[94] M. Deenadayalan,[79] J. Degallaix ,[177] M. De Laurentis ,[32,4] F. De Lillo ,[23] S. Della Torre ,[127] W. Del Pozzo ,[81,80] A. Demagny,[31] F. De Marco ,[39,38] G. Demasi,[178,61] F. De Matteis ,[21,22] N. Demos,[35] T. Dent ,[179] A. Depasse ,[15] N. DePergola,[102] R. De Pietri ,[180,181] R. De Rosa ,[32,4] C. De Rossi ,[62] M. Desai ,[35] R. DeSalvo ,[182] A. DeSimone,[183] R. De Simone,[150,131] A. Dhani ,[1] R. Diab,[46] M. C. Díaz ,[164] M. Di Cesare ,[32,4] G. Dideron,[184] T. Dietrich ,[1] L. Di Fiore,[4] C. Di Fronzo ,[72] M. Di Giovanni ,[39,38] T. Di Girolamo ,[32,4] D. Diksha,[37,36] J. Ding ,[20,185] S. Di Pace ,[39,38] I. Di Palma ,[39,38] D. Di Piero,[186,48] F. Di Renzo ,[56] Divyajyoti ,[33] A. Dmitriev ,[118] J. P. Docherty,[86] Z. Doctor ,[96] N. Doerksen ,[168] E. Dohmen,[2] A. Doke,[132] A. Domiciano De Souza,[187] L. D'Onofrio ,[38] F. Donovan,[35] K. L. Dooley ,[33] T. Dooney,[71] S. Doravari ,[79] O. Dorosh,[188] W. J. D. Doyle,[122] M. Drago ,[39,38] J. C. Driggers ,[2] L. Dunn ,[123] U. Dupletsa,[44] P.-A. Duverne ,[20] D. D'Urso ,[172,155] P. Dutta Roy ,[46] H. Duval ,[189] S. E. Dwyer,[2] C. Eassa,[2] M. Ebersold ,[190,31] T. Eckhardt ,[97] G. Eddolls ,[78] A. Effler ,[63] J. Eichholz ,[34] H. Einsle,[113] M. Eisenmann,[25] M. Emma ,[58] K. Endo,[151] R. Enficiaud ,[1] L. Errico ,[32,4] R. Espinosa,[164] M. Esposito ,[4,32] R. C. Essick ,[191] H. Estellés ,[1] T. Etzel,[11] M. Evans ,[35] T. Evstafyeva,[184] B. E. Ewing,[7] J. M. Ezquiaga ,[139] F. Fabrizi ,[60,61] V. Fafone ,[21,22] S. Fairhurst ,[33] A. M. Farah ,[129] B. Farr ,[77] W. M. Farr ,[192,193] G. Favaro ,[91] M. Favata ,[194] M. Fays ,[165] M. Fazio ,[55] J. Feicht,[11] M. M. Fejer,[89] R. Felicetti ,[186,48] E. Fenyvesi ,[87,195] J. Fernandes,[196] T. Fernandes ,[197,137] D. Fernando,[110] S. Ferraiuolo ,[198,39,38] T. A. Ferreira,[12] F. Fidecaro ,[81,80] P. Figura ,[95] A. Fiori ,[80,81] I. Fiori ,[62] M. Fishbach ,[191] R. P. Fisher,[122] R. Fittipaldi ,[199,131] V. Fiumara ,[200,131] R. Flaminio,[31] S. M. Fleischer ,[201] L. S. Fleming,[202] E. Floden,[18] H. Fong,[114] J. A. Font ,[137,138] F. Fontinele-Nunes,[18] C. Foo,[1] B. Fornal ,[203] K. Franceschetti,[180] F. Frappez,[31] S. Frasca,[39,38] F. Frasconi ,[80] J. P. Freed,[65] Z. Frei ,[204] A. Freise ,[37,107] O. Freitas ,[197,137] R. Frey ,[77] W. Frischhertz,[63] P. Fritschel,[35] V. V. Frolov,[63] G. G. Fronzé ,[28] M. Fuentes-Garcia ,[11] S. Fujii,[205] T. Fujimori,[206] P. Fulda,[46] M. Fyffe,[63] B. Gadre ,[71] J. R. Gair ,[1] S. Galaudage ,[187] V. Galdi,[207] R. Gamba,[7] A. Gamboa ,[1] S. Gamoji,[182] D. Ganapathy ,[208] A. Ganguly ,[79] B. Garaventa ,[29] J. García-Bellido ,[209] C. García-Quirós ,[190] J. W. Gardner ,[34] K. A. Gardner,[114] S. Garg,[42] J. Gargiulo ,[62] X. Garrido ,[41] A. Garron ,[98] F. Garufi ,[32,4] P. A. Garver,[89] C. Gasbarra ,[21,22] B. Gateley,[2] F. Gautier ,[210] V. Gayathri ,[10] T. Gayer,[78] G. Gemme ,[29] A. Gennai ,[80] V. Gennari ,[100] J. George,[103] R. George ,[147] O. Gerberding ,[97] L. Gergely ,[153] Archisman Ghosh ,[94] Sayantan Ghosh,[196] Shaon Ghosh ,[194] Shrobana Ghosh,[8,9] Suprovo Ghosh ,[211] Tathagata Ghosh ,[79] J. A. Giaime ,[12,63] K. D. Giardina,[63] D. R. Gibson,[202] C. Gier ,[55] S. Gkaitatzis ,[81,80] J. Glanzer ,[11] F. Glotin ,[41] J. Godfrey,[77] R. V. Godley,[8,9] P. Godwin ,[11] A. S. Goettel ,[33] E. Goetz ,[114] J. Golomb,[11] S. Gomez Lopez ,[39,38] B. Goncharov ,[44] G. González ,[12] P. Goodarzi ,[212] S. Goode,[6] A. W. Goodwin-Jones ,[15] M. Gosselin,[62] R. Gouaty ,[31] D. W. Gould,[34] K. Govorkova,[35] A. Grado ,[76,51] V. Graham ,[86] A. E. Granados ,[18] M. Granata ,[177] V. Granata ,[213,131] S. Gras,[35] P. Grassia,[11] J. Graves,[57] C. Gray,[2] R. Gray ,[86] G. Greco,[51] A. C. Green ,[37,107] L. Green,[214] S. M. Green,[73] S. R. Green ,[215] C. Greenberg,[132] A. M. Gretarsson,[65] H. K. Griffin,[18] D. Griffith,[11] H. L. Griggs ,[57] G. Grignani,[76,51] C. Grimaud ,[31] H. Grote ,[33] S. Grunewald ,[1] D. Guerra ,[137] D. Guetta ,[216] G. M. Guidi ,[60,61] A. R. Guimaraes,[12] H. K. Gulati,[93] F. Gulminelli ,[174,175] H. Guo ,[144] W. Guo ,[72] Y. Guo ,[37,36] Anuradha Gupta ,[217] I. Gupta ,[7] N. C. Gupta,[93] S. K. Gupta,[46] V. Gupta ,[18] N. Gupte,[1] J. Gurs,[97] N. Gutierrez,[177] N. Guttman,[6] F. Guzman ,[130] D. Haba,[218] M. Haberland ,[1] S. Haino,[219] E. D. Hall ,[35] E. Z. Hamilton ,[98] G. Hammond ,[86] M. Haney,[37] J. Hanks,[2] C. Hanna ,[7] M. D. Hannam,[33] O. A. Hannuksela ,[220] A. G. Hanselman ,[129] H. Hansen,[2] J. Hanson,[63] S. Hanumasagar,[57] R. Harada,[42] A. R. Hardison,[183] S. Harikumar ,[188] K. Haris,[37,71] I. Harley-Trochimczyk,[130] T. Harmark ,[133] J. Harms ,[44,45] G. M. Harry ,[221] I. W. Harry ,[73] J. Hart,[104] B. Haskell,[95,222,223] C. J. Haster ,[214] K. Haughian ,[86] H. Hayakawa,[50] K. Hayama,[224] M. C. Heintze,[63] J. Heinze ,[118] J. Heinzel,[35] H. Heitmann ,[113] F. Hellman ,[208] A. F. Helmling-Cornell ,[77] G. Hemming ,[62] O. Henderson-Sapir ,[115] M. Hendry ,[86] I. S. Heng,[86] M. H. Hennig ,[86] C. Henshaw ,[57] M. Heurs ,[8,9] A. L. Hewitt ,[225,226] J. Heynen,[15] J. Heyns,[35] S. Higginbotham,[33] S. Hild,[36,37] S. Hill,[86] Y. Himemoto ,[227] N. Hirata,[25] C. Hirose,[228]

D. Hofman,[177] B. E. Hogan,[65] N. A. Holland,[37,107] I. J. Hollows,[176] D. E. Holz,[129] L. Honet,[111] D. J. Horton-Bailey,[208] J. Hough,[86] S. Hourihane,[11] N. T. Howard,[143] E. J. Howell,[72] C. G. Hoy,[73] C. A. Hrishikesh,[21] P. Hsi,[35] H.-F. Hsieh,[141] H.-Y. Hsieh,[141] C. Hsiung,[229] S.-H. Hsu,[145] W.-F. Hsu,[109] Q. Hu,[86] H. Y. Huang,[140] Y. Huang,[7] Y. T. Huang,[78] A. D. Huddart,[230] B. Hughey,[65] V. Hui,[31] S. Husa,[98] R. Huxford,[7] L. Iampieri,[39,38] G. A. Iandolo,[36] M. Ianni,[22,21] G. Iannone,[131] J. Iascau,[77] K. Ide,[231] R. Iden,[218] A. Ierardi,[44,45] S. Ikeda,[146] H. Imafuku,[42] Y. Inoue,[140] G. Iorio,[91] P. Iosif,[186,48] M. H. Iqbal,[34] J. Irwin,[86] R. Ishikawa,[231] M. Isi,[192,193] K. S. Isleif,[232] Y. Itoh,[206,233] M. Iwaya,[205] B. R. Iyer,[24] C. Jacquet,[100] P.-E. Jacquet,[121] T. Jacquot,[41] S. J. Jadhav,[234] S. P. Jadhav,[154] M. Jain,[132] T. Jain,[225] A. L. James,[11] K. Jani,[143] J. Janquart,[15] N. N. Janthalur,[234] S. Jaraba,[235] P. Jaranowski,[236] R. Jaume,[98] W. Javed,[33] A. Jennings,[2] M. Jensen,[2] W. Jia,[35] J. Jiang,[149] H.-B. Jin,[237,238] G. R. Johns,[122] N. A. Johnson,[46] M. C. Johnston,[214] R. Johnston,[86] N. Johny,[8,9] D. H. Jones,[34] D. I. Jones,[211] R. Jones,[86] H. E. Jose,[77] P. Joshi,[7] S. K. Joshi,[79] G. Joubert,[56] J. Ju,[239] L. Ju,[72] K. Jung,[240] J. Junker,[34] V. Juste,[111] H. B. Kabagoz,[63,35] T. Kajita,[241] I. Kaku,[206] V. Kalogera,[96] M. Kalomenopoulos,[214] M. Kamiizumi,[50] N. Kanda,[233,206] S. Kandhasamy,[79] G. Kang,[242] N. C. Kannachel,[6] J. B. Kanner,[11] S. A. KantiMahanty,[18] S. J. Kapadia,[79] D. P. Kapasi,[54] M. Karthikeyan,[132] M. Kasprzack,[11] H. Kato,[151] T. Kato,[205] E. Katsavounidis,[35] W. Katzman,[63] R. Kaushik,[103] K. Kawabe,[2] R. Kawamoto,[206] D. Keitel,[98] L. J. Kemperman,[115] J. Kennington,[7] F. A. Kerkow,[18] R. Kesharwani,[79] J. S. Key,[243] R. Khadela,[8,9] S. Khadka,[89] S. S. Khadkikar,[7] F. Y. Khalili,[108] F. Khan,[8,9] T. Khanam,[162] M. Khursheed,[103] N. M. Khusid,[192,193] W. Kiendrebeogo,[113,244] N. Kijbunchoo,[115] C. Kim,[245] J. C. Kim,[246] K. Kim,[247] M. H. Kim,[239] S. Kim,[248] Y.-M. Kim,[247] C. Kimball,[96] K. Kimes,[54] M. Kinnear,[33] J. S. Kissel,[2] S. Klimenko,[46] A. M. Knee,[114] E. J. Knox,[77] N. Knust,[8,9] K. Kobayashi,[205] S. M. Koehlenbeck,[89] G. Koekoek,[37,36] K. Kohri,[249,250] K. Kokeyama,[33,251] S. Koley,[44,165] P. Kolitsidou,[118] A. E. Koloniari,[252] K. Komori,[42] A. K. H. Kong,[141] A. Kontos,[253] L. M. Koponen,[118] M. Korobko,[97] X. Kou,[18] A. Koushik,[23] N. Kouvatsos,[67] M. Kovalam,[72] T. Koyama,[151] D. B. Kozak,[11] S. L. Kranzhoff,[36,37] V. Kringel,[8,9] N. V. Krishnendu,[118] S. Kroker,[254] A. Królak,[255,188] K. Kruska,[8,9] J. Kubisz,[256] G. Kuehn,[8,9] S. Kulkarni,[217] A. Kulur Ramamohan,[34] Achal Kumar,[46] Anil Kumar,[234] Praveen Kumar,[179] Prayush Kumar,[24] Rahul Kumar,[2] Rakesh Kumar,[93] J. Kume,[257,258,42] K. Kuns,[35] N. Kuntimaddi,[33] S. Kuroyanagi,[209,259] S. Kuwahara,[42] K. Kwak,[240] K. Kwan,[34] S. Kwon,[42] G. Lacaille,[86] D. Laghi,[190,100] A. H. Laity,[163] E. Lalande,[260] M. Lalleman,[23] P. C. Lalremruati,[261] M. Landry,[2] B. B. Lane,[35] R. N. Lang,[35] J. Lange,[147] R. Langgin,[214] B. Lantz,[89] I. La Rosa,[98] J. Larsen,[201] A. Lartaux-Vollard,[41] P. D. Lasky,[6] J. Lawrence,[164] M. Laxen,[63] C. Lazarte,[137] A. Lazzarini,[11] C. Lazzaro,[156,155] P. Leaci,[39,38] L. Leali,[18] Y. K. Lecoeuche,[114] H. M. Lee,[262] H. W. Lee,[263] J. Lee,[78] K. Lee,[239] R.-K. Lee,[141] R. Lee,[35] Sungho Lee,[247] Sunjae Lee,[239] Y. Lee,[140] I. N. Legred,[11] J. Lehmann,[8,9] L. Lehner,[184] M. Le Jean,[177,116] A. Lemaître,[264] M. Lenti,[61,178] M. Leonardi,[74,75,265] M. Lequime,[40] N. Leroy,[41] M. Lesovsky,[11] N. Letendre,[31] M. Lethuillier,[56] Y. Levin,[6] K. Leyde,[73] A. K. Y. Li,[11] K. L. Li,[266] T. G. F. Li,[109] X. Li,[148] Y. Li,[96] Z. Li,[86] A. Lihos,[122] E. T. Lin,[141] F. Lin,[140] L. C.-C. Lin,[266] Y.-C. Lin,[141] C. Lindsay,[202] S. D. Linker,[182] A. Liu,[220] G. C. Liu,[229] Jian Liu,[72] F. Llamas Villarreal,[164] J. Llobera-Querol,[98] R. K. L. Lo,[139] J.-P. Locquet,[109] S. C. G. Loggins,[267] M. R. Loizou,[132] L. T. London,[67] A. Longo,[60,61] D. Lopez,[165] M. Lopez Portilla,[71] M. Lorenzini,[21,22] A. Lorenzo-Medina,[179] V. Loriette,[41] M. Lormand,[63] G. Losurdo,[268,80] E. Lotti,[132] T. P. Lott IV,[57] J. D. Lough,[8,9] H. A. Loughlin,[35] C. O. Lousto,[110] N. Low,[123] N. Lu,[34] L. Lucchesi,[80] H. Lück,[9,8,9] D. Lumaca,[22] A. P. Lundgren,[269,270] A. W. Lussier,[260] R. Macas,[73] M. MacInnis,[35] D. M. Macleod,[33] I. A. O. MacMillan,[11] A. Macquet,[41] K. Maeda,[151] S. Maenaut,[109] S. S. Magare,[79] R. M. Magee,[11] E. Maggio,[1] R. Maggiore,[37,107] M. Magnozzi,[29,30] M. Mahesh,[97] M. Maini,[163] S. Majhi,[79] E. Majorana,[39,38] C. N. Makarem,[11] D. Malakar,[105] J. A. Malaquias-Reis,[19] U. Mali,[191] S. Maliakal,[11] A. Malik,[103] L. Mallick,[168,191] A.-K. Malz,[58] N. Man,[113] M. Mancarella,[99] V. Mandic,[18] V. Mangano,[172,155] B. Mannix,[77] G. L. Mansell,[78] M. Manske,[10] M. Mantovani,[62] M. Mapelli,[91,92,271] C. Marinelli,[101] F. Marion,[31] A. S. Markosyan,[89] A. Markowitz,[11] E. Maros,[11] S. Marsat,[100] F. Martelli,[60,61] I. W. Martin,[86] R. M. Martin,[194] B. B. Martinez,[130] D. A. Martinez,[54] M. Martinez,[43,272] V. Martinez,[128] A. Martini,[74,75] J. C. Martins,[19] D. V. Martynov,[118] E. J. Marx,[35] L. Massaro,[36,37] A. Masserot,[31] M. Masso-Reid,[86] S. Mastrogiovanni,[38] T. Matcovich,[51] M. Matiushechkina,[8,9] L. Maurin,[210] N. Mavalvala,[35] N. Maxwell,[2] G. McCarrol,[63] R. McCarthy,[2] D. E. McClelland,[34] S. McCormick,[63] L. McCuller,[11] S. McEachin,[122] C. McElhenny,[122] G. I. McGhee,[86] J. McGinn,[86] K. B. M. McGowan,[143] J. McIver,[114] A. McLeod,[72] I. McMahon,[190] T. McRae,[34] R. McTeague,[86] D. Meacher,[10] B. N. Meagher,[78]

R. Mechum,[110] Q. Meijer,[71] A. Melatos,[123] C. S. Menoni,[136] F. Mera,[2] R. A. Mercer,[10] L. Mereni,[177] K. Merfeld,[162] E. L. Merilh,[63] J. R. Mérou,[98] J. D. Merritt,[77] M. Merzougui,[113] C. Messick,[10] B. Mestichelli,[44] M. Meyer-Conde,[273] F. Meylahn,[8, 9] A. Mhaske,[79] A. Miani,[74, 75] H. Miao,[274] C. Michel,[177] Y. Michimura,[42] H. Middleton,[118] D. P. Mihaylov,[104] A. L. Miller,[37, 71] S. J. Miller,[11] M. Millhouse,[57] E. Milotti,[186, 48] V. Milotti,[91] Y. Minenkov,[22] E. M. Minihan,[65] Ll. M. Mir,[43] L. Mirasola,[155, 156] M. Miravet-Tenés,[137] C.-A. Miritescu,[43] A. Mishra,[24] C. Mishra,[106] T. Mishra,[46] A. L. Mitchell,[37, 107] J. G. Mitchell,[65] S. Mitra,[79] V. P. Mitrofanov,[108] K. Mitsuhashi,[25] R. Mittleman,[35] O. Miyakawa,[50] S. Miyoki,[50] A. Miyoko,[65] G. Mo,[35] L. Mobilia,[60, 61] S. R. P. Mohapatra,[11] S. R. Mohite,[7] M. Molina-Ruiz,[208] M. Mondin,[182] M. Montani,[60, 61] C. J. Moore,[225] D. Moraru,[2] A. More,[79] S. More,[79] C. Moreno,[134] E. A. Moreno,[35] G. Moreno,[2] A. Moreso Serra,[82] S. Morisaki,[42, 205] Y. Moriwaki,[151] G. Morras,[209] A. Moscatello,[91] M. Mould,[35] B. Mours,[64] C. M. Mow-Lowry,[37, 107] L. Muccillo,[178, 61] F. Muciaccia,[39, 38] D. Mukherjee,[118] Samanwaya Mukherjee,[24] Soma Mukherjee,[164] Subroto Mukherjee,[93] Suvodip Mukherjee,[13] N. Mukund,[35] A. Mullavey,[63] H. Mullock,[114] J. Mundi,[221] C. L. Mungioli,[72] M. Murakoshi,[231] P. G. Murray,[86] D. Nabari,[74, 75] S. L. Nadji,[8, 9] A. Nagar,[28, 275] N. Nagarajan,[86] K. Nakagaki,[50] K. Nakamura,[25] H. Nakano,[276] M. Nakano,[11] D. Nanadoumgar-Lacroze,[43] D. Nandi,[12] V. Napolano,[62] P. Narayan,[217] I. Nardecchia,[22] T. Narikawa,[205] H. Narola,[71] L. Naticchioni,[38] R. K. Nayak,[261] L. Negri,[71] A. Nela,[86] C. Nelle,[77] A. Nelson,[130] T. J. N. Nelson,[63] M. Nery,[8, 9] A. Neunzert,[2] S. Ng,[54] L. Nguyen Quynh,[277] S. A. Nichols,[12] A. B. Nielsen,[278] Y. Nishino,[25, 42] A. Nishizawa,[279] S. Nissanke,[280, 37] W. Niu,[7] F. Nocera,[62] J. Noller,[281] M. Norman,[33] C. North,[33] J. Novak,[116, 235, 282] R. Nowicki,[143] J. F. Nuño Siles,[209] L. K. Nuttall,[73] K. Obayashi,[231] J. Oberling,[2] J. O'Dell,[230] E. Oelker,[35] M. Oertel,[235, 116, 283, 282] G. Oganesyan,[44, 45] T. O'Hanlon,[63] M. Ohashi,[50] F. Ohme,[8, 9] R. Oliveri,[116, 283, 282] R. Omer,[18] B. O'Neal,[122] M. Onishi,[151] K. Oohara,[284] B. O'Reilly,[63] M. Orselli,[51, 76] R. O'Shaughnessy,[110] S. O'Shea,[86] S. Oshino,[50] C. Osthelder,[11] I. Ota,[12] D. J. Ottaway,[115] A. Ouzriat,[56] H. Overmier,[63] B. J. Owen,[285] R. Ozaki,[231] A. E. Pace,[7] R. Pagano,[12] M. A. Page,[25] A. Pai,[196] L. Paiella,[44] A. Pal,[286] S. Pal,[261] M. A. Palaia,[80, 81] M. Pálfi,[204] P. P. Palma,[39, 21, 22] C. Palomba,[38] P. Palud,[20] H. Pan,[141] J. Pan,[72] K. C. Pan,[141] P. K. Panda,[234] Shiksha Pandey,[7] Swadha Pandey,[35] P. T. H. Pang,[37, 71] F. Pannarale,[39, 38] K. A. Pannone,[54] B. C. Pant,[103] F. H. Panther,[72] M. Panzeri,[60, 61] F. Paoletti,[80] A. Paolone,[38, 287] A. Papadopoulos,[86] E. E. Papalexakis,[212] L. Papalini,[80, 81] G. Papigkiotis,[252] A. Paquis,[41] A. Parisi,[76, 51] B.-J. Park,[247] J. Park,[288] W. Parker,[63] G. Pascale,[8, 9] D. Pascucci,[94] A. Pasqualetti,[62] R. Passaquieti,[81, 80] L. Passenger,[6] D. Passuello,[80] O. Patane,[2] A. V. Patel,[140] D. Pathak,[79] A. Patra,[33] B. Patricelli,[81, 80] B. G. Patterson,[33] K. Paul,[106] S. Paul,[77] E. Payne,[11] T. Pearce,[33] M. Pedraza,[11] A. Pele,[11] F. E. Peña Arellano,[289] X. Peng,[118] Y. Peng,[57] S. Penn,[290] M. D. Penuliar,[54] A. Perego,[74, 75] Z. Pereira,[132] C. Périgois,[291, 92, 91] G. Perna,[91] A. Perreca,[74, 75, 44] J. Perret,[20] S. Perriès,[56] J. W. Perry,[37, 107] D. Pesios,[252] S. Peters,[165] S. Petracca,[207] C. Petrillo,[76] H. P. Pfeiffer,[1] H. Pham,[63] K. A. Pham,[18] K. S. Phukon,[118] H. Phurailatpam,[220] M. Piarulli,[100] L. Piccari,[39, 38] O. J. Piccinni,[34] M. Pichot,[113] M. Piendibene,[81, 80] F. Piergiovanni,[60, 61] L. Pierini,[38] G. Pierra,[38] V. Pierro,[292, 131] M. Pietrzak,[95] M. Pillas,[165] F. Pilo,[80] L. Pinard,[177] I. M. Pinto,[292, 131, 293, 32] M. Pinto,[62] B. J. Piotrzkowski,[10] M. Pirello,[2] M. D. Pitkin,[225, 86] A. Placidi,[51] E. Placidi,[39, 38] M. L. Planas,[98] W. Plastino,[213, 22] C. Plunkett,[35] R. Poggiani,[81, 80] E. Polini,[35] J. Pomper,[80, 81] L. Pompili,[1] J. Poon,[220] E. Porcelli,[37] E. K. Porter,[20] C. Posnansky,[7] R. Poulton,[62] J. Powell,[154] G. S. Prabhu,[79] M. Pracchia,[165] B. K. Pradhan,[79] T. Pradier,[64] A. K. Prajapati,[93] K. Prasai,[294] R. Prasanna,[234] P. Prasia,[79] G. Pratten,[118] G. Principe,[186, 48] G. A. Prodi,[74, 75] P. Prosperi,[80] P. Prosposito,[21, 22] A. C. Providence,[65] A. Puecher,[1] J. Pullin,[12] P. Puppo,[38] M. Pürrer,[163] H. Qi,[16] J. Qin,[34] G. Quéméner,[175, 116] V. Quetschke,[164] P. J. Quinonez,[65] N. Qutob,[57] R. Rading,[232] I. Rainho,[137] S. Raja,[103] C. Rajan,[103] B. Rajbhandari,[110] K. E. Ramirez,[63] F. A. Ramis Vidal,[98] M. Ramos Arevalo,[164] A. Ramos-Buades,[98, 37] S. Ranjan,[57] K. Ransom,[63] P. Rapagnani,[39, 38] B. Ratto,[65] A. Ravichandran,[132] A. Ray,[96] V. Raymond,[33] M. Razzano,[81, 80] J. Read,[54] T. Regimbau,[31] S. Reid,[55] C. Reissel,[35] D. H. Reitze,[11] A. I. Renzini,[126, 11] B. Revenu,[295, 41] A. Revilla Peña,[82] R. Reyes,[182] L. Ricca,[15] F. Ricci,[39, 38] M. Ricci,[38, 39] A. Ricciardone,[81, 80] J. Rice,[78] J. W. Richardson,[212] M. L. Richardson,[115] A. Rijal,[65] K. Riles,[90] H. K. Riley,[33] S. Rinaldi,[271] J. Rittmeyer,[97] C. Robertson,[230] F. Robinet,[41] M. Robinson,[2] A. Rocchi,[22] L. Rolland,[31] J. G. Rollins,[11] A. E. Romano,[296] R. Romano,[3, 4] A. Romero,[31] I. M. Romero-Shaw,[225] J. H. Romie,[63] S. Ronchini,[7] T. J. Roocke,[115] L. Rosa,[4, 32] T. J. Rosauer,[212] C. A. Rose,[57] D. Rosińska,[124] M. P. Ross,[53] M. Rossello-Sastre,[98] S. Rowan,[86] S. K. Roy,[192, 193] S. Roy,[15] D. Rozza,[126, 127] P. Ruggi,[62] N. Ruhama,[240]

E. Ruiz Morales,[297,209] K. Ruiz-Rocha,[143] S. Sachdev,[57] T. Sadecki,[2] P. Saffarieh,[37,107] S. Safi-Harb,[168] M. R. Sah,[13] S. Saha,[141] T. Sainrat,[64] S. Sajith Menon,[216,39,38] K. Sakai,[298] Y. Sakai,[273] M. Sakellariadou,[67] S. Sakon,[7] O. S. Salafia,[158,127,126] F. Salces-Carcoba,[11] L. Salconi,[62] M. Saleem,[147] F. Salemi,[39,38] M. Sallé,[37] S. U. Salunkhe,[79] S. Salvador,[175,174] A. Salvarese,[147] A. Samajdar,[71,37] A. Sanchez,[2] E. J. Sanchez,[11] L. E. Sanchez,[11] N. Sanchis-Gual,[137] J. R. Sanders,[183] E. M. Sänger,[1] F. Santoliquido,[44,45] F. Sarandrea,[28] T. R. Saravanan,[79] N. Sarin,[6] P. Sarkar,[8,9] A. Sasli,[252] P. Sassi,[51,76] B. Sassolas,[177] R. Sato,[228] S. Sato,[151] Yukino Sato,[151] Yu Sato,[151] O. Sauter,[46] R. L. Savage,[2] T. Sawada,[50] H. L. Sawant,[79] S. Sayah,[177] V. Scacco,[21,22] D. Schaetzl,[11] M. Scheel,[148] A. Schiebelbein,[191] M. G. Schiworski,[78] P. Schmidt,[118] S. Schmidt,[71] R. Schnabel,[97] M. Schneewind,[8,9] R. M. S. Schofield,[77] K. Schouteden,[109] B. W. Schulte,[8,9] B. F. Schutz,[33,8,9] E. Schwartz,[299] M. Scialpi,[300] J. Scott,[86] S. M. Scott,[34] R. M. Sedas,[63] T. C. Seetharamu,[86] M. Seglar-Arroyo,[43] Y. Sekiguchi,[301] D. Sellers,[63] N. Sembo,[206] A. S. Sengupta,[302] E. G. Seo,[86] J. W. Seo,[109] V. Sequino,[32,4] M. Serra,[38] A. Sevrin,[189] T. Shaffer,[2] U. S. Shah,[57] M. A. Shaikh,[262] L. Shao,[303] A. K. Sharma,[98] Preeti Sharma,[12] Prianka Sharma,[103] Ritwik Sharma,[18] S. Sharma Chaudhary,[105] P. Shawhan,[125] N. S. Shcheblanov,[304,264] E. Sheridan,[143] Z.-H. Shi,[141] M. Shikauchi,[42] R. Shimomura,[305] H. Shinkai,[305] S. Shirke,[79] D. H. Shoemaker,[35] D. M. Shoemaker,[147] R. W. Short,[2] S. ShyamSundar,[103] A. Sider,[157] H. Siegel,[192,193] D. Sigg,[2] L. Silenzi,[36,37] L. Silvestri,[39,169] M. Simmonds,[115] L. P. Singer,[306] Amitesh Singh,[217] Anika Singh,[11] D. Singh,[208] N. Singh,[98] S. Singh,[218,59] A. M. Sintes,[98] V. Sipala,[172,155] V. Skliris,[33] B. J. J. Slagmolen,[34] D. A. Slater,[201] T. J. Slaven-Blair,[72] J. Smetana,[118] J. R. Smith,[54] L. Smith,[86,186,48] R. J. E. Smith,[6] W. J. Smith,[143] S. Soares de Albuquerque Filho,[60] M. Soares-Santos,[190] K. Somiya,[218] I. Song,[141] S. Soni,[35] V. Sordini,[56] F. Sorrentino,[29] H. Sotani,[307] F. Spada,[80] V. Spagnuolo,[37] A. P. Spencer,[86] P. Spinicelli,[62] A. K. Srivastava,[93] F. Stachurski,[86] C. J. Stark,[122] D. A. Steer,[308] N. Steinle,[168] J. Steinlechner,[36,37] S. Steinlechner,[36,37] N. Stergioulas,[252] P. Stevens,[41] M. StPierre,[163] M. D. Strong,[12] A. Strunk,[2] A. L. Stuver,[102,*] M. Suchenek,[95] S. Sudhagar,[95] Y. Sudo,[231] N. Sueltmann,[97] L. Suleiman,[54] K. D. Sullivan,[12] J. Sun,[242] L. Sun,[34] S. Sunil,[93] J. Suresh,[113] B. J. Sutton,[67] P. J. Sutton,[33] K. Suzuki,[218] M. Suzuki,[205] B. L. Swinkels,[37] A. Syx,[116] M. J. Szczepańczyk,[309] P. Szewczyk,[124] M. Tacca,[37] H. Tagoshi,[205] K. Takada,[205] H. Takahashi,[273] R. Takahashi,[25] A. Takamori,[42] S. Takano,[310] H. Takeda,[311,312] K. Takeshita,[218] I. Takimoto Schmiegelow,[44,45] M. Takou-Ayaoh,[78] C. Talbot,[129] M. Tamaki,[205] N. Tamanini,[100] D. Tanabe,[140] K. Tanaka,[50] S. J. Tanaka,[231] S. Tanioka,[33] D. B. Tanner,[46] W. Tanner,[8,9] L. Tao,[212] R. D. Tapia,[7] E. N. Tapia San Martín,[37] C. Taranto,[21,22] A. Taruya,[313] J. D. Tasson,[152] J. G. Tau,[110] D. Tellez,[54] R. Tenorio,[98] H. Themann,[182] A. Theodoropoulos,[137] M. P. Thirugnanasambandam,[79] L. M. Thomas,[11] M. Thomas,[63] P. Thomas,[2] J. E. Thompson,[211] S. R. Thondapu,[103] K. A. Thorne,[63] E. Thrane,[6] J. Tissino,[44,45] A. Tiwari,[79] Pawan Tiwari,[44] Praveer Tiwari,[196] S. Tiwari,[190] V. Tiwari,[118] M. R. Todd,[78] M. Toffano,[91] A. M. Toivonen,[18] K. Toland,[86] A. E. Tolley,[73] T. Tomaru,[25] V. Tommasini,[11] T. Tomura,[50] H. Tong,[6] C. Tong-Yu,[140] A. Torres-Forné,[137,138] C. I. Torrie,[11] I. Tosta e Melo,[314] E. Tournefier,[31] M. Trad Nery,[113] K. Tran,[122] A. Trapananti,[52,51] R. Travaglini,[167] F. Travasso,[52,51] G. Traylor,[63] M. Trevor,[125] M. C. Tringali,[62] A. Tripathee,[90] G. Troian,[186,48] A. Trovato,[186,48] L. Trozzo,[4] R. J. Trudeau,[11] T. Tsang,[33] S. Tsuchida,[315] L. Tsukada,[214] K. Turbang,[189,23] M. Turconi,[113] C. Turski,[94] H. Ubach,[82,83] T. Uchiyama,[50] R. P. Udall,[11] T. Uehara,[316] K. Ueno,[42] V. Undheim,[278] L. E. Uronen,[220] T. Ushiba,[50] M. Vacatello,[80,81] H. Vahlbruch,[8,9] N. Vaidya,[11] G. Vajente,[11] A. Vajpeyi,[6] J. Valencia,[98] M. Valentini,[107,37] S. A. Vallejo-Peña,[296] S. Vallero,[28] V. Valsan,[10] M. van Dael,[37,317] E. Van den Bossche,[189] J. F. J. van den Brand,[36,107,37] C. Van Den Broeck,[71,37] M. van der Sluys,[37,71] A. Van de Walle,[41] J. van Dongen,[37,107] K. Vandra,[102] M. VanDyke,[119] H. van Haevermaet,[23] J. V. van Heijningen,[37,107] P. Van Hove,[64] J. Vanier,[260] M. VanKeuren,[104] J. Vanosky,[2] N. van Remortel,[23] M. Vardaro,[36,37] A. F. Vargas,[123] V. Varma,[132] A. N. Vazquez,[89] A. Vecchio,[118] G. Vedovato,[92] J. Veitch,[86] P. J. Veitch,[115] S. Venikoudis,[15] R. C. Venterea,[18] P. Verdier,[56] M. Vereecken,[15] D. Verkindt,[31] B. Verma,[132] Y. Verma,[103] S. M. Vermeulen,[11] F. Vetrano,[60] A. Veutro,[38,39] A. Viceré,[60,61] S. Vidyant,[78] A. D. Viets,[88] A. Vijaykumar,[191] A. Vilkha,[110] N. Villanueva Espinosa,[137] V. Villa-Ortega,[179] E. T. Vincent,[57] J.-Y. Vinet,[113] S. Viret,[56] S. Vitale,[35] H. Vocca,[76,51] D. Voigt,[97] E. R. G. von Reis,[2] J. S. A. von Wrangel,[8,9] W. E. Vossius,[232] L. Vujeva,[139] S. P. Vyatchanin,[108] J. Wack,[11] L. E. Wade,[104] M. Wade,[104] K. J. Wagner,[110] L. Wallace,[11] E. J. Wang,[89] H. Wang,[218] J. Z. Wang,[90] W. H. Wang,[164] Y. F. Wang,[1] G. Waratkar,[196] J. Warner,[2] M. Was,[31] T. Washimi,[25] N. Y. Washington,[11] D. Watarai,[42] B. Weaver,[2] S. A. Webster,[86] N. L. Weickhardt,[97] M. Weinert,[8,9] A. J. Weinstein,[11] R. Weiss,[35] L. Wen,[72]

K. Wette ,[34] J. T. Whelan ,[110] B. F. Whiting ,[46] C. Whittle ,[11] E. G. Wickens,[73] D. Wilken ,[8,9,9]
A. T. Wilkin,[212] B. M. Williams,[119] D. Williams ,[86] M. J. Williams ,[73] N. S. Williams ,[1] J. L. Willis ,[11]
B. Willke ,[9,8,9] M. Wils ,[109] L. Wilson,[104] C. W. Winborn,[105] J. Winterflood,[72] C. C. Wipf,[11] G. Woan ,[86]
J. Woehler,[36,37] N. E. Wolfe,[35] H. T. Wong ,[140] I. C. F. Wong ,[220,109] K. Wong,[191] T. Wouters,[71,37]
J. L. Wright,[2] M. Wright ,[86,71] B. Wu,[78] C. Wu ,[141] D. S. Wu ,[8,9] H. Wu ,[141] K. Wu,[119] Q. Wu,[53] Y. Wu,[96]
Z. Wu ,[100] E. Wuchner,[54] D. M. Wysocki ,[10] V. A. Xu ,[208] Y. Xu ,[98] N. Yadav ,[28] H. Yamamoto ,[11]
K. Yamamoto ,[151] T. S. Yamamoto ,[42] T. Yamamoto ,[50] R. Yamazaki ,[231] T. Yan,[118] K. Z. Yang ,[18]
Y. Yang ,[145] Z. Yarbrough ,[12] J. Yebana,[98] S.-W. Yeh,[141] A. B. Yelikar ,[143] X. Yin,[35] J. Yokoyama ,[318,42]
T. Yokozawa,[50] S. Yuan,[72] H. Yuzurihara ,[50] M. Zanolin,[65] M. Zeeshan ,[110] T. Zelenova,[62] J.-P. Zendri,[92]
M. Zeoli ,[15] M. Zerrad,[40] M. Zevin ,[96] L. Zhang,[11] N. Zhang,[57] R. Zhang ,[149] T. Zhang,[118] C. Zhao ,[72]
Yue Zhao,[161] Yuhang Zhao,[20] Z.-C. Zhao ,[319] Y. Zheng ,[105] H. Zhong ,[18] H. Zhou,[78] H. O. Zhu,[72]
Z.-H. Zhu ,[319,320] A. B. Zimmerman ,[147] L. Zimmermann,[56] M. E. Zucker ,[35,11] and J. Zweizig [11]

[1] *Max Planck Institute for Gravitational Physics (Albert Einstein Institute), D-14476 Potsdam, Germany*
[2] *LIGO Hanford Observatory, Richland, WA 99352, USA*
[3] *Dipartimento di Farmacia, Università di Salerno, I-84084 Fisciano, Salerno, Italy*
[4] *INFN, Sezione di Napoli, I-80126 Napoli, Italy*
[5] *University of Warwick, Coventry CV4 7AL, United Kingdom*
[6] *OzGrav, School of Physics & Astronomy, Monash University, Clayton 3800, Victoria, Australia*
[7] *The Pennsylvania State University, University Park, PA 16802, USA*
[8] *Max Planck Institute for Gravitational Physics (Albert Einstein Institute), D-30167 Hannover, Germany*
[9] *Leibniz Universität Hannover, D-30167 Hannover, Germany*
[10] *University of Wisconsin-Milwaukee, Milwaukee, WI 53201, USA*
[11] *LIGO Laboratory, California Institute of Technology, Pasadena, CA 91125, USA*
[12] *Louisiana State University, Baton Rouge, LA 70803, USA*
[13] *Tata Institute of Fundamental Research, Mumbai 400005, India*
[14] *Centre de Physique Théorique, Aix-Marseille Université, Campus de Luminy, 163 Av. de Luminy, 13009 Marseille, France*
[15] *Université catholique de Louvain, B-1348 Louvain-la-Neuve, Belgium*
[16] *Queen Mary University of London, London E1 4NS, United Kingdom*
[17] *University of California, Davis, Davis, CA 95616, USA*
[18] *University of Minnesota, Minneapolis, MN 55455, USA*
[19] *Instituto Nacional de Pesquisas Espaciais, 12227-010 São José dos Campos, São Paulo, Brazil*
[20] *Université Paris Cité, CNRS, Astroparticule et Cosmologie, F-75013 Paris, France*
[21] *Università di Roma Tor Vergata, I-00133 Roma, Italy*
[22] *INFN, Sezione di Roma Tor Vergata, I-00133 Roma, Italy*
[23] *Universiteit Antwerpen, 2000 Antwerpen, Belgium*
[24] *International Centre for Theoretical Sciences, Tata Institute of Fundamental Research, Bengaluru 560089, India*
[25] *Gravitational Wave Science Project, National Astronomical Observatory of Japan, 2-21-1 Osawa, Mitaka City, Tokyo 181-8588, Japan*
[26] *Advanced Technology Center, National Astronomical Observatory of Japan, 2-21-1 Osawa, Mitaka City, Tokyo 181-8588, Japan*
[27] *Theoretisch-Physikalisches Institut, Friedrich-Schiller-Universität Jena, D-07743 Jena, Germany*
[28] *INFN Sezione di Torino, I-10125 Torino, Italy*
[29] *INFN, Sezione di Genova, I-16146 Genova, Italy*
[30] *Dipartimento di Fisica, Università degli Studi di Genova, I-16146 Genova, Italy*
[31] *Univ. Savoie Mont Blanc, CNRS, Laboratoire d'Annecy de Physique des Particules - IN2P3, F-74000 Annecy, France*
[32] *Università di Napoli "Federico II", I-80126 Napoli, Italy*
[33] *Cardiff University, Cardiff CF24 3AA, United Kingdom*
[34] *OzGrav, Australian National University, Canberra, Australian Capital Territory 0200, Australia*
[35] *LIGO Laboratory, Massachusetts Institute of Technology, Cambridge, MA 02139, USA*
[36] *Maastricht University, 6200 MD Maastricht, Netherlands*
[37] *Nikhef, 1098 XG Amsterdam, Netherlands*
[38] *INFN, Sezione di Roma, I-00185 Roma, Italy*
[39] *Università di Roma "La Sapienza", I-00185 Roma, Italy*
[40] *Aix Marseille Univ, CNRS, Centrale Med, Institut Fresnel, F-13013 Marseille, France*
[41] *Université Paris-Saclay, CNRS/IN2P3, IJCLab, 91405 Orsay, France*
[42] *University of Tokyo, Tokyo, 113-0033, Japan*
[43] *Institut de Física d'Altes Energies (IFAE), The Barcelona Institute of Science and Technology, Campus UAB, E-08193 Bellaterra (Barcelona), Spain*
[44] *Gran Sasso Science Institute (GSSI), I-67100 L'Aquila, Italy*
[45] *INFN, Laboratori Nazionali del Gran Sasso, I-67100 Assergi, Italy*

[46] University of Florida, Gainesville, FL 32611, USA
[47] Dipartimento di Scienze Matematiche, Informatiche e Fisiche, Università di Udine, I-33100 Udine, Italy
[48] INFN, Sezione di Trieste, I-34127 Trieste, Italy
[49] Tecnologico de Monterrey, Escuela de Ingeniería y Ciencias, 64849 Monterrey, Nuevo León, Mexico
[50] Institute for Cosmic Ray Research, KAGRA Observatory, The University of Tokyo, 238 Higashi-Mozumi, Kamioka-cho, Hida City, Gifu 506-1205, Japan
[51] INFN, Sezione di Perugia, I-06123 Perugia, Italy
[52] Università di Camerino, I-62032 Camerino, Italy
[53] University of Washington, Seattle, WA 98195, USA
[54] California State University Fullerton, Fullerton, CA 92831, USA
[55] SUPA, University of Strathclyde, Glasgow G1 1XQ, United Kingdom
[56] Université Claude Bernard Lyon 1, CNRS, IP2I Lyon / IN2P3, UMR 5822, F-69622 Villeurbanne, France
[57] Georgia Institute of Technology, Atlanta, GA 30332, USA
[58] Royal Holloway, University of London, London TW20 0EX, United Kingdom
[59] Astronomical course, The Graduate University for Advanced Studies (SOKENDAI), 2-21-1 Osawa, Mitaka City, Tokyo 181-8588, Japan
[60] Università degli Studi di Urbino "Carlo Bo", I-61029 Urbino, Italy
[61] INFN, Sezione di Firenze, I-50019 Sesto Fiorentino, Firenze, Italy
[62] European Gravitational Observatory (EGO), I-56021 Cascina, Pisa, Italy
[63] LIGO Livingston Observatory, Livingston, LA 70754, USA
[64] Université de Strasbourg, CNRS, IPHC UMR 7178, F-67000 Strasbourg, France
[65] Embry-Riddle Aeronautical University, Prescott, AZ 86301, USA
[66] Dipartimento di Fisica "E.R. Caianiello", Università di Salerno, I-84084 Fisciano, Salerno, Italy
[67] King's College London, University of London, London WC2R 2LS, United Kingdom
[68] Korea Institute of Science and Technology Information, Daejeon 34141, Republic of Korea
[69] International College, Osaka University, 1-1 Machikaneyama-cho, Toyonaka City, Osaka 560-0043, Japan
[70] Accelerator Laboratory, High Energy Accelerator Research Organization (KEK), 1-1 Oho, Tsukuba City, Ibaraki 305-0801, Japan
[71] Institute for Gravitational and Subatomic Physics (GRASP), Utrecht University, 3584 CC Utrecht, Netherlands
[72] OzGrav, University of Western Australia, Crawley, Western Australia 6009, Australia
[73] University of Portsmouth, Portsmouth, PO1 3FX, United Kingdom
[74] Università di Trento, Dipartimento di Fisica, I-38123 Povo, Trento, Italy
[75] INFN, Trento Institute for Fundamental Physics and Applications, I-38123 Povo, Trento, Italy
[76] Università di Perugia, I-06123 Perugia, Italy
[77] University of Oregon, Eugene, OR 97403, USA
[78] Syracuse University, Syracuse, NY 13244, USA
[79] Inter-University Centre for Astronomy and Astrophysics, Pune 411007, India
[80] INFN, Sezione di Pisa, I-56127 Pisa, Italy
[81] Università di Pisa, I-56127 Pisa, Italy
[82] Institut de Ciències del Cosmos (ICCUB), Universitat de Barcelona (UB), c. Martí i Franquès, 1, 08028 Barcelona, Spain
[83] Departament de Física Quàntica i Astrofísica (FQA), Universitat de Barcelona (UB), c. Martí i Franqués, 1, 08028 Barcelona, Spain
[84] Institut d'Estudis Espacials de Catalunya, c. Gran Capità, 2-4, 08034 Barcelona, Spain
[85] Dipartimento di Medicina, Chirurgia e Odontoiatria "Scuola Medica Salernitana", Università di Salerno, I-84081 Baronissi, Salerno, Italy
[86] IGR, University of Glasgow, Glasgow G12 8QQ, United Kingdom
[87] HUN-REN Wigner Research Centre for Physics, H-1121 Budapest, Hungary
[88] Concordia University Wisconsin, Mequon, WI 53097, USA
[89] Stanford University, Stanford, CA 94305, USA
[90] University of Michigan, Ann Arbor, MI 48109, USA
[91] Università di Padova, Dipartimento di Fisica e Astronomia, I-35131 Padova, Italy
[92] INFN, Sezione di Padova, I-35131 Padova, Italy
[93] Institute for Plasma Research, Bhat, Gandhinagar 382428, India
[94] Universiteit Gent, B-9000 Gent, Belgium
[95] Nicolaus Copernicus Astronomical Center, Polish Academy of Sciences, 00-716, Warsaw, Poland
[96] Northwestern University, Evanston, IL 60208, USA
[97] Universität Hamburg, D-22761 Hamburg, Germany
[98] IAC3–IEEC, Universitat de les Illes Balears, E-07122 Palma de Mallorca, Spain
[99] Aix-Marseille Université, Université de Toulon, CNRS, CPT, Marseille, France
[100] Laboratoire des 2 Infinis - Toulouse (L2IT-IN2P3), F-31062 Toulouse Cedex 9, France
[101] Università di Siena, Dipartimento di Scienze Fisiche, della Terra e dell'Ambiente, I-53100 Siena, Italy

[102]Villanova University, Villanova, PA 19085, USA
[103]RRCAT, Indore, Madhya Pradesh 452013, India
[104]Kenyon College, Gambier, OH 43022, USA
[105]Missouri University of Science and Technology, Rolla, MO 65409, USA
[106]Indian Institute of Technology Madras, Chennai 600036, India
[107]Department of Physics and Astronomy, Vrije Universiteit Amsterdam, 1081 HV Amsterdam, Netherlands
[108]Lomonosov Moscow State University, Moscow 119991, Russia
[109]Katholieke Universiteit Leuven, Oude Markt 13, 3000 Leuven, Belgium
[110]Rochester Institute of Technology, Rochester, NY 14623, USA
[111]Université libre de Bruxelles, 1050 Bruxelles, Belgium
[112]Bar-Ilan University, Ramat Gan, 5290002, Israel
[113]Université Côte d'Azur, Observatoire de la Côte d'Azur, CNRS, Artemis, F-06304 Nice, France
[114]University of British Columbia, Vancouver, BC V6T 1Z4, Canada
[115]OzGrav, University of Adelaide, Adelaide, South Australia 5005, Australia
[116]Centre national de la recherche scientifique, 75016 Paris, France
[117]Univ Rennes, CNRS, Institut FOTON - UMR 6082, F-35000 Rennes, France
[118]University of Birmingham, Birmingham B15 2TT, United Kingdom
[119]Washington State University, Pullman, WA 99164, USA
[120]Cornell University, Ithaca, NY 14850, USA
[121]Laboratoire Kastler Brossel, Sorbonne Université, CNRS, ENS-Université PSL, Collège de France, F-75005 Paris, France
[122]Christopher Newport University, Newport News, VA 23606, USA
[123]OzGrav, University of Melbourne, Parkville, Victoria 3010, Australia
[124]Astronomical Observatory Warsaw University, 00-478 Warsaw, Poland
[125]University of Maryland, College Park, MD 20742, USA
[126]Università degli Studi di Milano-Bicocca, I-20126 Milano, Italy
[127]INFN, Sezione di Milano-Bicocca, I-20126 Milano, Italy
[128]Université de Lyon, Université Claude Bernard Lyon 1, CNRS, Institut Lumière Matière, F-69622 Villeurbanne, France
[129]University of Chicago, Chicago, IL 60637, USA
[130]University of Arizona, Tucson, AZ 85721, USA
[131]INFN, Sezione di Napoli, Gruppo Collegato di Salerno, I-80126 Napoli, Italy
[132]University of Massachusetts Dartmouth, North Dartmouth, MA 02747, USA
[133]Niels Bohr Institute, Copenhagen University, 2100 København, Denmark
[134]Universidad de Guadalajara, 44430 Guadalajara, Jalisco, Mexico
[135]Istituto di Astrofisica e Planetologia Spaziali di Roma, 00133 Roma, Italy
[136]Colorado State University, Fort Collins, CO 80523, USA
[137]Departamento de Astronomía y Astrofísica, Universitat de València, E-46100 Burjassot, València, Spain
[138]Observatori Astronòmic, Universitat de València, E-46980 Paterna, València, Spain
[139]Niels Bohr Institute, University of Copenhagen, 2100 Kóbenhavn, Denmark
[140]National Central University, Taoyuan City 320317, Taiwan
[141]National Tsing Hua University, Hsinchu City 30013, Taiwan
[142]OzGrav, Charles Sturt University, Wagga Wagga, New South Wales 2678, Australia
[143]Vanderbilt University, Nashville, TN 37235, USA
[144]University of the Chinese Academy of Sciences / International Centre for Theoretical Physics Asia-Pacific, Bejing 100049, China
[145]Department of Electrophysics, National Yang Ming Chiao Tung University, 101 Univ. Street, Hsinchu, Taiwan
[146]Kamioka Branch, National Astronomical Observatory of Japan, 238 Higashi-Mozumi, Kamioka-cho, Hida City, Gifu 506-1205, Japan
[147]University of Texas, Austin, TX 78712, USA
[148]CaRT, California Institute of Technology, Pasadena, CA 91125, USA
[149]Northeastern University, Boston, MA 02115, USA
[150]Dipartimento di Ingegneria Industriale (DIIN), Università di Salerno, I-84084 Fisciano, Salerno, Italy
[151]Faculty of Science, University of Toyama, 3190 Gofuku, Toyama City, Toyama 930-8555, Japan
[152]Carleton College, Northfield, MN 55057, USA
[153]University of Szeged, Dóm tér 9, Szeged 6720, Hungary
[154]OzGrav, Swinburne University of Technology, Hawthorn VIC 3122, Australia
[155]INFN Cagliari, Physics Department, Università degli Studi di Cagliari, Cagliari 09042, Italy
[156]Università degli Studi di Cagliari, Via Università 40, 09124 Cagliari, Italy
[157]Université Libre de Bruxelles, Brussels 1050, Belgium
[158]INAF, Osservatorio Astronomico di Brera sede di Merate, I-23807 Merate, Lecco, Italy
[159]Departamento de Matemáticas, Universitat de València, E-46100 Burjassot, València, Spain
[160]Montana State University, Bozeman, MT 59717, USA

[161] The University of Utah, Salt Lake City, UT 84112, USA
[162] Johns Hopkins University, Baltimore, MD 21218, USA
[163] University of Rhode Island, Kingston, RI 02881, USA
[164] The University of Texas Rio Grande Valley, Brownsville, TX 78520, USA
[165] Université de Liège, B-4000 Liège, Belgium
[166] DIFA- Alma Mater Studiorum Università di Bologna, Via Zamboni, 33 - 40126 Bologna, Italy
[167] Istituto Nazionale Di Fisica Nucleare - Sezione di Bologna, viale Carlo Berti Pichat 6/2 - 40127 Bologna, Italy
[168] University of Manitoba, Winnipeg, MB R3T 2N2, Canada
[169] INFN-CNAF - Bologna, Viale Carlo Berti Pichat, 6/2, 40127 Bologna BO, Italy
[170] Dipartimento di Fisica e Astronomia, Alma Mater Studiorum - Università di Bologna, Via Piero Gobetti 93/2 - 40129 Bologna, Italy
[171] Istituto Nazionale di Fisica Nucleare, sede di Bologna, viale C. Berti-Pichat 6/2 - 40127 Bologna, Italy
[172] Università degli Studi di Sassari, I-07100 Sassari, Italy
[173] INFN, Laboratori Nazionali del Sud, I-95125 Catania, Italy
[174] Université de Normandie, ENSICAEN, UNICAEN, CNRS/IN2P3, LPC Caen, F-14000 Caen, France
[175] Laboratoire de Physique Corpusculaire Caen, 6 boulevard du maréchal Juin, F-14050 Caen, France
[176] The University of Sheffield, Sheffield S10 2TN, United Kingdom
[177] Université Claude Bernard Lyon 1, CNRS, Laboratoire des Matériaux Avancés (LMA), IP2I Lyon / IN2P3, UMR 5822, F-69622 Villeurbanne, France
[178] Università di Firenze, Sesto Fiorentino I-50019, Italy
[179] IGFAE, Universidade de Santiago de Compostela, E-15782 Santiago de Compostela, Spain
[180] Dipartimento di Scienze Matematiche, Fisiche e Informatiche, Università di Parma, I-43124 Parma, Italy
[181] INFN, Sezione di Milano Bicocca, Gruppo Collegato di Parma, I-43124 Parma, Italy
[182] California State University, Los Angeles, Los Angeles, CA 90032, USA
[183] Marquette University, Milwaukee, WI 53233, USA
[184] Perimeter Institute, Waterloo, ON N2L 2Y5, Canada
[185] Corps des Mines, Mines Paris, Université PSL, 60 Bd Saint-Michel, 75272 Paris, France
[186] Dipartimento di Fisica, Università di Trieste, I-34127 Trieste, Italy
[187] Université Côte d'Azur, Observatoire de la Côte d'Azur, CNRS, Lagrange, F-06304 Nice, France
[188] National Center for Nuclear Research, 05-400 Świerk-Otwock, Poland
[189] Vrije Universiteit Brussel, 1050 Brussel, Belgium
[190] University of Zurich, Winterthurerstrasse 190, 8057 Zurich, Switzerland
[191] Canadian Institute for Theoretical Astrophysics, University of Toronto, Toronto, ON M5S 3H8, Canada
[192] Stony Brook University, Stony Brook, NY 11794, USA
[193] Center for Computational Astrophysics, Flatiron Institute, New York, NY 10010, USA
[194] Montclair State University, Montclair, NJ 07043, USA
[195] HUN-REN Institute for Nuclear Research, H-4026 Debrecen, Hungary
[196] Indian Institute of Technology Bombay, Powai, Mumbai 400 076, India
[197] Centro de Física das Universidades do Minho e do Porto, Universidade do Minho, PT-4710-057 Braga, Portugal
[198] Aix Marseille Univ, CNRS/IN2P3, CPPM, Marseille, France
[199] CNR-SPIN, I-84084 Fisciano, Salerno, Italy
[200] Scuola di Ingegneria, Università della Basilicata, I-85100 Potenza, Italy
[201] Western Washington University, Bellingham, WA 98225, USA
[202] SUPA, University of the West of Scotland, Paisley PA1 2BE, United Kingdom
[203] Barry University, Miami Shores, FL 33168, USA
[204] Eötvös University, Budapest 1117, Hungary
[205] Institute for Cosmic Ray Research, KAGRA Observatory, The University of Tokyo, 5-1-5 Kashiwa-no-Ha, Kashiwa City, Chiba 277-8582, Japan
[206] Department of Physics, Graduate School of Science, Osaka Metropolitan University, 3-3-138 Sugimoto-cho, Sumiyoshi-ku, Osaka City, Osaka 558-8585, Japan
[207] University of Sannio at Benevento, I-82100 Benevento, Italy and INFN, Sezione di Napoli, I-80100 Napoli, Italy
[208] University of California, Berkeley, CA 94720, USA
[209] Instituto de Fisica Teorica UAM-CSIC, Universidad Autonoma de Madrid, 28049 Madrid, Spain
[210] Laboratoire d'Acoustique de l'Université du Mans, UMR CNRS 6613, F-72085 Le Mans, France
[211] University of Southampton, Southampton SO17 1BJ, United Kingdom
[212] University of California, Riverside, Riverside, CA 92521, USA

[213] *Dipartimento di Ingegneria Industriale, Elettronica e Meccanica, Università degli Studi Roma Tre, I-00146 Roma, Italy*
[214] *University of Nevada, Las Vegas, Las Vegas, NV 89154, USA*
[215] *University of Nottingham NG7 2RD, UK*
[216] *Ariel University, Ramat HaGolan St 65, Ari'el, Israel*
[217] *The University of Mississippi, University, MS 38677, USA*
[218] *Graduate School of Science, Institute of Science Tokyo, 2-12-1 Ookayama, Meguro-ku, Tokyo 152-8551, Japan*
[219] *Institute of Physics, Academia Sinica, 128 Sec. 2, Academia Rd., Nankang, Taipei 11529, Taiwan*
[220] *The Chinese University of Hong Kong, Shatin, NT, Hong Kong*
[221] *American University, Washington, DC 20016, USA*
[222] *Dipartimento di Fisica, Università degli studi di Milano, Via Celoria 16, I-20133, Milano, Italy*
[223] *INFN, sezione di Milano, Via Celoria 16, I-20133, Milano, Italy*
[224] *Department of Applied Physics, Fukuoka University, 8-19-1 Nanakuma, Jonan, Fukuoka City, Fukuoka 814-0180, Japan*
[225] *University of Cambridge, Cambridge CB2 1TN, United Kingdom*
[226] *University of Lancaster, Lancaster LA1 4YW, United Kingdom*
[227] *College of Industrial Technology, Nihon University, 1-2-1 Izumi, Narashino City, Chiba 275-8575, Japan*
[228] *Faculty of Engineering, Niigata University, 8050 Ikarashi-2-no-cho, Nishi-ku, Niigata City, Niigata 950-2181, Japan*
[229] *Department of Physics, Tamkang University, No. 151, Yingzhuan Rd., Danshui Dist., New Taipei City 25137, Taiwan*
[230] *Rutherford Appleton Laboratory, Didcot OX11 0DE, United Kingdom*
[231] *Department of Physical Sciences, Aoyama Gakuin University, 5-10-1 Fuchinobe, Sagamihara City, Kanagawa 252-5258, Japan*
[232] *Helmut Schmidt University, D-22043 Hamburg, Germany*
[233] *Nambu Yoichiro Institute of Theoretical and Experimental Physics (NITEP), Osaka Metropolitan University, 3-3-138 Sugimoto-cho, Sumiyoshi-ku, Osaka City, Osaka 558-8585, Japan*
[234] *Directorate of Construction, Services & Estate Management, Mumbai 400094, India*
[235] *Observatoire Astronomique de Strasbourg, 11 Rue de l'Université, 67000 Strasbourg, France*
[236] *Faculty of Physics, University of Białystok, 15-245 Białystok, Poland*
[237] *National Astronomical Observatories, Chinese Academic of Sciences, 20A Datun Road, Chaoyang District, Beijing, China*
[238] *School of Astronomy and Space Science, University of Chinese Academy of Sciences, 20A Datun Road, Chaoyang District, Beijing, China*
[239] *Sungkyunkwan University, Seoul 03063, Republic of Korea*
[240] *Department of Physics, Ulsan National Institute of Science and Technology (UNIST), 50 UNIST-gil, Ulju-gun, Ulsan 44919, Republic of Korea*
[241] *Institute for Cosmic Ray Research, The University of Tokyo, 5-1-5 Kashiwa-no-Ha, Kashiwa City, Chiba 277-8582, Japan*
[242] *Chung-Ang University, Seoul 06974, Republic of Korea*
[243] *University of Washington Bothell, Bothell, WA 98011, USA*
[244] *Laboratoire de Physique et de Chimie de l'Environnement, Université Joseph KI-ZERBO, 9GH2+3V5, Ouagadougou, Burkina Faso*
[245] *Ewha Womans University, Seoul 03760, Republic of Korea*
[246] *National Institute for Mathematical Sciences, Daejeon 34047, Republic of Korea*
[247] *Korea Astronomy and Space Science Institute, Daejeon 34055, Republic of Korea*
[248] *Department of Astronomy and Space Science, Chungnam National University, 9 Daehak-ro, Yuseong-gu, Daejeon 34134, Republic of Korea*
[249] *Institute of Particle and Nuclear Studies (IPNS), High Energy Accelerator Research Organization (KEK), 1-1 Oho, Tsukuba City, Ibaraki 305-0801, Japan*
[250] *Division of Science, National Astronomical Observatory of Japan, 2-21-1 Osawa, Mitaka City, Tokyo 181-8588, Japan*
[251] *Nagoya University, Nagoya, 464-8601, Japan*
[252] *Department of Physics, Aristotle University of Thessaloniki, 54124 Thessaloniki, Greece*
[253] *Bard College, Annandale-On-Hudson, NY 12504, USA*
[254] *Technical University of Braunschweig, D-38106 Braunschweig, Germany*
[255] *Institute of Mathematics, Polish Academy of Sciences, 00656 Warsaw, Poland*
[256] *Astronomical Observatory, Jagiellonian University, 31-007 Cracow, Poland*
[257] *Department of Physics and Astronomy, University of Padova, Via Marzolo, 8-35151 Padova, Italy*
[258] *Sezione di Padova, Istituto Nazionale di Fisica Nucleare (INFN), Via Marzolo, 8-35131 Padova, Italy*

[259] *Department of Physics, Nagoya University, ES building, Furocho, Chikusa-ku, Nagoya, Aichi 464-8602, Japan*
[260] *Université de Montréal/Polytechnique, Montreal, Quebec H3T 1J4, Canada*
[261] *Indian Institute of Science Education and Research, Kolkata, Mohanpur, West Bengal 741252, India*
[262] *Seoul National University, Seoul 08826, Republic of Korea*
[263] *Department of Computer Simulation, Inje University, 197 Inje-ro, Gimhae, Gyeongsangnam-do 50834, Republic of Korea*
[264] *NAVIER, École des Ponts, Univ Gustave Eiffel, CNRS, Marne-la-Vallée, France*
[265] *Gravitational Wave Science Project, National Astronomical Observatory of Japan (NAOJ), Mitaka City, Tokyo 181-8588, Japan*
[266] *Department of Physics, National Cheng Kung University, No.1, University Road, Tainan City 701, Taiwan*
[267] *St. Thomas University, Miami Gardens, FL 33054, USA*
[268] *Scuola Normale Superiore, I-56126 Pisa, Italy*
[269] *Institució Catalana de Recerca i Estudis Avançats, E-08010 Barcelona, Spain*
[270] *Institut de Física d'Altes Energies, E-08193 Barcelona, Spain*
[271] *Institut fuer Theoretische Astrophysik, Zentrum fuer Astronomie Heidelberg, Universitaet Heidelberg, Albert Ueberle Str. 2, 69120 Heidelberg, Germany*
[272] *Institucio Catalana de Recerca i Estudis Avançats (ICREA), Passeig de Lluís Companys, 23, 08010 Barcelona, Spain*
[273] *Research Center for Space Science, Advanced Research Laboratories, Tokyo City University, 3-3-1 Ushikubo-Nishi, Tsuzuki-Ku, Yokohama, Kanagawa 224-8551, Japan*
[274] *Tsinghua University, Beijing 100084, China*
[275] *Institut des Hautes Etudes Scientifiques, F-91440 Bures-sur-Yvette, France*
[276] *Faculty of Law, Ryukoku University, 67 Fukakusa Tsukamoto-cho, Fushimi-ku, Kyoto City, Kyoto 612-8577, Japan*
[277] *Phenikaa Institute for Advanced Study (PIAS), Phenikaa University, Yen Nghia, Ha Dong, Hanoi, Vietnam*
[278] *University of Stavanger, 4021 Stavanger, Norway*
[279] *Physics Program, Graduate School of Advanced Science and Engineering, Hiroshima University, 1-3-1 Kagamiyama, Higashihiroshima City, Hiroshima 739-8526, Japan*
[280] *GRAPPA, Anton Pannekoek Institute for Astronomy and Institute for High-Energy Physics, University of Amsterdam, 1098 XH Amsterdam, Netherlands*
[281] *University College London, London WC1E 6BT, United Kingdom*
[282] *Observatoire de Paris, 75014 Paris, France*
[283] *Laboratoire Univers et Théories, Observatoire de Paris, 92190 Meudon, France*
[284] *Graduate School of Science and Technology, Niigata University, 8050 Ikarashi-2-no-cho, Nishi-ku, Niigata City, Niigata 950-2181, Japan*
[285] *University of Maryland, Baltimore County, Baltimore, MD 21250, USA*
[286] *CSIR-Central Glass and Ceramic Research Institute, Kolkata, West Bengal 700032, India*
[287] *Consiglio Nazionale delle Ricerche - Istituto dei Sistemi Complessi, I-00185 Roma, Italy*
[288] *Department of Astronomy, Yonsei University, 50 Yonsei-Ro, Seodaemun-Gu, Seoul 03722, Republic of Korea*
[289] *Department of Physics, University of Guadalajara, Av. Revolucion 1500, Colonia Olimpica C.P. 44430, Guadalajara, Jalisco, Mexico*
[290] *Hobart and William Smith Colleges, Geneva, NY 14456, USA*
[291] *INAF, Osservatorio Astronomico di Padova, I-35122 Padova, Italy*
[292] *Dipartimento di Ingegneria, Università del Sannio, I-82100 Benevento, Italy*
[293] *Museo Storico della Fisica e Centro Studi e Ricerche "Enrico Fermi", I-00184 Roma, Italy*
[294] *Kennesaw State University, Kennesaw, GA 30144, USA*
[295] *Subatech, CNRS/IN2P3 - IMT Atlantique - Nantes Université, 4 rue Alfred Kastler BP 20722 44307 Nantes CÉDEX 03, France*
[296] *Universidad de Antioquia, Medellín, Colombia*
[297] *Departamento de Física - ETSIDI, Universidad Politécnica de Madrid, 28012 Madrid, Spain*
[298] *Department of Electronic Control Engineering, National Institute of Technology, Nagaoka College, 888 Nishikatakai, Nagaoka City, Niigata 940-8532, Japan*
[299] *Trinity College, Hartford, CT 06106, USA*
[300] *Dipartimento di Fisica e Scienze della Terra, Università Degli Studi di Ferrara, Via Saragat, 1, 44121 Ferrara FE, Italy*
[301] *Faculty of Science, Toho University, 2-2-1 Miyama, Funabashi City, Chiba 274-8510, Japan*
[302] *Indian Institute of Technology, Palaj, Gandhinagar, Gujarat 382355, India*
[303] *Kavli Institute for Astronomy and Astrophysics, Peking University, Yiheyuan Road 5, Haidian District, Beijing 100871, China*

[304]*Laboratoire MSME, Cité Descartes, 5 Boulevard Descartes, Champs-sur-Marne, 77454 Marne-la-Vallée Cedex 2, France*
[305]*Faculty of Information Science and Technology, Osaka Institute of Technology, 1-79-1 Kitayama, Hirakata City, Osaka 573-0196, Japan*
[306]*NASA Goddard Space Flight Center, Greenbelt, MD 20771, USA*
[307]*Faculty of Science and Technology, Kochi University, 2-5-1 Akebono-cho, Kochi-shi, Kochi 780-8520, Japan*
[308]*Laboratoire de Physique de l'École Normale Supérieure, ENS, (CNRS, Université PSL, Sorbonne Université, Université Paris Cité), F-75005 Paris, France*
[309]*Faculty of Physics, University of Warsaw, Ludwika Pasteura 5, 02-093 Warszawa, Poland*
[310]*Laser Interferometry and Gravitational Wave Astronomy, Max Planck Institute for Gravitational Physics, Callinstrasse 38, 30167 Hannover, Germany*
[311]*The Hakubi Center for Advanced Research, Kyoto University, Yoshida-honmachi, Sakyou-ku, Kyoto City, Kyoto 606-8501, Japan*
[312]*Department of Physics, Kyoto University, Kita-Shirakawa Oiwake-cho, Sakyou-ku, Kyoto City, Kyoto 606-8502, Japan*
[313]*Yukawa Institute for Theoretical Physics (YITP), Kyoto University, Kita-Shirakawa Oiwake-cho, Sakyou-ku, Kyoto City, Kyoto 606-8502, Japan*
[314]*University of Catania, Department of Physics and Astronomy, Via S. Sofia, 64, 95123 Catania CT, Italy*
[315]*National Institute of Technology, Fukui College, Geshi-cho, Sabae-shi, Fukui 916-8507, Japan*
[316]*Department of Communications Engineering, National Defense Academy of Japan, 1-10-20 Hashirimizu, Yokosuka City, Kanagawa 239-8686, Japan*
[317]*Eindhoven University of Technology, 5600 MB Eindhoven, Netherlands*
[318]*Kavli Institute for the Physics and Mathematics of the Universe (Kavli IPMU), WPI, The University of Tokyo, 5-1-5 Kashiwa-no-Ha, Kashiwa City, Chiba 277-8583, Japan*
[319]*Department of Astronomy, Beijing Normal University, Xinjiekouwai Street 19, Haidian District, Beijing 100875, China*
[320]*School of Physics and Technology, Wuhan University, Bayi Road 299, Wuchang District, Wuhan, Hubei, 430072, China*
(Dated: December 5, 2025)

* Deceased, September 2024.